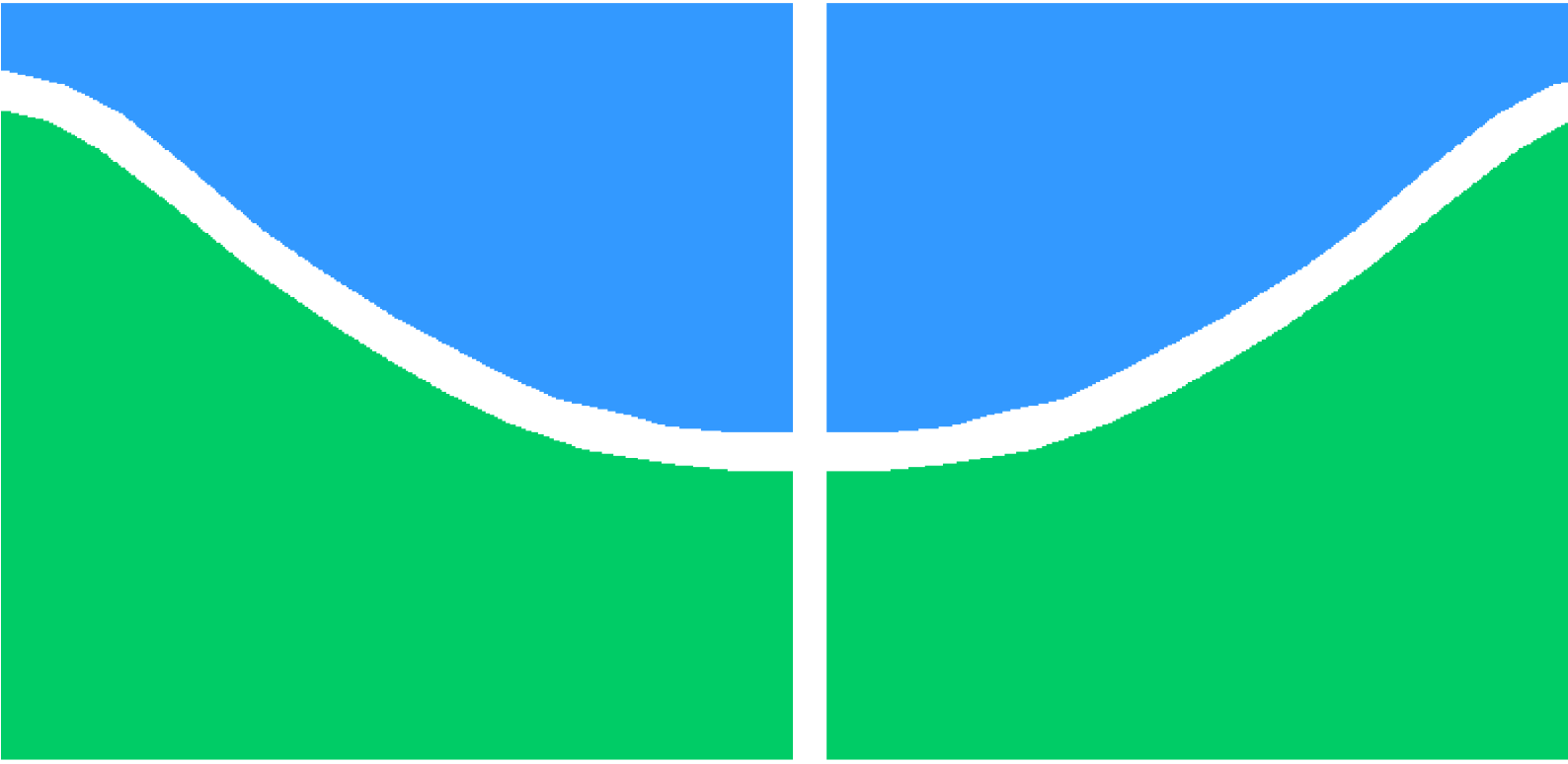

MASTER'S DISSERTATION

MICROSTRUCTURE AND VELOCITY FLUCTUATIONS IN A SEDIMENTING MAGNETIC SUSPENSION

Filipe Henrique de Sousa Evangelista

Brasília, November 11, 2019

UNIVERSIDADE DE BRASÍLIA

FACULDADE DE TECNOLOGIA

DEPARTAMENTO DE ENGENHARIA MECÂNICA

UNIVERSIDADE DE BRASÍLIA
Faculdade de Tecnologia
Departamento de Engenharia Mecânica

MASTER'S DISSERTATION

MICROSTRUCTURE AND VELOCITY FLUCTUATIONS IN A SEDIMENTING MAGNETIC SUSPENSION

Filipe Henrique de Sousa Evangelista

Dissertation submitted to the Department of Mechanical Engineering in partial fulfillment of the requirements for the degree of Master of Mechanical Sciences

Examining Committee

Francisco Ricardo da Cunha, PhD
Advisor (ENM-UnB)

Adriano Possebon Rosa, PhD
Internal Member (ENM-UnB)

Marcello Augusto Faraco Medeiros, PhD
External Member (USP)

Brasília, November 11, 2019

Este trabalho é dedicado à minha mãe,
por todo o apoio que me deu ao longo desta jornada.

"No single raindrop feels responsible for the flood."
(Douglas Adams)

"Our theories bear the same relationship to nature as symbols do to the entities they stand for, or as letters of the alphabet bear to the voice, or as notes do to music."
(Ludwig Boltzmann)

Acknowledgements

Meu percurso acadêmico somente se iniciou e persistiu pela influência dos muitos amigos e entes queridos que me motivaram e ampararam, aos quais agradeço:

À minha mãe, Talita, por tudo! Por me apoiar e confiar em mim, mesmo desejando que eu tivesse trilhado caminhos mais fáceis, por me dar suporte financeiro e emocional ao longo de tudo, por cuidar de mim e orar por mim, sempre me desejando o melhor. Não sou capaz de retribuir tudo mas o que sempre quis é, em algum momento, poder dividir contigo o que eu chegar a usufruir e te ajudar a alcançar os teus anseios.

Ao meu pai, Valdeci, por também me apoiar financeiramente, me permitindo tentar traçar uma carreira que de outro modo não seria possível.

Ao meu tio Assis, por ter sido como um pai para mim desde cedo, por fomentar meu interesse pela matemática e a resolução de problemas desde cedo, bem como acompanhar com interesse minhas escolhas desde então. Com o mesmo interesse me acompanha também toda a família, que me deseja sucesso e paz, e por isto sou grato. Faço menção particular também à tia Zeres, ao tio Joab, à tia Elita e o tio Fábio, que acompanharam regularmente durante este processo e sempre se colocaram à disposição para contribuir de todas as formas possíveis.

Ao meu amigo Edson Júnior, que me apoiou na escolha pela Mecânica, que me deu aulas preparatórias para o vestibular e caronas para a UnB. Com as aulas, moldei minha forma de pensar, aprendi a procurar entender princípios ao invés de memorizar fórmulas e aprofundei meu interesse pela missão de transmitir o conhecimento. De ambos estes favores que me foram prestados, ficou a lição de generosidade que procuro passar à frente.

À minha psicóloga, Sheila, por me ajudar a encontrar um caminho na vida ao longo da graduação, permitir que eu me conhecesse melhor e isto dar suporte ao meu progresso acadêmico. Além disso, agradeço pelo bom entendimento que tivemos e pela empatia que você demonstrou comigo, sempre desempenhando um papel ativo em tentar me direcionar à rota da evolução pessoal, rumo à conquista dos meus sonhos, passo a passo.

Aos amigos do TJDFT pelos valiosos conselhos, indicações de livros, momentos de descontração e de crescimento pessoal, em especial ao Seu Sérgio, Thiagão, Rui, Bruce e

ao Galo Doido.

Devo também importante menção àqueles que me inspiraram e auxiliaram durante a graduação. Agradeço imensamente ao Professor Francisco Ricardo, cujas aulas despertaram meu interesse para a Mecânica dos Fluidos, sendo também meu primeiro contato sério com a Matemática Aplicada e um passo primordial na construção de uma formação mais séria e necessária à prática científica. Ademais, agradeço-o pelo inesgotável esforço em prover condições adequadas de trabalho no Vortex, seja na infraestrutura, seja na orientação cordial e consciente, que levo como exemplo para minha futura prática profissional.

Aos meus colegas do Vortex, pelo ambiente empático que tive e por tudo que aprendi com vocês:

- Ao Igor, pelos exemplos de profissionalismo, competência, inteligência e empatia. Confio que você alcançará seus objetivos e será na vida profissional aquilo que já é para o Vortex: um exímio trabalhador e uma companhia maravilhosa. Você é um grande amigo que me deu muita força nos momentos em que senti mais dúvidas e dificuldades. *Bonne chance !*;

- Ao Gesse, por se importar com cada um de nós, se colocar à nossa disposição para ajudar sempre que necessário e descontrair o ambiente. Você é um cara brilhante, certamente fará um doutorado espetacular aí no Colorado e já faz falta aqui no Vortex. Agradeço também por todas as suas contribuições ao meu trabalho, bem como ao meu conhecimento de Matemática, Física, pizzarias e hamburguerias;

- Ao Yuri, cuja tranquilidade e paz me permitiram ver um modo alternativo de viver no ambiente acadêmico, no qual há tanta pressão. Seu modo de ser trouxe equilíbrio ao nosso grupo e sua amizade nos é muito prezada. Mesmo sendo uma pessoa tão ímpar, você é simpático, humilde e altruísta, e isso te faz uma ótima companhia. Sua inteligência, dedicação e conquistas nos motivam a crer que também podemos alcançar nossos objetivos;

- Ao Shumy, cuja postura de constante interesse pelo aprendizado e a pesquisa o tornam um ótimo pesquisador e uma motivação para mim. Tenho aprendido bastante nas discussões acadêmicas contigo. Ademais, você é um grande amigo, que contribui para o clima de trabalho, apoiado pelo suporte coletivo que encontrei no Vortex;

- Ao Dr. Álvaro, por ser para mim um exemplo de companheirismo, humildade, foco, perseverança e uma fé benéfica, que o sustentou durante tudo. Aprendi contigo valiosas lições, que serão deveras importantes para os próximos estágios da vida, e desejo ser no doutorado alguém como você, que alegre os mais próximos e seja exitoso em seus desígnios. Agradeço por tudo e vamos agir com a vida!

À Amanda, minha namorada, que chegou à minha vida ao fim da graduação, e com quem me identifiquei rapidamente no âmbito acadêmico pela avidez por aprender e explorar o desconhecido e o fascínio com a beleza do Universo. Neste percurso, tivemos muitas discussões iluminadoras e pude aprender demais! Agradeço por ter me amparado emocionalmente ao longo do turbilhão de sentimentos que é o mestrado. Afora isto, soulhe grato pelas preciosas indicações culturais que complementaram minha vida enquanto concluía este trabalho.

Por fim, agradeço também aos membros da banca, Prof. Adriano Possebon Rosa e Prof. Marcello Augusto Faraco, pela cuidadosa leitura deste trabalho e pelas sugestões valiosas ao aprimoramento do mesmo.

Resumo

Neste trabalho, efetua-se um estudo numérico das propriedades de suspensões magnéticas gás-sólido em escoamentos puramente viscosos.

Primeiramente, investiga-se a sedimentação de uma partícula esférica isolada em fluido newtoniano, quando esta é suficientemente pequena para que forças brownianas sejam consideradas mas o número de Reynolds seja desprezável. Deste modo, conseguimos definir os parâmetros físicos apropriados para o escoamento de suspensões. As simulações para este caso simples ainda possibilitam a validação do método numérico para o cálculo da variância das flutuações de velocidade e a função autocorrelação destas flutuações em uma ampla faixa de números de Péclet e Stokes.

Em seguida, efetuam-se simulações de Dinâmica de Langevin para integrar as equações governantes dos movimentos translacional e rotacional de N partículas micrométricas suspensas em um fluido puramente viscoso, incluindo interações hidrodinâmicas, para suspensões magnéticas e não-magnéticas.

O primeiro objetivo desta dissertação é investigar o comportamento de curto tempo das flutuações de velocidade das partículas em suspensão, em termos da variância das tais. Também é apresentado um estudo do comportamento de longo tempo dessas flutuações de velocidade, calculando sua autocorrelação no tempo e a difusividade das partículas, que foi observada anisotrópica.

Sabendo a variância das flutuações de velocidade a partir das simulações numéricas, determinou-se a pressão de partículas em termos da fração volumétrica de partículas, sendo esta relação tipicamente uma quantidade de fechamento em modelos de sistemas particulados complexos, como leitos fluidizados. Este cálculo baseado em princípios físicos é uma contribuição inédita deste trabalho, visto que modelos de pressão de partículas são geralmente heurísticos.

Detalhes do tensor de flutuações de velocidade hidrodinâmicas e sua importância para a pressão de partículas e a viscosidade de partículas são discutidos. As simulações mostram clara evidência da pressão de partículas resultando do distúrbios ao escoamento produzidos pelas interações hidrodinâmicas na suspensão diluída.

Finalmente, examinaram-se os efeitos das interações magnéticas dipolares e do campo magnético externo sobre as propriedades supracitadas. Notou-se que as interações

magnéticas dipolares produzem uma recorrelação das flutuações de velocidade, causando um coeficiente de difusão divergente. Até onde se sabe, este também é um resultado inédito.

Palavras-chave: suspensões magnéticas, flutuações de velocidade, pressão de partículas, difusividade, interações hidrodinâmicas, interações magnéticas dipolares, sedimentação.

Abstract

In this work, we undertake a numerical study of properties of magnetic gas-solid suspensions of micron-sized particles sedimenting in creeping flow.

First we investigate the sedimentation of an isolated spherical particle in a Newtonian fluid when it is small enough for Brownian forces to be considered but the Reynolds number is negligible, in order to define the appropriate physical parameters of our suspension flows. The simulations for this simple case allow us to validate the numerical approach for calculating velocity fluctuations variance and autocorrelation function over a wide range of Péclet and Stokes numbers.

Next, we perform Langevin Dynamics simulations to integrate the equations governing the translational and rotational motions of N micron-sized spherical particles suspended in a viscous fluid, including hydrodynamic interactions between the particles, both for non-magnetic and magnetic suspensions.

The first particular interest of this dissertation is to investigate the short-time behavior of the particle velocity fluctuations in this suspension in terms of its variance. We also present a study of the long-time behavior of these velocity fluctuations by calculating their time autocorrelation functions and the anisotropic particle diffusivities.

Knowing the particle velocity variance from the numerical simulations, we determine the particle-phase pressure in terms of the particle volume fraction, that usually being a closure quantity required in models of complex particulate systems such as fluidized beds. This calculation based upon physical principles is a novel contribution of this work, since models of particle-phase pressure are typically heuristic.

Details of the hydrodynamic velocity fluctuations tensor and its importance to determine the particle-phase pressure and particle viscosity are discussed. The simulations show clear evidence for the particle pressure arising from the flow disturbance produced by hydrodynamic interactions in a dilute suspension.

Finally, we examine the effect of magnetic dipolar interactions and the intensity of the external field over these properties. We find out that magnetic dipolar interactions produce a recorrelation of velocity fluctuations, yielding a divergent diffusivity coefficient. To the best of our knowledge, this is also a novel result.

Keywords: magnetic suspensions, velocity fluctuations, particle-phase pressure, diffusivity, hydrodynamic interactions, magnetic dipolar interactions, sedimentation.

List of Figures

List of Tables

List of abbreviations and acronyms

cf.	See
Chap.	Chapter
e.g.	For example
Eq.	Equation
Fig.	Figure
i.e.	That is
ODE	Ordinary differential equation
PDE	Partial differential equation
PDF	Probability density function
Sec.	Section
SI	International System of Units
Tab.	Table

List of symbols

Latin symbols

a_i	Hydrodynamic radius of the i-th particle
$a_{m,i}$	Magnetic core radius of the i-th particle
$\bar{a}$	Reduced hydrodynamics radius
A	Open surface
b	Contact radius between particles
$\boldsymbol{b}$	Body force
$\boldsymbol{B}$	Magnetic induction
B_0	Reference configuration
B_t	Current configuration
$\mathcal{B}$	Continuous body
$\boldsymbol{c}$	Normalized autocorrelation of velocity fluctuations
$\boldsymbol{C}$	Autocorrelation of velocity fluctuations
$\boldsymbol{d}$	Rate of strain tensor
D_0	Einstein-Stokes diffusivity
$\boldsymbol{D}$	Diffusivity tensor
$\boldsymbol{D}_e$	Electric displacement field
$\boldsymbol{E}$	Electric field
$\boldsymbol{F}_\alpha$	Total force over a particle
$\boldsymbol{F}_i^h$	Hydrodynamic force over a particle
$\boldsymbol{F}_i^{nh}$	Non-hydrodynamic force over a particle

$\boldsymbol{\mathcal{F}}$	Deformation gradient in the Lagragian description
$\boldsymbol{g}$	Gravitational acceleration
$\bar{G}$	Time average of an arbitrary stochastic process G
G'	Fluctuation of an arbitrary stochastic process G
$\boldsymbol{G}$	Oseen tensor
$\boldsymbol{H}$	Magnetic field
$\boldsymbol{I}$	Identity tensor
J_i	Moment of inertia of the i-th particle
$\boldsymbol{k}$	Wavenumber vector
$\boldsymbol{L}$	Linear momentum
$\boldsymbol{M}$	Magnetization
$\mathcal{M}_i$	Mass of a particle
$\boldsymbol{m}$	Dipole moment
$\hat{\boldsymbol{n}}$	Unit normal vector to a surface
n_r	Number of realizations
n	Density number
N	Number of particles
$\boldsymbol{P}$	Electric polarization
P_n	Legendre polynomials
p	Pressure field
p_p	Particle pressure
Pe	Péclet number
ρ	Density of the fluid
ρ_s	Density of the particles
$\boldsymbol{\mathcal{P}}$	Pressure field Green kernel
$\boldsymbol{r}$	Distance vector between two particles
Re	Reynolds number

Re_t	Terminal Reynolds number
S	Closed surface
$S(\boldsymbol{k})$	Structure factor
$\boldsymbol{S}$	Stresslet
St	Stokes number
Δt	Time-step
t	Time
$\boldsymbol{t}$	Traction
T	Temperature
$\boldsymbol{T}$	Stresslet of a point particle
$\boldsymbol{u}$	Eulerian velocity field
$\boldsymbol{u}'$	Velocity fluctuations
$\boldsymbol{u}^\infty$	Velocity of the undisturbed flow
$\boldsymbol{u}^D$	Velocity disturbance
$\boldsymbol{U}_s$	Stokes velocity
V	Volume
$\boldsymbol{W}$	Vorticity tensor
$\boldsymbol{x}$	Position vector
$\boldsymbol{X}$	Label of a material point
Y_{lm}	Spherical harmonics

Greek symbols

i, j	Particle numbering indices
$\delta(\boldsymbol{x})$	Dirac delta distribution
δ_{ij}	Virtual overlap between particles i and j
ε_0	Electric vacuum permittivity
ε_{ij}	Gap between particles
$\boldsymbol{\varepsilon}$	Levi-Civita third rank tensor
ϕ	Volume fraction of particles
φ	Magnetic potential
Φ	Configuration map
μ_0	Magnetic vacuum permeability
η	Dynamic viscosity
Ω	Solid angle
$\boldsymbol{\Omega}$	Angular velocity of particles
$\boldsymbol{\sigma}$	Stress tensor
τ_b	Brownian diffusion time
τ_c	Velocity fluctuations correlation time
τ_s	Sedimentation time
τ_r	Inertial relaxation time
$\boldsymbol{\xi}$	Vorticity

Mathematical symbols

$\mathbb{R}$	Field of the real numbers
∇	Nabla differential operator
$\langle\rangle$	Ensemble average
*	Complex conjugation

Summary

1 Introduction

1.1 Overview of Magnetic Suspensions

In this work we investigate some properties of non-colloidal magnetic suspensions in sedimentation via numerical integration of their equation of motion. We take a particular interest in gas-solid suspensions, though the formulation is more general in nature and may be applied to liquid-solid suspensions. In this context, we firstly make a brief exposition of magnetic suspensions in general, their distinctive physical characteristics and technological uses.

A noteworthy consequence of the insertion of particles in a fluid, even when they are not magnetic, is the alteration of properties of the resulting suspension. For example, the effective viscosity of an infinitely dilute[1] statistically homogeneous suspension was shown by Einstein (1956) to be enhanced by the carried particles, whose presence imposes an additional energy dissipation. Furthermore, when the particles are close enough to alter the flow around their neighbors, the effect of the particle configuration comes into play resulting in further change of properties, e.g. in the work of Batchelor and Green (1972). This conclusion opens up a possibility to tune the properties of a suspension to a given application. Magnetic suspensions fulfill that exact purpose. They are comprised of particles which react to an external field, thereby rendering it suitable for the control of their configuration and consequently also the rheological[2] properties of the suspension.

Magnetic suspensions can be classified according to their properties and applications. Ferrofluids were the first of these suspensions to be studied, under the theoretical setting of the work of Rosensweig (1969). They are made of ferromagnetic *nanometric* particles, typically suspended in oil based, organic or inorganic fluids, such as ester, water and kerosene, respectively. A physically remarkable feature of these fluids is a tendency to align along imposed magnetic field lines, as seen in Fig. (1). In a shear flow setting, this mechanism culminates in a competition between rotation imposed by the flow and orientation with the magnetic fields lines, promoting additional energy dissipation in what is called the magnetoviscous effect (ROSENSWEIG; KAISER; MISKOLCZY, 1969).

[1] That is, where pairwise interactions between particles are negligible.

[2] Rheology is the study of deformation and flow of matter (MORRISON et al., 2001), typically in the realm of complex fluids, aiming to the characterization of its properties.

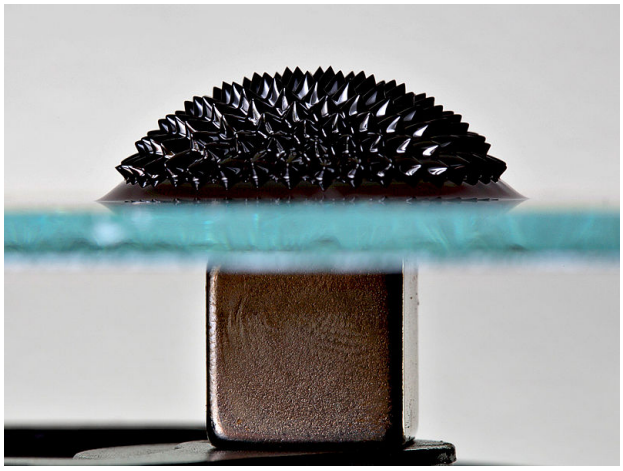

Figure 1 – Ferrofluid over glass under the action of a magnet (Gregory F. Maxwell, 2006).

Their firstly designed applications center around their capacity of presenting elevated yield stresses when submitted to external magnetic fields, thus being fit to sealing applications, as rotary shaft seals (RAJ; MOSKOWITZ, 1990). More recent applications include damping of loudspeakers, illustrated by Fig. (2), currently used by prominent companies like Sony. It consists in hindering resonance peaks of the diaphragm motion, smoothing transient responses in frequency changes and enhancing heat transfer in the coil cooling (RAJ; MOSKOWITZ, 1990). Medical applications also exist, such as magnetic hyperthermia, a treatment for cancerous tumor oblation based on the heat generated by a ferrofluid subject to an oscillatory magnetic field (HIERGEIST et al., 1999).

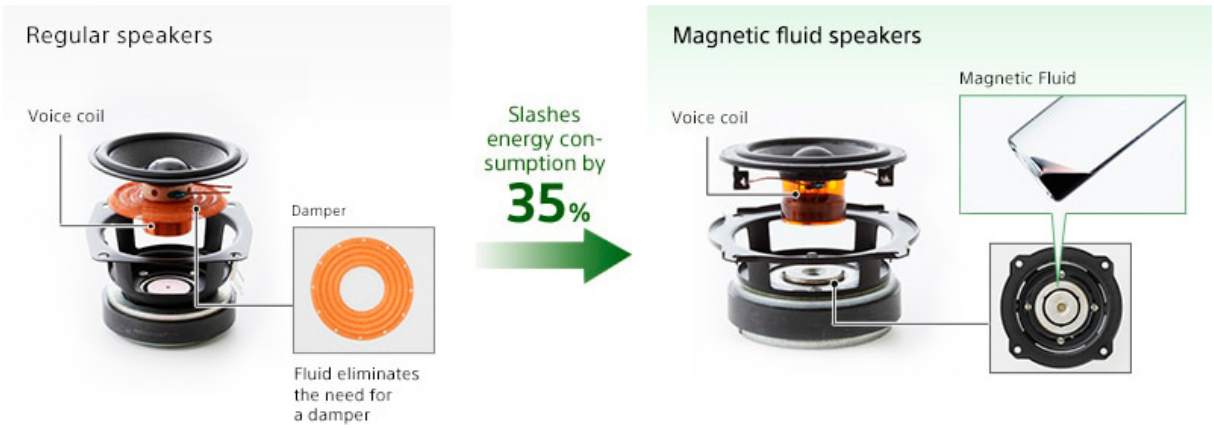

Figure 2 – Loudspeaker damping with ferrofluids (Sony, 2014).

Magnetorheological fluids are liquid-solid suspensions of *micrometric* magnetizable particles and they are so called due to the sharp change in their rheological properties with the application of an external magnetic field. Indeed, they transition from liquid-like to solid-like states with the application of the field due to the formation of chain-like structures and more complex coherent structures, so that they will only flow under stresses above a minimum threshold, called yield stress (BICA; LIU; CHOI, 2013). Some technologies based upon this physical feature are damping devices to control mechanical vibrations, such as car brakes and seismic shock dampers in buildings (BICA; LIU; CHOI,

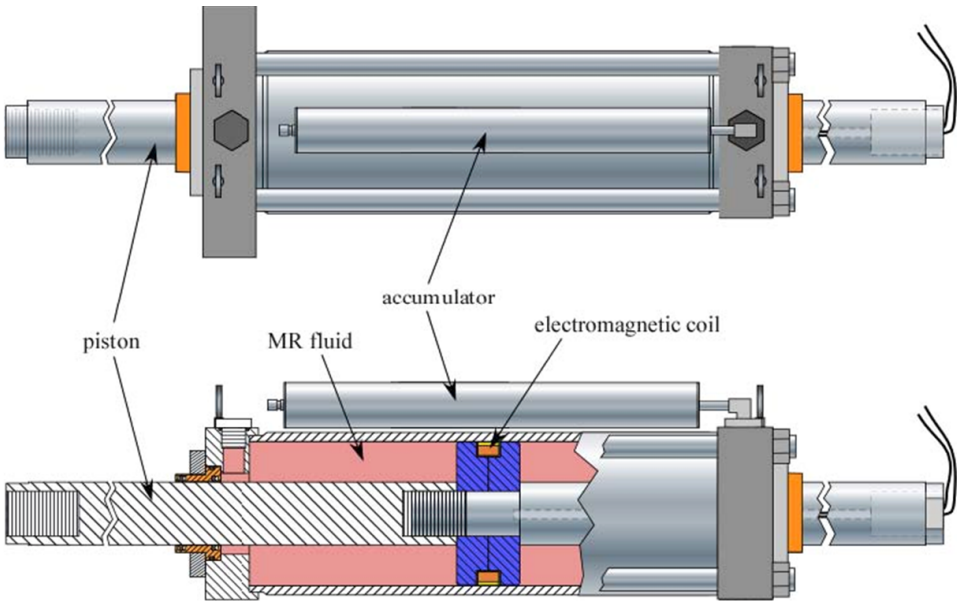

Figure 3 – Magnetorheological fluid seismic damper (Purdue University, 2010).

2013), depicted in Fig. (3).

Gas-solid magnetic suspensions are also often encountered in practice, chiefly in the stabilization of fluidized beds by an external magnetic field, as first proposed by Rosensweig (1979). Fludized beds are suspensions of millimeter-sized particles carried upwards by an injected fluid, whose purpose is to perform chemical reactions at elevated rates, in view of the high velocities which these particles attain. Their performance is lowered by the formation of large voids of particles in the carrier fluid, thence the motivation for flow control strategies which inhibit this behavior. This particular stabilization scheme works by the formation of complex structures of linked particles due to magnetic dipolar interaction and a tendency to align with the external field, hence restraining the flow and controlling void fractions formation. Fig. (4) shows voidage waves in a non-magnetic fluidized bed.

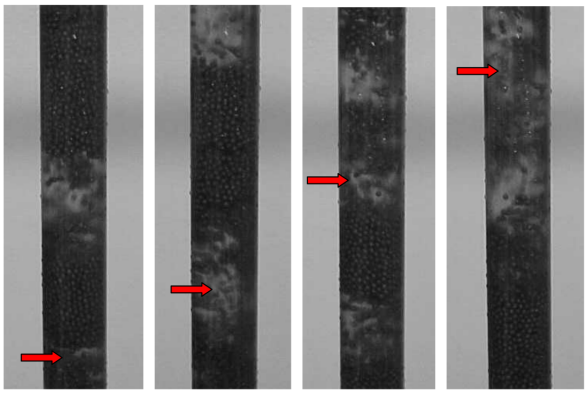

Figure 4 – A fluidized bed. Traveling voidage waves indicated by the arrows. Courtesy of the Vortex Lab-UnB.

Yet, a seldom investigated scenario, both from the theoretical and applied viewpoints is that of micron-sized ferromagnetic particles immersed in a gas, a dual regime in

which the inertia of the particles should often be taken into account although the inertia of the carrier fluid is negligible. Foreseeable applications of this physical system abound, even more so with the freshly arisen interest in microfluidics devices. Moreover, since the non-inertial regime of the fluid is linear, analytical methods of solution of its equation of motion are available, enabling simpler methods to determine the motion of the particles, which apply the available theoretical machinery of microhydrodynamics to avoid numerically solving the fluid phase equations.

1.2 Literature Review

In view of our interest in the hydrodynamical aspects of motion, both for an isolated particle and then for a collection of interacting particles, we firstly remark some of its aspects, then list some contributions from papers in magnetic and non-magnetic suspensions in order to specify and justify the subarea of magnetic suspensions examined in this dissertation.

The sedimentation of isolated particles in fluids has long arisen the interest of the scientific community for its rich dynamics, ensuing a great number of renowned works from early on, e.g. the quadratic drag formula of Newton (1687) and the solution of Stokes (1851) for a falling sphere in creeping flow. The interaction between particle and the fluid, which is governed by the non-linear Navier-Stokes equation, may give rise to intriguingly erratic motion, cf. (ERN et al., 2012). In fact, this problem is not completely solved and there have been many works lately concerning the solution of the equation of motion for the sedimentation of an isolated particle in a fluid for finite Reynolds numbers, subject to different circumstances, such as a Basset force (SOBRAL; OLIVEIRA; CUNHA, 2007), hydrodynamic drags given by particular drag formulas (FERREIRA; CHHABRA, 1998), anistropy of the particle shape (MOHAZZABI, 2010) or non-Newtonian fluids (CHHABRA; SOARES; FERREIRA, 1998; JAYARAMAN; BELMONTE, 2003).

In the linear regime of low Reynolds numbers, collisions of the mesoparticle with the fluid particles result in Brownian fluctuations and induce a diffusive process (EINSTEIN, 1956). Primordial works as that of Uhlenbeck and Ornstein (1930) helped establish a solid knowledge of this process. This proper understanding of the motion of individual particles is the first step to describing suspensions. However, the complexity of the dynamics of a suspension is far greater than that of an isolated particle since in the latter, the presence of a particle disturbs the flow, which in turn modifies the path of the others. Thus, this hydrodynamic interaction between particles stems displacements from their original streamlines upon eventual encounters, yielding a collective diffusive behavior at times much larger than the one it takes for a particle to fall through its own radius (RALLISON; HINCH, 1986). Therefore, a complex interplay between hydrodynamic and Brownian fluctuations befalls.

The analysis of such systems by analytic methods has been fruitful in very dilute regimes, where only pairwise interactions are accounted, e.g. Batchelor's calculations of the average velocity and viscosity of these suspensions (BATCHELOR, 1972; BATCHELOR, 1976). In that context, two-body problems describe properly the effects of interactions and have been used to calculate transport properties (CUNHA; HINCH, 1996). In contrast, numerical methods are applicable to wider volumetric fraction regimes and are amenable to the insertion of physical mechanisms without major alterations. Many contributions have been made in this manner, e.g. in colloidal suspensions (BRADY; BOSSIS, 1988; LADD, 1993; CUNHA et al., 2002; CUNHA; SOUSA; HINCH, 2002; PADDING; LOUIS, 2004), ferrofluids (GONTIJO; CUNHA, 2015), magnetorheological suspensions (MOHEBI; JAMASBI; LIU, 1996; MELLE et al., 2002; BOSSIS et al., 2011; ROURE; CUNHA, 2018) and magnetic fluidized beds (WANG et al., 2013).

Nevertheless, some works numerical focus on the regime of negligible particle inertia, thus there is still room for the study of its effect over macroscopic properties. An investigation of this influence could be paramount in attempts to reconcile the variance of velocity fluctuations of non-magnetic suspensions determined by numerical simulations (KOCH, 1994; CUNHA et al., 2002) and analytic calculations (CAFLISCH; LUKE, 1985) with that observed in experiments (NICOLAI; GUAZZELLI, 1995), under the claim that the inertia of the particles could balance the statistical weight fluctuations in the suspension (CUNHA, 1997), which induces convective currents. Effects of hydrodynamic interactions, considered in this work, are even more often disregarded. This is an important contribution of this study.

These velocity fluctuations also give rise to a hydrodynamic fluctuations stress tensor, analogously to turbulence, whose isotropic part is associated to a particle-phase pressure. Several works in the literature have used a suitable choice of the particle pressure as a function of the particle volume fraction to investigate stability of fluidized beds (HARRIS; CRIGHTON, 1994; DURU et al., 2002; SUNDARESAN, 2003; CUNHA; SOBRAL; GONTIJO, 2013; SOBRAL; HINCH, 2017). In fact, the resulting models are not based in a method of calculating particle pressure from first principles. Batchelor (1988) appears to be the first who proposed some physical basis, suggesting that particle pressure may be associated to particle velocity fluctuations or particle self-diffusivity in low Reynolds numbers. A study of fluctuations and particle pressure in a homogeneous sedimenting gas-solid suspension based on kinetic theory and numerical simulations for concentrated suspensions of moderated Stokes number showed particle velocity fluctuations to be significantly anisotropic (KOCH; SANGANI, 1999). A crucial step in determining the particle pressure is to predict the magnitude of the particle velocity fluctuations. In the absence of an imposed shear flow, the velocity fluctuations of non-Brownian, non-magnetic particles arise solely due to the hydrodynamic interactions among the particles.

Furthermore, the magnetic gas-solid suspension dual regime where the inertia of the fluid is negligible, as opposed to that of the particles, is still feasible for micrometric

particles, and a sensible calculation assuming typical values for its parameters shows that even Brownian motion may still be sensibly retained. Indeed, as shown in Tab. (1), the Stokes number, St, and Péclet number, Pe, which respectively quantify particle inertia and Brownian fluctuations, both present moderate non-negligible values.

Table 1 – Typical parameters of magnetic gas-solid suspensions of micron-sized particles. ρ_s is the particle density, ρ the fluid density, η the fluid viscosity, a the particle radius, g the gravitational acceleration, k_B Boltzmann's constant, T the temperature, St Stokes' number, Re Reynolds' number and Pe Péclet's number.

ρ_s (kg/m^3)	10^4
ρ (kg/m^3)	1.2
η (Pa.s)	1.8×10^{-5}
a (μm)	1
g (m/s^2)	9.81
k_B (J/K)	1.38×10^{-23}
T (K)	298
St	0.05
Re	8×10^{-5}
Pe	100

1.3 Scope of the Work

The main goal of this work is the description of the short and long-time behavior of the hydrodynamic velocity fluctuations tensor in a dilute magnetic gas-solid suspension under conditions of high Péclet number and small Stokes numbers. The relevant macroscopic properties such as the variance of velocity fluctuations, the velocity autocorrelation functions, their associated diffusivities and the particle-phase pressure are determined by our Langevin Dynamics computer simulations. While this is generally well-known, it should be appreciated that a study involving the prediction of particle pressure based on the direct calculation of particle velocity fluctuations in a suspension is still an open question. This is a particularly valuable approach to the study of non-Brownian suspensions, where the computation of the above mentioned properties by direct numerical simulations of particle velocity fluctuations seems to be still scarce.

In order to attain these objectives, the dissertation structure is organized follows:

- **Chapter 2**: We describe the theoretical foundation of the models for the physical mechanisms inserted in the simulation;
- **Chapter 3**: We carry out numerical simulations of an isolated non-magnetic particle in sedimentation and compare their results to the analytic solution;
- **Chapter 4**: We describe the methodology of many-body simulations by extending the procedure employed in the single particle case;

- **Chapter 5**: We simulate the motion of suspensions of massive magnetic and non-magnetic particles in sedimentation. In the latter case, we investigate the effect of hydrodynamic interactions and particle inertia over the velocity fluctuations, whereas in the former we examine the effects of dipolar interactions and the external field;
- **Chapter 6**: We present results and simulate particular settings which are related to potential applications. There, our interest is qualitative;

2 Theoretical Fundamentals

This chapter presents an overview of the theoretical background of this work, in what concerns the main forces and torques of Brownian, hydrodynamic and magnetic origin. These are the principal mechanisms which influence the collective motion of the low Reynolds number magnetic suspension here investigated.

We start by deriving general equations of fluid motion under the framework of continuum mechanics. Then, we restrict our analysis to flows free of fluid inertia and obtain expressions for the forces which they exert upon immersed particles. Lastly, we present Maxwell's equations, specify them to the magnetostatic regime and employ them to determine the generalized forces due to external magnetic fields or magnetic dipolar interaction.

2.1 Balance Equations of a Fluid

2.1.1 Continuum Hypothesis and Motion

Continuum mechanics is concerned with the derivation of equations of motion for continuous media, whose properties are described by fields. This description is based upon the continuum hypothesis, i.e., the assumption that matter may be regarded as continuous, rather than discrete. Physically, this is tantamount to ascribing local properties to the continuum, which are in fact averages of molecular properties over a volume sufficiently large to contain enough particles to render this statistic significant, yet smaller than spatial macroscopic variations due to the flow (BATCHELOR, 2000). The volume at which these averages converge is called sensitive volume.

For instance, the density of a fluid is defined as the limit

$$\rho(\boldsymbol{x}) = \lim_{\delta V_{\boldsymbol{x}} \to \delta V_{\boldsymbol{x}}^*} \frac{1}{\delta V_{\boldsymbol{x}}} \int_{\delta V_{\boldsymbol{x}}} \sum_i \mathcal{M}_i \delta(\boldsymbol{x}_i - \boldsymbol{y})\, d\boldsymbol{y} \tag{2.1}$$

as the sampling volume $\delta V_{\boldsymbol{x}}$ tends to the sensitive volume $\delta V_{\boldsymbol{x}}^*$. Here, $\delta(\boldsymbol{x}_i - \boldsymbol{y})$ is the Dirac delta distribution and $\boldsymbol{y}$ is a dummy position vector which sweeps the sampling volume, as illustrated by Fig. (5). In this idealization, the volume is composed of concentrated point-masses $\mathcal{M}_i$ each located at the position $\boldsymbol{x}_i$. The presence of the Dirac delta as

weighting factor ensures that volume integrals over regions containing mass points yield their total mass. Fig. (6) shows how the values of the aforementioned averages typically vary with the volume over which they are measured.

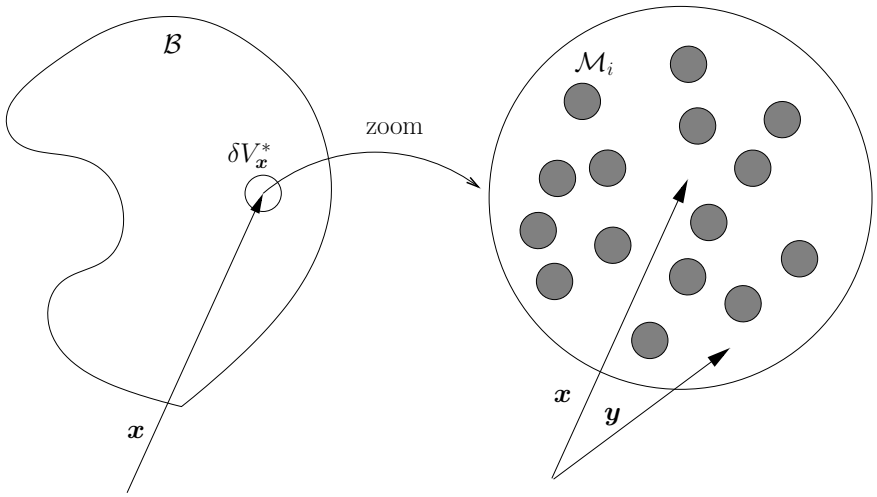

Figure 5 – Continuum density as the volume average over a sensitive volume $\delta V_{\boldsymbol{x}}^*$.

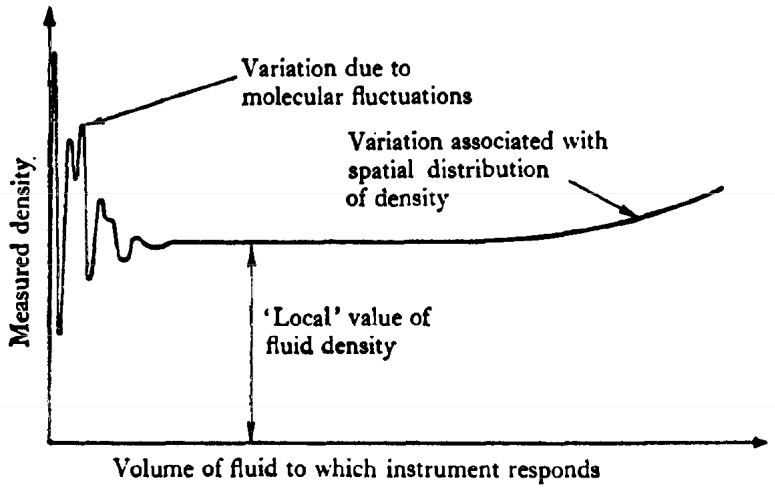

Figure 6 – Dependence of the density on the sensitive volume of the instrument of measure (BATCHELOR, 2000).

Mathematically, a continuous body $\mathcal{B}$ is identified by the set of labels of its particles, $\mathcal{B} = \{\boldsymbol{X}\}$. The continuum hypothesis implies that these particles are nondenumerable, thus instead of counting them, we map them to a region (a configuration) which they occupy at some reference time, V_0 (ODEN, 2011). Hence, a motion is described by a mapping Φ that takes an initial configuration V_0 to a current configuration V at a time t, i.e.,

$$\boldsymbol{x} = \Phi(\boldsymbol{X}, t). \tag{2.2}$$

It should be noted that the continuum hypothesis is not always applicable, since there are physical settings where volumes which contain sufficient molecules for the convergence of averages of properties are already large enough to capture their macroscopic

variations. Thus, local properties cannot be defined. This could occur, for example, in shock waves and in rarefied gases (BATCHELOR, 2000).

The distinction between coordinates of points in space and labels of particles permits two different descriptions of motion: one named Eulerian, which gives properties as functions of positions in space, e.g. $\rho(\boldsymbol{x}, t)$, and another named Lagrangian, describing properties as functions of particle labels, $\rho(\Phi(\boldsymbol{X}, t), t)$. Laws of motion in classical mechanics describe rates of variation of state variables of given particles, i.e., they are naturally written in terms of derivatives with fixed labels. Therefore, derivatives with a fixed $\boldsymbol{X}$ appear in Eulerian descriptions of motion, and in order to write them only in terms of fields, we employ the chain rule,

$$\frac{DG}{Dt} := \left(\frac{\partial G}{\partial t}\right)_{\boldsymbol{X}} = \left(\frac{\partial G}{\partial t}\right)_{\boldsymbol{x}} + \boldsymbol{u}(\boldsymbol{x}, t) \cdot \nabla G(\boldsymbol{x}, t), \tag{2.3}$$

where the material derivative operator has been defined. There, $\boldsymbol{u}(\boldsymbol{x}, t)$ is the velocity field of the continuum, i.e., the material derivative of the position vector and $G(\boldsymbol{x}, t)$ is an arbitrary tensor field of any rank.

In the following sections, we shall be concerned with the derivation of the equations of motion for a fluid, which involve time rates of change of integrals over material volumes. To this end, it is useful to carry out those integrals over the reference configuration using the mapping (2.2). Since this requires knowledge of the time derivative of the mapping Jacobian determinant, we finish this section with its deduction. Consider the Jacobian of transformation (2.2), also referred to as the gradient of deformation in the Lagrangian description,

$$\boldsymbol{\mathcal{F}} = \frac{\partial \boldsymbol{x}}{\partial \boldsymbol{X}}, \tag{2.4}$$

whose coordinates are $\mathcal{F}_{ij} = \partial x_j / \partial X_i$. Its material and partial derivatives commute, so by the chain rule,

$$\frac{D\boldsymbol{\mathcal{F}}}{Dt} = \boldsymbol{\mathcal{F}} \cdot \nabla \boldsymbol{u}. \tag{2.5}$$

Now the derivative of the determinant is, by the chain rule,

$$\frac{D \det \boldsymbol{\mathcal{F}}}{Dt} = \frac{d \det \boldsymbol{\mathcal{F}}}{d\boldsymbol{\mathcal{F}}} : \frac{D\boldsymbol{\mathcal{F}}}{Dt}. \tag{2.6}$$

Note that the right-hand side is the inner product of the gradient[1] of the determinant of $\boldsymbol{\mathcal{F}}$ and another tensor, so by definition

$$\frac{d \det \boldsymbol{\mathcal{F}}}{d\boldsymbol{\mathcal{F}}} : \frac{D\boldsymbol{\mathcal{F}}}{Dt} = \lim_{h \to 0} \frac{1}{h} \left[\det\left(\boldsymbol{\mathcal{F}} + h \frac{D\boldsymbol{\mathcal{F}}}{Dt}\right) - \det\left(\boldsymbol{\mathcal{F}}\right) \right]. \tag{2.7}$$

Binet's theorem yields

$$\det\left(\boldsymbol{\mathcal{F}} + h \frac{D\boldsymbol{\mathcal{F}}}{Dt}\right) = \det(\boldsymbol{\mathcal{F}}) \det\left(\boldsymbol{I} + h \boldsymbol{\mathcal{F}}^{-1} \cdot \frac{D\boldsymbol{\mathcal{F}}}{Dt}\right). \tag{2.8}$$

[1] With respect to the coordinates of $\boldsymbol{\mathcal{F}}$.

Furthermore, by a Taylor expansion,

$$\det\left(\boldsymbol{I}+h\boldsymbol{\mathcal{F}}^{-1}\cdot\frac{D\boldsymbol{\mathcal{F}}}{Dt}\right)=1+h\,\mathrm{tr}\left(\boldsymbol{\mathcal{F}}^{-1}\cdot\frac{D\boldsymbol{\mathcal{F}}}{Dt}\right)+\mathcal{O}(h^2). \tag{2.9}$$

Inserting Eq. (2.5) in Eq. (2.9),

$$\det\left(\boldsymbol{I}+h\boldsymbol{\mathcal{F}}^{-1}\cdot\frac{D\boldsymbol{\mathcal{F}}}{Dt}\right)=1+h\nabla\cdot\boldsymbol{u}+\mathcal{O}(h^2), \tag{2.10}$$

so Eqs. (2.6), (2.7), (2.8) and (2.10) yield

$$\frac{D\det\boldsymbol{\mathcal{F}}}{Dt}=\det\boldsymbol{\mathcal{F}}\,\nabla\cdot\boldsymbol{u}, \tag{2.11}$$

called Euler's second formula.

2.1.2 Reynolds' Transport Theorem

As priorly stated, we proceed to the determination of material derivatives of integrals over current configurations. In this case, the domain of integration depends on time, therefore the derivative and integral cannot be commuted. Instead, first we change the variables of integration, pulling back to the reference configuration. Then, the derivative and integral commute, that is

$$\frac{D}{Dt}\int_{V(t)}G(\boldsymbol{x},t)\,\mathrm{dV}=\int_{V_0}\frac{D}{Dt}\left[G(\boldsymbol{x},t)\det\boldsymbol{\mathcal{F}}\right]\,\mathrm{dV}_0. \tag{2.12}$$

Applying the product rule for derivatives and Euler's second formula, (2.11),

$$\frac{D}{Dt}\int_{V(t)}G(\boldsymbol{x},t)\,\mathrm{dV}=\int_{V_0}\left[\frac{DG}{Dt}+G(\nabla\cdot\boldsymbol{u})\right]\det\boldsymbol{\mathcal{F}}\,\mathrm{dV}_0. \tag{2.13}$$

Rewriting the integral in the current coordinates, we obtain

$$\frac{D}{Dt}\int_{V(t)}G(\boldsymbol{x},t)\,\mathrm{dV}=\int_{V(t)}\left[\frac{DG}{Dt}+G(\nabla\cdot\boldsymbol{u})\right]\,\mathrm{dV}, \tag{2.14}$$

named Reynolds' transport theorem (REYNOLDS; BRIGHTMORE; MOORBY, 1903). An useful variation of it may be obtained by recalling the definition of the material derivative, which yields

$$\frac{D}{Dt}\int_{V(t)}G(\boldsymbol{x},t)\,\mathrm{dV}=\int_{V(t)}\left[\frac{\partial G}{\partial t}+\nabla\cdot(G\boldsymbol{u})\right]\,\mathrm{dV}, \tag{2.15}$$

and applying the divergence theorem,

$$\frac{D}{Dt}\int_{V(t)}G(\boldsymbol{x},t)\,\mathrm{dV}=\int_{V(t)}\frac{\partial G}{\partial t}\,\mathrm{dV}+\int_{S(t)}G\boldsymbol{u}\cdot\hat{\boldsymbol{n}}\,\mathrm{dS}. \tag{2.16}$$

Here, $S(t)$ is the boundary of the volume $V(t)$. We conclude from this equation that the time rate of variation of a property inside a material volume in motion is due to two distinct contributions: a local variation inside the volume, and a flux of the property through the surface.

2.1.3 Continuity Equation

Now that we are in possession of an expression for time derivatives of integrals over material volumes, we can start to inquire how the laws governing integral properties imply equations for corresponding local variables. In the first place, we consider the mass density of a continuum, $\rho(\boldsymbol{x}, t)$. Its corresponding extensive property is the total mass of the body, given by

$$m = \int_V \rho(\boldsymbol{x}, t)\,\mathrm{dV}. \tag{2.17}$$

By the principle of mass conservation, it remains constant during the motion in the absence of chemical reactions or relativistic effects, such that its time derivative is always null,

$$\frac{Dm}{Dt} = 0. \tag{2.18}$$

Applying Reynolds' transport theorem, Eq. (2.14), to Eq. (2.18),

$$\int_V \left(\frac{D\rho}{Dt} + \rho\nabla\cdot\boldsymbol{u}\right)\,\mathrm{dV} = 0. \tag{2.19}$$

Note that this result holds for an arbitrary volume V. Therefore, under the assumption that the integrand is continuous, which is sensible for physical flows, the du Bois-Reymond lemma (PATERSON, 1983) implies that the integrand is null in every point of the domain, i.e., there results

$$\frac{D\rho}{Dt} + \rho\nabla\cdot\boldsymbol{u} = 0, \tag{2.20}$$

denominated the continuity equation.

Another useful variation of Reynolds' transport theorem is obtained by combining it with the continuity equation. Indeed, for an arbitrary field proportional to the mass density, corresponding to $\rho(\boldsymbol{x}, t)G(\boldsymbol{x}, t)$, Eq. (2.14) implies

$$\frac{D}{Dt}\int_V \rho(\boldsymbol{x}, t)G(\boldsymbol{x}, t)\,\mathrm{dV} = \int_V \left[\frac{D(\rho G)}{Dt} + \rho G\nabla\cdot\boldsymbol{u}\right]\,\mathrm{dV}. \tag{2.21}$$

Deriving the product and using Eq. (2.20),

$$\frac{D}{Dt}\int_V \rho(\boldsymbol{x}, t)G(\boldsymbol{x}, t)\,\mathrm{dV} = \int_V \rho\frac{DG}{Dt}\,\mathrm{dV}. \tag{2.22}$$

2.1.4 Balance of Linear Momentum

We derive Cauchy's equation for the balance of linear momentum, which results from Newton's second law applied to the body, i.e., its time rate of change of linear momentum is equal to the sum of external forces acting over it. Those might be body forces, $\boldsymbol{F}_b$, that act from distance, or surface forces, $\boldsymbol{F}_s$, which act upon contact. Hence,

$$\frac{D\boldsymbol{L}}{Dt} = \boldsymbol{F}_b + \boldsymbol{F}_s. \tag{2.23}$$

The linear momentum of a continuum element is $\mathrm{d}\boldsymbol{L} = \rho\boldsymbol{u}\,\mathrm{dV}$, while the body and surface forces over it are respectively $d\boldsymbol{F}_b = \rho\boldsymbol{b}\,\mathrm{dV}$ and $d\boldsymbol{F}_s = \boldsymbol{t}(\boldsymbol{x}, t; \hat{\boldsymbol{n}})\,\mathrm{dS}$, where $\boldsymbol{b}$ is the body field per unit mass and $\boldsymbol{t}(\boldsymbol{x}, t; \hat{\boldsymbol{n}})$ the traction[2], so Eq. (2.23) results in

$$\frac{D}{Dt}\int_V \rho\boldsymbol{u}\,\mathrm{dV} = \int_V \rho\boldsymbol{b}\,\mathrm{dV} + \int_S \boldsymbol{t}\,\mathrm{dS}. \tag{2.24}$$

By Cauchy's hypothesis (ODEN, 2011; BATCHELOR, 2000), the force density is linearly related to the normal vector to the surface by the stress tensor field, $\boldsymbol{t}(\boldsymbol{x}, t; \hat{\boldsymbol{n}}) = \hat{\boldsymbol{n}}\cdot\boldsymbol{\sigma}(\boldsymbol{x}, t)$. Therefore, applying the conservative version of Reynolds' transport theorem, Eq. (2.22),

$$\int_V \rho\frac{D\boldsymbol{u}}{Dt}\,\mathrm{dV} = \int_V \rho\boldsymbol{b}\,\mathrm{dV} + \int_S \hat{\boldsymbol{n}}\cdot\boldsymbol{\sigma}\,\mathrm{dS}. \tag{2.25}$$

In addition, use of the divergence theorem for second-rank tensors permits this equation to be written entirely in terms of volume integrals,

$$\int_V \rho\frac{D\boldsymbol{u}}{Dt}\,\mathrm{dV} = \int_V \rho\boldsymbol{b}\,\mathrm{dV} + \int_V \nabla\cdot\boldsymbol{\sigma}\,\mathrm{dV}, \tag{2.26}$$

whence the localization theorem applies, yielding Cauchy's equation for the balance of linear momentum,

$$\rho\frac{D\boldsymbol{u}}{Dt} = \nabla\cdot\boldsymbol{\sigma} + \rho\boldsymbol{b}. \tag{2.27}$$

In order to determine the continuum motion, closure equations are required for the mass density and the stress tensor. We present the particular equations of this kind for the fluids that concern us in this study. In the case of incompressible flow, the mass density of the fluid is constant along the motion, then Eq. (2.20) implies

$$\nabla\cdot\boldsymbol{u} = 0. \tag{2.28}$$

Moreover, if the fluid is Newtonian, the deviatoric part of its stress tensor is linearly related to the symmetric part of the velocity gradient. Since the incompressibility condition implies the equality of the mechanical pressure and the thermodynamic equilibrium pressure, the stress tensor is written as

$$\boldsymbol{\sigma} = -p\boldsymbol{I} + 2\eta\boldsymbol{d} \tag{2.29}$$

where p is the pressure, η is the dynamic viscosity and $\boldsymbol{d} = (\nabla\boldsymbol{u} + \nabla\boldsymbol{u}^T)/2$. Consequently, it follows from the Eqs. (2.27) to (2.29), with the body field being gravity ($\boldsymbol{b} = \boldsymbol{g}$), that

$$\rho\frac{D\boldsymbol{u}}{Dt} = -\nabla p + \eta\nabla^2\boldsymbol{u} + \rho\boldsymbol{g}. \tag{2.30}$$

This is the Navier-Stokes equation for a Newtonian incompressible fluid.

[2] A surface force density exerted over the fluid.

2.1.5 Particle Pressure

On a side note, while we are talking about constitutive models, we take the opportunity to discuss a central property of our study, the particle pressure. In contrast to our discussion of continuum mechanics, this quantity arises in the kinetic theory of gases. There, macroscopic properties are determined via the analysis of the microscopic motion of particles. We reproduce its derivation of the relation between pressure in gases and the velocity fluctuations tensor of its particles. It is exactly this link that we mean to provide by our numerical investigation, by analogy to kinetic theory, thence the importance of this exposition, based in Chapman and Cowling (1970). A similar analogy is widely used in turbulence, in the Reynolds decomposition of the Navier-Stokes equations, where the turbulent fluctuations promote momentum transfer which enters the stress tensor of the mean flow.

We analyze the exchange of linear momentum in a surface, in order to determine the forces resulting from this interaction and thereby define a particle pressure. The number of particles contained in an infinitesimal volume element is given by its number density times the volume element $n(\boldsymbol{x}, t)\,\mathrm{dV}$. Alternatively, it can be represented using the velocity distribution of these particles, as $\mathrm{d}V \int f(\boldsymbol{x}, \boldsymbol{U}, t)\, d\boldsymbol{U}$, where $\boldsymbol{U}$ is their velocity and f their probability density function. Similarly, the state space average value of an arbitrary tensor property of any rank is given by

$$n\langle G(\boldsymbol{x}, t)\rangle = \int G(\boldsymbol{x}, t) f(\boldsymbol{x}, \boldsymbol{U}, t)\, d\boldsymbol{U}. \tag{2.31}$$

Now consider a stationary wall $\mathrm{d}S$, illustrated by Fig. (7), impinged by all the particles contained in the volume $\mathrm{d}V = (\boldsymbol{U} \cdot \hat{\boldsymbol{n}})\,\mathrm{d}S\,\mathrm{d}t$. In this case, the total number of particles which collides against the surface is precisely the amount contained in the volume,

$$\mathrm{d}S\,\mathrm{d}t \int_{+} (\boldsymbol{U} \cdot \hat{\boldsymbol{n}}) f(\boldsymbol{x}, \boldsymbol{U}, t)\, d\boldsymbol{U}, \tag{2.32}$$

where the symbol $+$ indicates the motion of these particles towards the direction pointed out by the normal vector, arbitrarily chosen as exterior to the domain of fluid. Analogously, the number of particles bounced back by the wall is

$$\mathrm{d}S\,\mathrm{d}t \int_{-} (\boldsymbol{U} \cdot -\hat{\boldsymbol{n}}) f(\boldsymbol{x}, \boldsymbol{U}, t)\, d\boldsymbol{U}. \tag{2.33}$$

We assume that there is no condensation or evaporation over the surface, such that the number of incident particles is equal to that of bounced back. Thus, subtracting Eq. (2.33) from Eq. (2.32), we get

$$\mathrm{d}S\,\mathrm{d}t \left[\int_{+} (\boldsymbol{U} \cdot \hat{\boldsymbol{n}}) f(\boldsymbol{x}, \boldsymbol{U}, t)\, d\boldsymbol{U} - \int_{-} (\boldsymbol{U} \cdot -\hat{\boldsymbol{n}}) f(\boldsymbol{x}, \boldsymbol{U}, t)\, d\boldsymbol{U}\right] = 0, \tag{2.34}$$

or equivalently,

$$\langle \boldsymbol{U} \cdot \hat{\boldsymbol{n}} \rangle = 0. \tag{2.35}$$

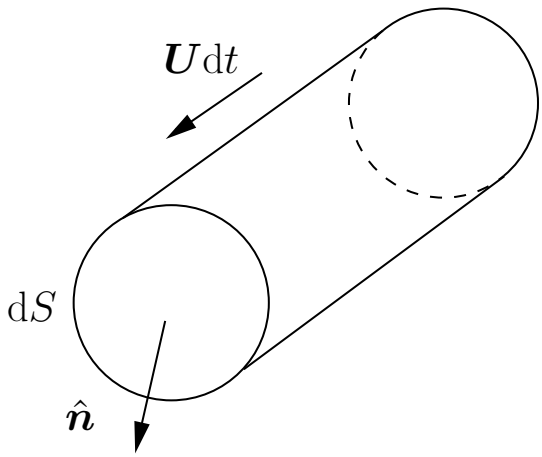

Figure 7 – Volume occupied by the particles which collide against the wall.

Likewise, the linear momentum before the collision is

$$\mathrm{d}S\,\mathrm{d}t \int_{+} \mathcal{M}\boldsymbol{U}(\boldsymbol{U}\cdot\hat{\boldsymbol{n}})f(\boldsymbol{x},\boldsymbol{U},t)\,d\boldsymbol{U} \tag{2.36}$$

and after the collision,

$$\mathrm{d}S\,\mathrm{d}t \int_{-} \mathcal{M}\boldsymbol{U}(\boldsymbol{U}\cdot-\hat{\boldsymbol{n}})f(\boldsymbol{x},\boldsymbol{U},t)\,d\boldsymbol{U}. \tag{2.37}$$

On the other hand, the variation of the linear momentum over the surface is equal to the impulse over it due surface forces, given by

$$-\mathrm{d}S\,\mathrm{d}t\,\boldsymbol{t}(\boldsymbol{x},t;\hat{\boldsymbol{n}}). \tag{2.38}$$

Accordingly, subtracting Eq. (2.37) from (2.36) and equating the result to (2.38), we have

$$-\mathrm{d}S\,\mathrm{d}t\,\boldsymbol{t}(\boldsymbol{x},t) = dS\,dt \int \mathcal{M}\boldsymbol{U}(\boldsymbol{U}\cdot\hat{\boldsymbol{n}})f(\boldsymbol{x},\boldsymbol{U},t)\,d\boldsymbol{U}. \tag{2.39}$$

By Eq. (2.31) and the identity $\rho = \mathcal{M}n$, it follows that

$$\boldsymbol{t} = -\rho\langle(\boldsymbol{U}\cdot\hat{\boldsymbol{n}})\boldsymbol{U}\rangle. \tag{2.40}$$

In terms of the velocity fluctuations, i.e., deviations with respect to the mean, $\boldsymbol{U}' = \boldsymbol{U} - \langle\boldsymbol{U}\rangle$, this result can be rewritten using Eq. (2.35) as

$$\boldsymbol{t} = \hat{\boldsymbol{n}}\cdot\boldsymbol{\sigma}_p, \tag{2.41}$$

where

$$\boldsymbol{\sigma}_p = -\rho\langle\boldsymbol{U}'\boldsymbol{U}'\rangle \tag{2.42}$$

is a stress tensor of hydrodynamic fluctuations, analogous to the Reynolds tensor, relating the stress to velocity fluctuations. From its isotropic and deviatoric parts, a *particle-phase pressure* and a *particle-phase viscosity* may be defined. Also, note how the form of Eq. (2.42) is analogous to that of Cauchy's hypothesis for the traction.

In our context of magnetic suspensions far from equilibrium, we define by analogy a tensor of hydrodynamic fluctuations,

$$\boldsymbol{\sigma}_h = -\phi\rho_s\langle \boldsymbol{U}'\boldsymbol{U}'\rangle, \tag{2.43}$$

where ρ_s is the density of solid particles and ϕ their volume fraction. Indeed, a particle pressure p_p has been defined is gas-solid suspensions as (ABADE; CUNHA, 2007; CUNHA, 1997; BATCHELOR, 1988)

$$p_p = \frac{\phi\rho_s}{3}\langle \boldsymbol{U}' \cdot \boldsymbol{U}'\rangle. \tag{2.44}$$

Moreover, a particle-phase viscosity, which is more seldom explored, may be defined by

$$\eta_p = -\frac{\phi\rho_s}{\dot{\gamma}}\langle U_2' U_3'\rangle \tag{2.45}$$

where $\dot{\gamma}$ is the shear-rate.

2.2 Microhydrodynamics

A fundamental parameter in fluid flows is the Reynolds number, which informs their typical ratio of inertial and viscous forces. In our analysis, it is suitably defined with the particle radius as length scale and its Stokes settling speed as velocity scale as

$$Re = \frac{\rho U_s a}{\eta}. \tag{2.46}$$

In the scope of microhydrodynamics, suitable characteristic scales of the flow are

$$|\boldsymbol{x}| \sim a, \quad |\boldsymbol{u}| \sim U_s, \quad t \sim \frac{a}{U_s} \quad \text{and} \quad p \sim \frac{\eta U_s}{a}. \tag{2.47}$$

In contrast to most common problems in hydrodynamics, the proper scale of the pressure is given by viscous stresses, since these dominate inertial stress in low-Reynolds number flows. In terms of these non-dimensional variables, the Navier-Stokes equation becomes

$$Re\left(\frac{\partial\tilde{\boldsymbol{u}}}{\partial\tilde{t}} + \tilde{\boldsymbol{u}}\cdot\tilde{\nabla}\tilde{\boldsymbol{u}}\right) = -\tilde{\nabla}\tilde{P} + \tilde{\nabla}^2\tilde{\boldsymbol{u}}, \tag{2.48}$$

where the modified pressure is $P = p - \rho\boldsymbol{g}\cdot\boldsymbol{x}$, tacitly accounting for gravitational effects, and non-dimensional variables are indicated by tildes.

In the regime under consideration in this work, the suspension of micron-sized particles is immersed in a slow flow, such that the Reynolds number is low and the inertia of the fluid may be neglected. Therein, Eq. (2.48) reduces to

$$-\nabla P + \eta\nabla^2\boldsymbol{u} = \boldsymbol{0}, \tag{2.49}$$

rewritten in dimensional form, along with the incompressible form of the continuity equation,

$$\nabla\cdot\boldsymbol{u} = \boldsymbol{0}, \tag{2.50}$$

which we repeat here to remind that both equations must be solved simultaneously. This regime is referred to as creeping flow and its governing equations are the Stokes equations.

In this section, we deduce the equations for hydrodynamic forces and torques in the aforementioned regime, accounting for the leading order disturbances which the motion of a particle produces over the others. Our framework is substantiated by the linearity of the Stokes equations. Since the calculation is somewhat lengthy, we outline in advance the sequence of addressed topics and their relevance to the matter.

First we present the formal solution of unbounded Stokes flows with a force density, such as occurs when a particle is immersed in a fluid. Next we specify this solution to a punctual force, which is then used to construct general integral solutions of Stokes flows via the reciprocal theorem. With this integral solution, we can determine the force, torque and stresslet[3] over a particle by Faxén's laws. Then, we show how the velocity disturbance field produced by a particle can be written as a series in the inverse distance, via the multipole expansion, and how we can obtain the matrices which linearly relate the moments of surface traction to dynamical variables of the flow, therefore determining our hydrodynamic forces and torques.

The presentation of the topics is partially based in Kim and Karrila (1991) and Roure (2018).

2.2.1 Formal Solution of Stokes Flows

We start by presenting a solution of the velocity field when the fluid exerts a force density field $\boldsymbol{f}(\boldsymbol{x})$ at each point in its domain. Taking it into account, the Stokes equation acquires the form

$$-\nabla P + \eta \nabla^2 \boldsymbol{u} = \boldsymbol{f}(\boldsymbol{x}). \tag{2.51}$$

Since the velocity field is solenoidal, the divergence of Eq. (2.51) yields an inhomogeneous Poisson equation for the pressure field,

$$\nabla^2 P = -\nabla \cdot \boldsymbol{f}. \tag{2.52}$$

Therefore, taking the laplacian of Eq. (2.51) and using Eq. (2.52), we have

$$\nabla^4 \boldsymbol{u} = \frac{1}{\eta}(\boldsymbol{I}\nabla^2 - \nabla\nabla) \cdot \boldsymbol{f}. \tag{2.53}$$

Bearing in mind that the force density may be written as a convolution integral with the Dirac delta distribution,

$$\boldsymbol{f}(\boldsymbol{x}) = \int_{\mathbb{R}_3} \boldsymbol{f}(\boldsymbol{x}')\delta(\boldsymbol{x} - \boldsymbol{x}')\, d\boldsymbol{x}'. \tag{2.54}$$

Eq. (2.53) then reduces to

$$\nabla^4 \boldsymbol{u} = \frac{1}{\eta} \int_{\mathbb{R}_3} (\boldsymbol{I}\nabla^2 - \nabla\nabla)\delta(\boldsymbol{x} - \boldsymbol{x}') \cdot \boldsymbol{f}(\boldsymbol{x}')\, d\boldsymbol{x}' \tag{2.55}$$

[3] Symmetric part of the first moment of the force over a particle surface.

and setting

$$\nabla^4 H(\boldsymbol{x}-\boldsymbol{x}') = \delta(\boldsymbol{x}-\boldsymbol{x}'), \tag{2.56}$$

its formal solution may be found to be

$$\boldsymbol{u} = \frac{1}{\eta}\int_{\mathbb{R}_3} (\boldsymbol{I}\nabla^2 - \nabla\nabla)H(\boldsymbol{x}-\boldsymbol{x}')\cdot\boldsymbol{f}(\boldsymbol{x}')\,d\boldsymbol{x}'. \tag{2.57}$$

Then we proceed to determine its explicit form by calculating $(\boldsymbol{I}\nabla^2 - \nabla\nabla)H(\boldsymbol{x}-\boldsymbol{x}')$. To this end, note that

$$-\nabla^2\left(\frac{1}{4\pi|\boldsymbol{x}-\boldsymbol{x}'|}\right) = \delta(\boldsymbol{x}-\boldsymbol{x}'), \tag{2.58}$$

so the solution of Eq. (2.56) is

$$H(\boldsymbol{x}-\boldsymbol{x}') = \frac{-|\boldsymbol{x}-\boldsymbol{x}'|}{8\pi}. \tag{2.59}$$

by direct integration of the laplacian in spherical coordinates. We accomplish our goal by applying the aforementioned operator to H, i.e., Eq. (2.57) is explicitly written as

$$\boldsymbol{u} = -\frac{1}{8\pi\eta}\int_{\mathbb{R}_3} \boldsymbol{G}(\boldsymbol{x}-\boldsymbol{x}')\cdot\boldsymbol{f}(\boldsymbol{x}')\,d\boldsymbol{x}', \tag{2.60}$$

where the Green kernel is

$$\boldsymbol{G}(\boldsymbol{x}-\boldsymbol{x}') = (\boldsymbol{I}\nabla^2 - \nabla\nabla)|\boldsymbol{x}-\boldsymbol{x}'| = \frac{\boldsymbol{I}}{|\boldsymbol{x}-\boldsymbol{x}'|} + \frac{(\boldsymbol{x}-\boldsymbol{x}')(\boldsymbol{x}-\boldsymbol{x}')}{|\boldsymbol{x}-\boldsymbol{x}'|^3}, \tag{2.61}$$

also called the Oseen tensor.

2.2.2 Stokes' Fundamental Solution

This fundamental solution corresponds to a force density located at a point $\boldsymbol{x}_0$, physically symbolizing the force exerted over a single particle whose dimensions are negligible. This is a valuable solution because its simple form may be used to solve arbitrary creeping flows via the Reciprocal Lorentz' Theorem, to be presented next. In accordance to the foregoing discussion, we restrict our attention to the case of a localized density force, i.e.,

$$\boldsymbol{f}(\boldsymbol{x}) = \boldsymbol{F}\delta(\boldsymbol{x}-\boldsymbol{x}_0) \tag{2.62}$$

where $\boldsymbol{F}$ is the constant force exerted over the particle. Also, let $\boldsymbol{r} = \boldsymbol{x}-\boldsymbol{x}_0$, $r = |\boldsymbol{r}|$ and $\hat{\boldsymbol{r}} = \boldsymbol{r}/r$. In this case, Eq. (2.61) yields

$$\boldsymbol{u}(\boldsymbol{x}) = -\frac{1}{8\pi\eta}\boldsymbol{G}(\boldsymbol{r})\cdot\boldsymbol{F}. \tag{2.63}$$

This velocity field is referred in the literature as Stokeslet (KIM; KARRILA, 1991). Other quantities which characterize the flow are straightforwardly derived. The pressure field following from Eq. (2.52) is

$$P(\boldsymbol{x}) = \nabla\left(\frac{1}{4\pi r}\right)\cdot\boldsymbol{F} = -\frac{\hat{\boldsymbol{r}}}{4\pi r^2}\cdot\boldsymbol{F}. \tag{2.64}$$

The velocity gradient calculated from Eq. (2.63) is

$$\nabla \boldsymbol{u} = -\frac{1}{8\pi\eta r^2}\left[\boldsymbol{F}\hat{\boldsymbol{r}} - \hat{\boldsymbol{r}}\boldsymbol{F} + (\hat{\boldsymbol{r}}\cdot\boldsymbol{F})\boldsymbol{I} - 3(\hat{\boldsymbol{r}}\cdot\boldsymbol{F})\hat{\boldsymbol{r}}\hat{\boldsymbol{r}}\right], \tag{2.65}$$

such that the corresponding vorticity and stress fields are, respectively

$$\boldsymbol{\xi} = \boldsymbol{\varepsilon} : \nabla \boldsymbol{u} = \frac{1}{4\pi\eta r^2}(\boldsymbol{\varepsilon}\cdot\hat{\boldsymbol{r}})\cdot\boldsymbol{F} \tag{2.66}$$

and

$$\boldsymbol{\sigma} = \frac{3}{4\pi r^2}\hat{\boldsymbol{r}}\hat{\boldsymbol{r}}\hat{\boldsymbol{r}}\cdot\boldsymbol{F}, \tag{2.67}$$

where $\boldsymbol{\varepsilon}$ is the Levi-Civita alternating third-rank tensor. The vorticity and stress fields of a point force are called rotlet and stresslet (KIM; KARRILA, 1991). It is convenient to assign a symbol to the linear operator which produces the stress field, which is, up to a constant,

$$\boldsymbol{\mathcal{T}} = \frac{6}{r^2}\hat{\boldsymbol{r}}\hat{\boldsymbol{r}}\hat{\boldsymbol{r}}. \tag{2.68}$$

With this notation, we have

$$\boldsymbol{\sigma} = \frac{1}{8\pi}\boldsymbol{\mathcal{T}}\cdot\boldsymbol{F}. \tag{2.69}$$

2.2.3 Reciprocal Lorentz' Theorem

Now we derive the reciprocal theorem of Lorentz (1907), which is the integral form of Green's second identity applied to a pair of Stokes flows, $(\boldsymbol{u},\boldsymbol{\sigma})$ and $(\boldsymbol{u}',\boldsymbol{\sigma}')$, defined in the same region V with boundary ∂V. This theorem permits the construction of an integral representation formula for the velocity field of Stokes flows, as we shall show in the next section.

For its proof, consider the Stokes equations of both flows,

$$\nabla\cdot\boldsymbol{\sigma} = \boldsymbol{f}, \qquad \nabla\cdot\boldsymbol{u} = 0 \tag{2.70}$$

and

$$\nabla\cdot\boldsymbol{\sigma}' = \boldsymbol{f}', \qquad \nabla\cdot\boldsymbol{u}' = 0. \tag{2.71}$$

Note that the constitutive equation for the stress tensor of a Newtonian incompressible fluid, Eq. (2.29), yields $\boldsymbol{\sigma} : \nabla\boldsymbol{u}' = 2\eta\,\boldsymbol{d} : \boldsymbol{d}' = \boldsymbol{\sigma}' : \nabla\boldsymbol{u}$, hence the product rule for derivatives along with Eqs. (2.70) and (2.71) for the divergence of the stress tensors yield Lorentz's reciprocal theorem in the differential form,

$$\nabla\cdot(\boldsymbol{\sigma}\cdot\boldsymbol{u}') - \boldsymbol{u}'\cdot\boldsymbol{f} = \nabla\cdot(\boldsymbol{\sigma}'\cdot\boldsymbol{u}) - \boldsymbol{u}\cdot\boldsymbol{f}'. \tag{2.72}$$

Integrating over V, using the divergence theorem and the symmetry of the stress tensor, we obtain the integral form of the theorem, namely

$$\int_{\partial V}\boldsymbol{u}'\cdot\boldsymbol{\sigma}\cdot\hat{\boldsymbol{n}}\,\mathrm{dS} - \int_V \boldsymbol{u}'\cdot\boldsymbol{f}\,\mathrm{dV} = \int_{\partial V}\boldsymbol{u}\cdot\boldsymbol{\sigma}'\cdot\hat{\boldsymbol{n}}\,\mathrm{dS} - \int_V \boldsymbol{u}\cdot\boldsymbol{f}'\,\mathrm{dV}. \tag{2.73}$$

2.2.4 Integral Representation of Stokes Flows

Now we employ Lorentz's reciprocal theorem when $(\boldsymbol{u}', \boldsymbol{\sigma}')$ is the fundamental solution and $(\boldsymbol{u}, \boldsymbol{\sigma})$ is an arbitrary non-singular ($\boldsymbol{f} = \boldsymbol{0}$) Stokes flow. Eqs. (2.73), (2.63) and (2.69) yield

$$-\frac{1}{8\pi\eta}\int_{\partial V} \boldsymbol{G}(\boldsymbol{x}-\boldsymbol{\zeta})\cdot\boldsymbol{\sigma}(\boldsymbol{\zeta})\cdot\hat{\boldsymbol{n}}^*\,\mathrm{d}S_\zeta = \frac{1}{8\pi}\int_{\partial V}\boldsymbol{u}(\boldsymbol{\zeta})\cdot\boldsymbol{\mathcal{T}}(\boldsymbol{x}-\boldsymbol{\zeta})\cdot\hat{\boldsymbol{n}}^*\,\mathrm{d}S_\zeta - \int_V \boldsymbol{u}(\boldsymbol{\zeta})\delta(\boldsymbol{x}-\boldsymbol{\zeta})\,\mathrm{d}V_\zeta, \tag{2.74}$$

where $\mathrm{d}S_\zeta$ and $\mathrm{d}V_\zeta$ denote integrations with respect to the variable $\boldsymbol{\zeta}$. Note that we temporarily denoted the unit normal vector pointing outwards the fluid region by $\hat{\boldsymbol{n}}^*$. This was done since in order to describe the flow outside an immersed particle, it is more convenient to use a normal vector which points outside the particle, thus towards the fluid. Accordingly, in terms of this vector, $\hat{\boldsymbol{n}} = -\hat{\boldsymbol{n}}^*$,

$$\frac{1}{8\pi\eta}\int_{\partial V} \boldsymbol{G}(\boldsymbol{x}-\boldsymbol{\zeta})\cdot\boldsymbol{\sigma}(\boldsymbol{\zeta})\cdot\hat{\boldsymbol{n}}\,\mathrm{d}S_\zeta = -\frac{1}{8\pi}\int_{\partial V}\boldsymbol{u}(\boldsymbol{\zeta})\cdot\boldsymbol{\mathcal{T}}(\boldsymbol{x}-\boldsymbol{\zeta})\cdot\hat{\boldsymbol{n}}\,\mathrm{d}S_\zeta - \int_V \boldsymbol{u}(\boldsymbol{\zeta})\delta(\boldsymbol{x}-\boldsymbol{\zeta})\,\mathrm{d}V_\zeta. \tag{2.75}$$

By the defining property of the Dirac delta distribution,

$$\left.\begin{array}{ll}\text{If} & \boldsymbol{x}\in V, \quad \boldsymbol{u}(\boldsymbol{x})\\ \text{If} & \boldsymbol{x}\notin \bar{V}, \quad \boldsymbol{0}\end{array}\right\} = -\frac{1}{8\pi\eta}\int_{\partial V} \boldsymbol{G}(\boldsymbol{x}-\boldsymbol{\zeta})\cdot\boldsymbol{\sigma}(\boldsymbol{\zeta})\cdot\hat{\boldsymbol{n}}\,\mathrm{d}S_\zeta - \frac{1}{8\pi}\int_{\partial V}\boldsymbol{u}(\boldsymbol{\zeta})\cdot\boldsymbol{\mathcal{T}}(\boldsymbol{x}-\boldsymbol{\zeta})\cdot\hat{\boldsymbol{n}}\,\mathrm{d}S_\zeta, \tag{2.76}$$

where $\bar{V}$ is the closure of V. Eq. (2.76) is the integral representation of Stokes flows, which determines the velocity field exclusively in terms of boundary conditions, given the propagators of the fundamental solution. Therefore, it provides an alternative method to the solution of the PDEs of motion.

The integral representation assumes a more specific form in the case of immersed rigid particles, as we now show. To this end, we analyze a doubly connected region of fluid, illustrated in Fig. (8), which represents the flow around an immersed particle. In this case, the boundary is composed of two disjoint surfaces, S_p and S_∞, the first being the surface of the particle and the latter an imaginary spherical surface of arbitrarily large radius.

Furthermore, we split the velocity field in two distinct contributions, $\boldsymbol{u}(\boldsymbol{x}) = \boldsymbol{u}^D(\boldsymbol{x}) + \boldsymbol{u}^\infty(\boldsymbol{x})$, where $\boldsymbol{u}^D(\boldsymbol{x})$ is the velocity disturbance produced by the presence of the particle and $\boldsymbol{u}^\infty(\boldsymbol{x})$ is the incident undisturbed flow. By this classification, we should have $\boldsymbol{u}^D(\boldsymbol{x}) \to \boldsymbol{0}$ as $|\boldsymbol{x}| \to \infty$ whereas $\boldsymbol{u}(\boldsymbol{x}) \to \boldsymbol{u}^\infty(\boldsymbol{x})$ as $|\boldsymbol{x}| \to \infty$, which motivates us to define

$$\boldsymbol{u}^\infty(\boldsymbol{x}) := -\frac{1}{8\pi\eta}\int_{S_\infty} \boldsymbol{G}(\boldsymbol{x}-\boldsymbol{\zeta})\cdot\boldsymbol{\sigma}(\boldsymbol{\zeta})\cdot\hat{\boldsymbol{n}}\,\mathrm{d}S_\zeta - \frac{1}{8\pi}\int_{S_\infty}\boldsymbol{u}(\boldsymbol{\zeta})\cdot\boldsymbol{\mathcal{T}}(\boldsymbol{x}-\boldsymbol{\zeta})\cdot\hat{\boldsymbol{n}}\,\mathrm{d}S_\zeta. \tag{2.77}$$

The application of the integral representation to the inner points of the region V implies

$$\boldsymbol{u}^D(\boldsymbol{x}) = -\frac{1}{8\pi\eta}\int_{S_p} \boldsymbol{G}(\boldsymbol{x}-\boldsymbol{\zeta})\cdot\boldsymbol{\sigma}(\boldsymbol{\zeta})\cdot\hat{\boldsymbol{n}}\,\mathrm{d}S_\zeta - \frac{1}{8\pi}\int_{S_p}\boldsymbol{u}(\boldsymbol{\zeta})\cdot\boldsymbol{\mathcal{T}}(\boldsymbol{x}-\boldsymbol{\zeta})\cdot\hat{\boldsymbol{n}}\,\mathrm{d}S_\zeta. \tag{2.78}$$

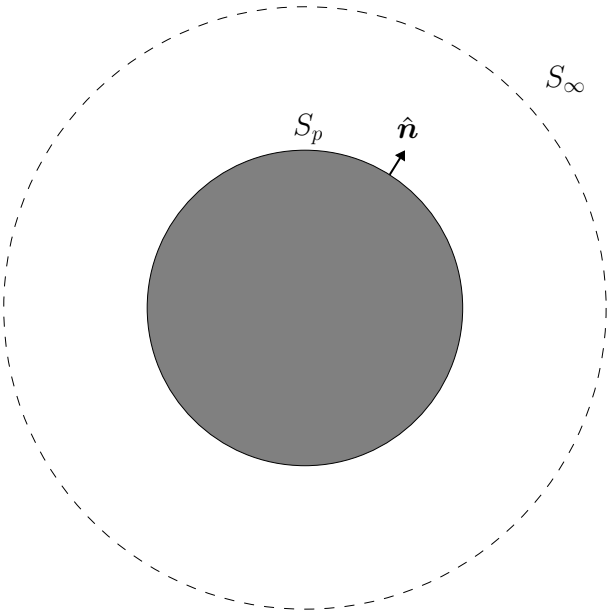

Figure 8 – Boundary of the creeping flow around a rigid particle.

The first integral which appears in Eq. (2.78) may be interpreted as the velocity field generated by a distribution of traction $\boldsymbol{\sigma} \cdot \hat{\boldsymbol{n}}$ over the surface S_p - compare against Eq. (2.60) - and it is thus denominated single layer, in an analogy to electrostatic potential theory (KIM; KARRILA, 1991). The second term is likewise called double layer, however its interpretation is more involved. It can be understood as a distribution of sources or sinks of intensity $\boldsymbol{u} \cdot \hat{\boldsymbol{n}}$ and an actual double layer of Stokeslets with dipole intensity $|\boldsymbol{u}|\hat{\boldsymbol{n}}$ in the direction of $\boldsymbol{u}$ (KIM; KARRILA, 1991).

In the case of rigid particles, which is the one addressed in our study, the double layer term may be shown to be null (KIM; KARRILA, 1991), thus the integral representation reduces to

$$\boldsymbol{u}(\boldsymbol{x}) = \boldsymbol{u}^{\infty}(\boldsymbol{x}) - \frac{1}{8\pi\eta} \int_{S_p} \boldsymbol{G}(\boldsymbol{x} - \boldsymbol{\zeta}) \cdot \boldsymbol{\sigma}(\boldsymbol{\zeta}) \cdot \hat{\boldsymbol{n}} \, \mathrm{d}S_{\zeta}. \tag{2.79}$$

2.2.5 Multipole Expansion

An useful representation for the velocity disturbance field of rigid particles is obtained by expanding the Oseen tensor in a Taylor series. Indeed, since[4]

$$\boldsymbol{G}(\boldsymbol{x} - \boldsymbol{\zeta}) = \boldsymbol{G}(\boldsymbol{x}) - \boldsymbol{\zeta} \cdot \nabla \boldsymbol{G}|_{\boldsymbol{x}} + \frac{\boldsymbol{\zeta}\boldsymbol{\zeta}}{2!} : \nabla\nabla \boldsymbol{G}|_{\boldsymbol{x}} + \cdots, \tag{2.80}$$

it follows from Eq. (2.79) that

$$\boldsymbol{u}^{D}(\boldsymbol{x}) = -\frac{1}{8\pi\eta} \left[\boldsymbol{F} \cdot \boldsymbol{G}(\boldsymbol{x}) - \boldsymbol{\mathcal{D}} : \nabla \boldsymbol{G}(\boldsymbol{x}) + \cdots \right], \tag{2.81}$$

[4] Note that $\boldsymbol{G}(\boldsymbol{x}-\boldsymbol{\zeta}) = \boldsymbol{G}(\boldsymbol{x}) + \boldsymbol{\zeta} \cdot \nabla_{\boldsymbol{\zeta}} \boldsymbol{G}|_{\boldsymbol{x}} + \frac{\boldsymbol{\zeta}\boldsymbol{\zeta}}{2!} : \nabla_{\boldsymbol{\zeta}} \nabla_{\boldsymbol{\zeta}} \boldsymbol{G}|_{\boldsymbol{x}} + \cdots = \boldsymbol{G}(\boldsymbol{x}) - \boldsymbol{\zeta} \cdot \nabla \boldsymbol{G}|_{\boldsymbol{x}} + \frac{\boldsymbol{\zeta}\boldsymbol{\zeta}}{2!} : \nabla\nabla \boldsymbol{G}|_{\boldsymbol{x}} + \cdots$ since $\nabla_{\boldsymbol{\zeta}} = -\nabla_{\boldsymbol{x}}$ by the chain rule.

where

$$\boldsymbol{F} = \int_{S_p} \boldsymbol{t}\,\mathrm{d}S \tag{2.82}$$

is the force over the particle and

$$\boldsymbol{\mathcal{D}} = \int_{S_p} \boldsymbol{\zeta}\boldsymbol{t}\,\mathrm{d}S \tag{2.83}$$

the force dipole. Splitting the dipole into its traceless symmetric, anti-symmetric and isotropic parts, the velocity disturbance may be written as

$$\boldsymbol{u}^D(\boldsymbol{x}) = -\frac{1}{8\pi\eta}\left[\boldsymbol{F}\cdot\boldsymbol{G}(\boldsymbol{x}) - \frac{\boldsymbol{T}}{2}\cdot\left(\nabla\times\boldsymbol{G}\right)(\boldsymbol{x}) - \boldsymbol{S}:\nabla\boldsymbol{G}(\boldsymbol{x}) + \cdots\right]. \tag{2.84}$$

Note that the isotropic part yields a null contribution, since the Oseen tensor is solenoidal. There,

$$\boldsymbol{T} = \int_{S_p} \boldsymbol{\zeta}\times\boldsymbol{t}\,\mathrm{d}S \tag{2.85}$$

is the torque and

$$\boldsymbol{S} = \frac{1}{2}\int_{S_p}\left[\boldsymbol{\zeta}\boldsymbol{t} + \boldsymbol{t}\boldsymbol{\zeta}\right]\,\mathrm{d}S - \frac{1}{3}\int_{S_p}\boldsymbol{\zeta}\cdot\boldsymbol{t}\,\mathrm{d}S\,\boldsymbol{I} \tag{2.86}$$

the stresslet over the particle.

In the case of a single sphere, due to the symmetry of the boundary conditions, the flow produced by its translation only contains a few terms in the multipole expansion. Indeed, bearing in mind that the combination of a Stokes force monopole and a degenerate quadrupole,

$$\left(1 + \frac{a^2}{6}\nabla^2\right)\boldsymbol{G} = \frac{4}{3a}\boldsymbol{I}, \tag{2.87}$$

suffices to meet the boundary condition of rigid body translation, whereas the torque term in the multipole expansion meets a boundary requirement of rigid body rotation, the disturbance field produced by a sphere in rigid body motion is

$$\boldsymbol{u}^D(\boldsymbol{x}) = -\frac{1}{8\pi\eta}\left[\boldsymbol{F}\cdot\left(1 + \frac{a^2}{6}\nabla^2\right)\boldsymbol{G} - \frac{\boldsymbol{T}}{2}\cdot\nabla\times\boldsymbol{G}\right]. \tag{2.88}$$

2.2.6 Faxén's Laws

In this section, we derive Hilding Faxén (1924) laws for the force, torque and stresslet over an isolated rigid sphere in a Stokes flow. Also in this case, the symmetry of the flow results in a multipole expansion which contains only a few terms, yielding closed and useful equations.

We start with the integral representation of the velocity disturbance field produced by the particle, Eq. (2.79). Placing the origin on the sphere centroid, we have that for the points $\boldsymbol{x}$ over the particle surface, the no-slip boundary condition with linear and angular velocities $\boldsymbol{U}$ and $\boldsymbol{\Omega}$, respectively, implies

$$\boldsymbol{U} + \boldsymbol{\Omega}\times\boldsymbol{x} - \boldsymbol{u}^\infty(\boldsymbol{x}) = -\frac{1}{8\pi\eta}\int_{S_p}\boldsymbol{G}(\boldsymbol{x}-\boldsymbol{\zeta})\cdot\boldsymbol{t}(\boldsymbol{\zeta})\,\mathrm{dS}_\zeta. \tag{2.89}$$

Integrating this equation again, this time with respect to $\boldsymbol{x}$, we have

$$\int_{S_p} [\boldsymbol{U} + \boldsymbol{\Omega} \times \boldsymbol{x} - \boldsymbol{u}^\infty(\boldsymbol{x})] \, \mathrm{dS}_{\boldsymbol{x}} = -\frac{1}{8\pi\eta} \int_{S_p} \left[\int_{S_p} \boldsymbol{G}(\boldsymbol{x} - \boldsymbol{\zeta}) \cdot \boldsymbol{t}(\boldsymbol{\zeta}) \, \mathrm{dS}_{\boldsymbol{\zeta}} \right] \mathrm{dS}_{\boldsymbol{x}}. \tag{2.90}$$

Note that the linear and angular velocities of the rigid particle are constant. Furthermore, the integrals of polyadics $\boldsymbol{x} \cdots \boldsymbol{x}$ containing an even number of terms are null due to the sphere symmetry. Also, interchanging the order of integration on the right-hand side,

$$4\pi a^2 \boldsymbol{U} - \int_{S_p} \boldsymbol{u}^\infty(\boldsymbol{x}) \, \mathrm{dS}_{\boldsymbol{x}} = -\frac{1}{8\pi\eta} \int_{S_p} \left[\int_{S_p} \boldsymbol{G}(\boldsymbol{x} - \boldsymbol{\zeta}) \, \mathrm{dS}_{\boldsymbol{x}} \right] \cdot \boldsymbol{t}(\boldsymbol{\zeta}) \, \mathrm{dS}_{\boldsymbol{\zeta}}. \tag{2.91}$$

We profit further from the sphere symmetry by performing Taylor expansions of the ambient velocity field and the Oseen tensor about the center of the sphere and the point $\boldsymbol{\zeta}$, respectively:

$$\boldsymbol{u}^\infty(\boldsymbol{x}) = \boldsymbol{u}^\infty(\boldsymbol{0}) + \boldsymbol{x} \cdot \nabla \boldsymbol{u}^\infty|_{\boldsymbol{0}} + \frac{\boldsymbol{x}\boldsymbol{x}}{2!} : \nabla\nabla \boldsymbol{u}^\infty|_{\boldsymbol{0}} + \cdots \tag{2.92}$$

and[5]

$$\boldsymbol{G}(\boldsymbol{x} - \boldsymbol{\zeta}) = \boldsymbol{G}(\boldsymbol{\zeta}) - \boldsymbol{x} \cdot \nabla_{\boldsymbol{\zeta}} \boldsymbol{G}|_{\boldsymbol{\zeta}} + \frac{\boldsymbol{x}\boldsymbol{x}}{2!} : \nabla_{\boldsymbol{\zeta}} \nabla_{\boldsymbol{\zeta}} \boldsymbol{G}|_{\boldsymbol{\zeta}} + \cdots . \tag{2.93}$$

Then, we apply Eqs. (2.92) and (2.93) to Eq. (2.91). We remind that integrals of odd rank polyadics $\boldsymbol{x} \cdots \boldsymbol{x}$ are zero and remark the following integral: $\int_{S_p} \boldsymbol{x}\boldsymbol{x} \, \mathrm{dS}_{\boldsymbol{x}} = 4\pi a^4 \, \boldsymbol{I}/3$. Also, note $\nabla^{2n} \boldsymbol{u}^\infty = \boldsymbol{0}$ and $\nabla_{\boldsymbol{\zeta}}^{2n} \boldsymbol{G} = \boldsymbol{0}$ for n greater than 1, which follow from Stokes equations. Hence,

$$4\pi a^2 \boldsymbol{U} - 4\pi a^2 \left(1 + \frac{a^2}{6} \nabla^2 \right) \boldsymbol{u}^\infty|_{\boldsymbol{0}} = -4\pi a^2 \frac{1}{8\pi\eta} \int_{S_p} \left(1 + \frac{a^2}{6} \nabla_{\boldsymbol{\zeta}}^2 \right) \boldsymbol{G}|_{\boldsymbol{\zeta}} \cdot \boldsymbol{t}(\boldsymbol{\zeta}) \, \mathrm{dS}_{\boldsymbol{\zeta}}. \tag{2.94}$$

From the definition of the Oseen tensor,

$$\left(1 + \frac{a^2}{6} \nabla_{\boldsymbol{\zeta}}^2 \right) \boldsymbol{G}|_{\boldsymbol{\zeta}} = \frac{4}{3a} \boldsymbol{I}. \tag{2.95}$$

Since the force over the particle is the integral of the traction, Eqs. (2.94) and (2.95) result in Faxén's law for the force over rigid spherical particles,

$$\boldsymbol{F} = 6\pi\eta a \left[\left(1 + \frac{a^2}{6} \nabla^2 \right) \boldsymbol{u}^\infty|_{\boldsymbol{0}} - \boldsymbol{U} \right]. \tag{2.96}$$

Faxén's laws for torque and stresslet are similarly obtained. The same procedure is repeated for the first moment of the integral representation for the velocity disturbance. Indeed, taking the tensor product of $\boldsymbol{x}$ and Eq. (2.89),

$$\boldsymbol{x}\boldsymbol{U} + \boldsymbol{x}(\boldsymbol{\Omega} \times \boldsymbol{x}) - \boldsymbol{x}\boldsymbol{u}^\infty(\boldsymbol{x}) = -\frac{1}{8\pi\eta} \, \boldsymbol{x} \int_{S_p} \boldsymbol{G}(\boldsymbol{x} - \boldsymbol{\zeta}) \cdot \boldsymbol{t}(\boldsymbol{\zeta}) \, \mathrm{dS}_{\boldsymbol{\zeta}}. \tag{2.97}$$

[5] Similarly to the previous Taylor expansion, $\boldsymbol{G}(\boldsymbol{x} - \boldsymbol{\zeta}) = \boldsymbol{G}(\boldsymbol{\zeta} - \boldsymbol{x}) = \boldsymbol{G}(\boldsymbol{\zeta}) + \boldsymbol{x} \cdot \nabla_{\boldsymbol{x}} \boldsymbol{G}|_{\boldsymbol{\zeta}} + \frac{\boldsymbol{x}\boldsymbol{x}}{2!} : \nabla_{\boldsymbol{x}} \nabla_{\boldsymbol{x}} \boldsymbol{G}|_{\boldsymbol{\zeta}} + \cdots = \boldsymbol{G}(\boldsymbol{x}) - \boldsymbol{x} \cdot \nabla_{\boldsymbol{\zeta}} \boldsymbol{G}|_{\boldsymbol{\zeta}} + \frac{\boldsymbol{x}\boldsymbol{x}}{2!} : \nabla_{\boldsymbol{\zeta}} \nabla_{\boldsymbol{\zeta}} \boldsymbol{G}|_{\boldsymbol{\zeta}} + \cdots$ since $\nabla_{\boldsymbol{\zeta}} = -\nabla_{\boldsymbol{x}}$ by the chain rule.

Integrating once again over the sphere surface and commuting integrals over $\boldsymbol{x}$ and $\boldsymbol{\zeta}$,

$$\int_{S_p} [\boldsymbol{x}\boldsymbol{U} + \boldsymbol{x}(\boldsymbol{\Omega}\times\boldsymbol{x}) - \boldsymbol{x}\boldsymbol{u}^\infty(\boldsymbol{x})]\,\mathrm{dS} = -\frac{1}{8\pi\eta}\int_{S_p}\left[\int_{S_p}\boldsymbol{x}\boldsymbol{G}(\boldsymbol{x}-\boldsymbol{\zeta})\,\mathrm{dS}_{\boldsymbol{x}}\right]\cdot\boldsymbol{t}(\boldsymbol{\zeta})\,\mathrm{dS}_{\boldsymbol{\zeta}}. \quad (2.98)$$

This calculation is more conveniently written in index notation, as

$$\int_{S_p} [x_i U_j + x_i\varepsilon_{jkl}\Omega_k x_l - x_i u_j^\infty(\boldsymbol{x})]\,\mathrm{dS} = -\frac{1}{8\pi\eta}\int_{S_p}\left[\int_{S_p} x_i G_{jk}(\boldsymbol{x}-\boldsymbol{\zeta})\,\mathrm{dS}_{\boldsymbol{x}}\right] t_k(\boldsymbol{\zeta})\,\mathrm{dS}_{\boldsymbol{\zeta}}. \quad (2.99)$$

Now, the ambient velocity field and the Oseen tensor are expanded in Taylor series,

$$u_j^\infty(\boldsymbol{x}) = u_j^\infty(\boldsymbol{0}) + x_l\partial_l u_j^\infty(\boldsymbol{0}) + \frac{1}{2!}\,x_m x_l\partial_m\partial_l u_j^\infty(\boldsymbol{0}) + \frac{1}{3!}\,x_p x_m x_l\partial_p\partial_m\partial_l u_j^\infty(\boldsymbol{0})\cdots \quad (2.100)$$

and

$$G_{jk}(\boldsymbol{x}-\boldsymbol{\zeta}) = G_{jk}(\boldsymbol{\zeta}) - x_l\partial_l G_{jk}(\boldsymbol{\zeta}) + \frac{1}{2!}x_l x_m\partial_l\partial_m G_{jk}(\boldsymbol{\zeta}) - \frac{1}{3!}x_p x_l x_m\partial_p\partial_l\partial_m G_{jk}(\boldsymbol{\zeta}) + \cdots. \quad (2.101)$$

Integrals of polyadics of the position components appear when substituting these expansions back in the integral representation. Thus, the following identities are noteworthy

$$\int_{S_p} x_i x_j\,\mathrm{dS}_{\boldsymbol{x}} = \frac{4\pi a^4}{3}\delta_{ij} \quad (2.102)$$

and

$$\int_{S_p} x_i x_j x_k x_l\,\mathrm{dS}_{\boldsymbol{x}} = \frac{4\pi a^6}{15}(\delta_{ij}\delta_{kl} + \delta_{ik}\delta_{jl} + \delta_{il}\delta_{jk}), \quad (2.103)$$

whereas integrals of an odd number of position components vanish. It follows from Eqs. (2.99) to (2.103) that

$$\varepsilon_{ijk}\Omega_k - \left(1 + \frac{a^2}{10}\nabla^2\right)\partial_i u_j^\infty(\boldsymbol{0}) = \frac{1}{8\pi\eta}\int_{S_p}\left(1 + \frac{a^2}{10}\nabla^2\right)\partial_i G_{jk}(\boldsymbol{\zeta})t_k(\boldsymbol{\zeta})\,\mathrm{dS}_{\boldsymbol{\zeta}}. \quad (2.104)$$

The combination of terms involving the Oseen tensor can be written over the sphere surface as

$$\left(1 + \frac{a^2}{10}\nabla^2\right)\partial_i G_{jk}(\boldsymbol{\zeta})t_k(\boldsymbol{\zeta}) = \frac{2}{5a^3}(\delta_{ij}\zeta_k + \delta_{ik}\zeta_j - 4\delta_{jk}\zeta_i), \quad (2.105)$$

therefore Eq. (2.104) is equivalent to

$$8\pi\eta\left[\varepsilon_{ijk}\Omega_k - \left(1 + \frac{a^2}{10}\nabla^2\right)\partial_i u_j^\infty(\boldsymbol{0})\right] = \frac{2}{5a^3}\int_{S_p}(\zeta_k t_k\delta_{ij} + t_i\zeta_j - 4\zeta_i t_j)\,\mathrm{dS}_{\boldsymbol{\zeta}}. \quad (2.106)$$

Back to Gibbs notation,

$$8\pi\eta\left[\boldsymbol{\varepsilon}\cdot\boldsymbol{\Omega} - \left(1 + \frac{a^2}{10}\nabla^2\right)\nabla\boldsymbol{u}^\infty(\boldsymbol{0})\right] = \frac{2}{5a^3}\int_{S_p}[(\boldsymbol{\zeta}\cdot\boldsymbol{t})\,\boldsymbol{I} + \boldsymbol{t}\boldsymbol{\zeta} - 4\boldsymbol{\zeta}\boldsymbol{t}]\,\mathrm{dS}_{\boldsymbol{\zeta}}. \quad (2.107)$$

Both of the Faxén laws for torque and stresslet can be retrieved from Eq. (2.107). Its anti-symmetrical part yields the relation

$$8\pi\eta a^3\left[\left(1 + \frac{a^2}{10}\nabla^2\right)\boldsymbol{W}^\infty(\boldsymbol{0}) - \boldsymbol{\varepsilon}\cdot\boldsymbol{\Omega}\right] = 2\boldsymbol{\tau} \quad (2.108)$$

where $\boldsymbol{W}^{\infty}$ is the anti-symmetric part of the ambient flow velocity gradient and

$$\boldsymbol{\tau} = \frac{1}{2}\int_{S_p} (\boldsymbol{\zeta t} - \boldsymbol{t\zeta})\,\mathrm{dS}_{\zeta}. \tag{2.109}$$

Contracting Eq. (2.108) with the Levi-Civita alternating tensor,

$$\boldsymbol{T} = 8\pi\eta a^3 \left[\frac{\nabla \times \boldsymbol{u}^{\infty}(\boldsymbol{0})}{2} - \boldsymbol{\Omega}\right] \tag{2.110}$$

since the Laplacian of ambient vorticity field vanishes, in compliance to the Stokes flow equation. Furthermore, the symmetrical part of the (2.107) yields

$$\boldsymbol{S} = \frac{20\pi\eta a^3}{3}\left(1 + \frac{a^2}{10}\nabla^2\right)\boldsymbol{E}^{\infty}|_{\boldsymbol{0}} \tag{2.111}$$

where $\boldsymbol{E}^{\infty}$ is the symmetrical part of the ambient velocity gradient and

$$\boldsymbol{S} = \frac{1}{2}\int_{S_p} (\boldsymbol{\zeta t} + \boldsymbol{t\zeta})\,\mathrm{dS}_{\zeta} - \frac{1}{3}\int_{S_p} [(\boldsymbol{\zeta}\cdot\boldsymbol{t})\boldsymbol{I}]\,\mathrm{dS}_{\zeta} \tag{2.112}$$

is the symmetrical traceless part of the force dipole.

2.2.7 Mobility and Resistance Formulations

At this point, we wish to derive equations for the hydrodynamic force and torque over each particle in a dilute suspension, accounting for hydrodynamic interactions. The linearity of the Stokes equations is crucial in this process since it furnishes linear relations between dynamic and kinematic variables of the flow. In a quiescent flow, these amount to (KIM; KARRILA, 1991)

$$\begin{bmatrix} \boldsymbol{U}_1 \\ \vdots \\ \boldsymbol{U}_N \\ \boldsymbol{\Omega}_1 \\ \vdots \\ \boldsymbol{\Omega}_N \end{bmatrix} = -\eta^{-1} \begin{bmatrix} \mathbf{a}_{11} & \cdots & \mathbf{a}_{1N} & \boldsymbol{b}_{11} & \cdots & \boldsymbol{b}_{1N} \\ \vdots & \ddots & \vdots & \vdots & \ddots & \vdots \\ \mathbf{a}_{N1} & \cdots & \mathbf{a}_{NN} & \boldsymbol{b}_{N1} & \cdots & \boldsymbol{b}_{NN} \\ \mathbf{b}_{11} & \cdots & \mathbf{b}_{1N} & \mathbf{c}_{11} & \cdots & \mathbf{c}_{1N} \\ \vdots & \ddots & \vdots & \vdots & \ddots & \vdots \\ \mathbf{b}_{N1} & \cdots & \mathbf{b}_{NN} & \mathbf{c}_{N1} & \cdots & \mathbf{c}_{NN} \end{bmatrix} \begin{bmatrix} \boldsymbol{F}_1 \\ \vdots \\ \boldsymbol{F}_N \\ \boldsymbol{T}_1 \\ \vdots \\ \boldsymbol{T}_N \end{bmatrix}, \tag{2.113}$$

where the upper indices denote the particle to which the variable relates. There, $\mathbf{a}_{ij}$, $\boldsymbol{b}_{ij}$, $\mathbf{b}_{ij}$ and $\mathbf{c}_{ij}$ are second-rank tensors which together form the mobility matrix. In this form, the linear relation is called the mobility formulation.

Knowledge of the mobility matrix enables the determination of the hydrodynamic forces and torques over the particles via inversion of Eq. (2.113), once the linear and angular velocities are known. In this inverted form, where the forces and torques are the dependent variables, the linear relation is named the resistance formulation. In this form, the equations for force and torque are often written as

$$\boldsymbol{F}_i = -\sum_{j=1}^{N} (\boldsymbol{\zeta}_{ij}^{TT}\cdot\boldsymbol{U}_j + \boldsymbol{\zeta}_{ij}^{TR}\cdot\boldsymbol{\Omega}_j) \tag{2.114}$$

and

$$\boldsymbol{T}_i = -\sum_{j=1}^{N}(\boldsymbol{\zeta}_{ij}^{RT} \cdot \boldsymbol{U}_j + \boldsymbol{\zeta}_{ij}^{RR} \cdot \boldsymbol{\Omega}_j), \tag{2.115}$$

where $\boldsymbol{\zeta}_{ij}$ are resistance matrices, associated to translation or rotation according to the indices T and R. This formula emphasizes the linear dependence of the dynamical variables on the boundary values of the kinematic variables. Despite this linear dependence, it is the coupling between the equations of motion of all the particles which precludes analytical solutions of their ODEs of motion. The resistance formulation is the natural setting for determining the motion of immersed particles since it permits the solution of initial value problems, albeit numerically.

We remark that the forces and torques over the particles, given by Eqs. (2.114) and (2.115), are sufficient for the simulations of the immersed particles. Indeed, the flow produced around them is the sum of their hydrodynamic disturbances, which is a solution of the Stokes equations, Eqs. (2.50) and (2.51). See Cunha et al. (2002) for a picture of the fluid velocity field found in numerical simulations of non-magnetic particles.

2.2.8 Method of Reflections

The method of reflections is a scheme to determine the asymptotic expansions for the generalized forces, or equivalently for the generalized velocities, over a system of hydrodynamically interacting particles in terms of the inverse distances between them. It can be cast in the mobility or in the resistance formulation, but the former converges more quickly, therefore we employ it. Furthermore, its inversion yields the generalized forces, which we seek.

In the chosen formulation, the method works as follows: suppose that the forces and torques over the particles are known, as well as the ambient flow in which they are immersed. Then, we generate a sequence of particle linear and angular velocities satisfying the Stokes equations, $(\{\boldsymbol{U}_i^k\}, \{\boldsymbol{\Omega}_i^k\})$, for every particle $i = 1, \cdots, N$, and the sequence index k ranges over the natural numbers.

We construct the zeroth term of the sequence as the correct solution *in the absence of hydrodynamic interactions* under the known generalized forces. In the next step, we take the new ambient flow over a given particle to be the sum of the original flow and the velocity disturbances produced by all other particles in it, i.e., we *reflect* their velocity disturbances. We also impose the nullity of the forces and torques over the particle from this step on, so that their values, already correct in the zeroth order, remain unaltered.

Then, the generalized velocities of the current step are found by Faxén's first and second laws, with null forces and torques. For every higher order reflection, the procedure is repeated, furnishing the next terms in the sequence. The sum of the series of linear or angular velocities provides the actual linear or angular velocities, all reflections considered.

In practice, especially when the suspension is dilute, so that the particles are on average far apart, the series can be truncated at a suitable order in the inverse distance, yielding an asymptotic approximation to the velocities. The relation is then inverted to obtain approximate generalized forces in terms of the generalized velocities. The process is depicted by Fig. (9) and exemplified by its application to our case of interest, the determination of a first-order correction to the forces and torques due to hydrodynamic interactions.

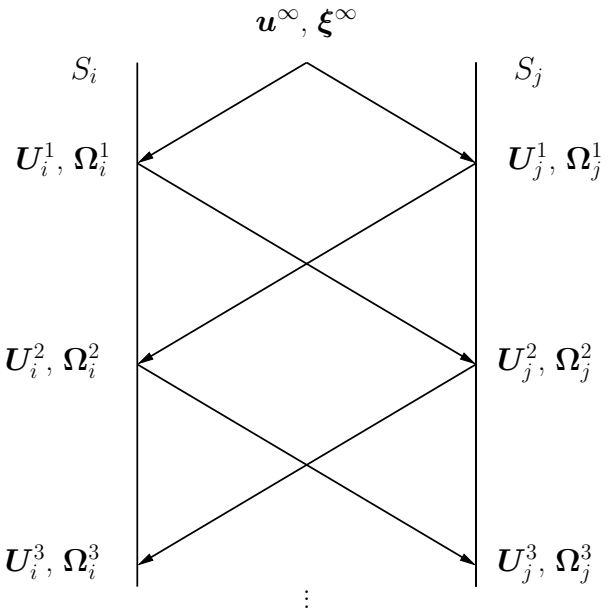

Figure 9 – Reflections of the velocity disturbances over the surfaces S_i and S_j corresponding to the particles i and j. Adapted from Kim and Karrila (1991).

In our analysis, the particles settle in a quiescent fluid, therefore the original ambient velocity and vorticity fields are null. It follows from Faxén's first and second laws, Eqs. (2.96) and (2.110) that the force and torque over each particle are

$$\boldsymbol{F}_i = \boldsymbol{F}_i^0 = -6\pi\eta a_i \boldsymbol{U}_i^0 \tag{2.116}$$

where a_i is radius of the particle i and

$$\boldsymbol{T}_i = \boldsymbol{T}_i^0 = -8\pi\eta a_i^3 \boldsymbol{\Omega}_i^0. \tag{2.117}$$

Now, for the first reflection, we have

$$\boldsymbol{F}_i^1 = 6\pi\eta a_i \left[\sum_{\substack{j=1 \\ j\neq i}}^{N} \left(1 + \frac{a_i^2}{6}\nabla^2\right) \boldsymbol{u}_j(\boldsymbol{x}_i) - \boldsymbol{U}_i^1 \right] = \boldsymbol{0}. \tag{2.118}$$

Furthermore, the velocity disturbance produced by each particle in rigid body motion is given by Eqs. (2.88) and (2.61) as

$$\boldsymbol{u}_j(\boldsymbol{x}_i) = -\frac{1}{8\pi\eta r_{ji}} \left[\boldsymbol{I} + \hat{\boldsymbol{r}}_{ji}\hat{\boldsymbol{r}}_{ji} + \frac{a_j^2}{3r_{ji}^2} \left(\boldsymbol{I} - 3\hat{\boldsymbol{r}}_{ji}\hat{\boldsymbol{r}}_{ji}\right) \right] \cdot \boldsymbol{F}_j + \frac{\boldsymbol{T}_j}{8\pi\eta} \times \nabla \left(\frac{1}{r_{ji}} \right). \tag{2.119}$$

Applying this result to Eq. (2.118), noting that $\nabla^4 \boldsymbol{G}$ and $\nabla \times \nabla^2 \boldsymbol{G}$ are both null,

$$\boldsymbol{U}_i^1 = \sum_{\substack{j=1 \\ j\neq i}}^{N} \left\{ -\frac{1}{8\pi\eta r_{ji}} \left[\boldsymbol{I} + \hat{\boldsymbol{r}}_{ji}\hat{\boldsymbol{r}}_{ji} + \frac{a_i^2 + a_j^2}{3r_{ji}^2} \left(\boldsymbol{I} - 3\hat{\boldsymbol{r}}_{ji}\hat{\boldsymbol{r}}_{ji} \right) \right] \cdot \boldsymbol{F}_j + \frac{\boldsymbol{\varepsilon} \cdot \hat{\boldsymbol{r}}_{ji}}{8\pi\eta r_{ji}^2} \cdot \boldsymbol{T}_j \right\}. \tag{2.120}$$

Similarly, the angular velocities due to the first reflection follow from Faxén's second law as

$$\boldsymbol{T}_i^1 = 8\pi\eta a_i^3 \left(\sum_{\substack{j=1 \\ j\neq i}}^{N} \frac{\boldsymbol{\xi}_j(\boldsymbol{x}_i)}{2} - \boldsymbol{\Omega}_i^1 \right) = \boldsymbol{0}. \tag{2.121}$$

Taking into account the nullity of $\nabla \times \nabla^2 \boldsymbol{G}$ once more, we note that the degenerate quadrupole does not contribute to the vorticity of the ambient flow. Indeed, the curl of (2.119) yields a rotlet, given by Eq. (2.66), and a torque related term, which may be simplified to

$$\boldsymbol{\xi}_j(\boldsymbol{x}_i) = \frac{\boldsymbol{\varepsilon} \cdot \hat{\boldsymbol{r}}_{ji}}{4\pi\eta r_{ji}^2} \cdot \boldsymbol{F}_j - \frac{1}{8\pi\eta r_{ji}^3} (\boldsymbol{I} - 3\hat{\boldsymbol{r}}_{ji}\hat{\boldsymbol{r}}_{ji}) \cdot \boldsymbol{T}_j, \tag{2.122}$$

thus Eq. (2.121) implies

$$\boldsymbol{\Omega}_i^1 = \sum_{\substack{j=1 \\ j\neq i}}^{N} \left[\frac{\boldsymbol{\varepsilon} \cdot \hat{\boldsymbol{r}}_{ji}}{8\pi\eta r_{ji}^2} \cdot \boldsymbol{F}_j - \frac{1}{16\pi\eta r_{ji}^3} (\boldsymbol{I} - 3\hat{\boldsymbol{r}}_{ji}\hat{\boldsymbol{r}}_{ji}) \cdot \boldsymbol{T}_j \right]. \tag{2.123}$$

Gathering the results of the zeroth and first orders, we get

$$\boldsymbol{U}_i = -\frac{\boldsymbol{I} \cdot \boldsymbol{F}_i}{6\pi\eta a_i} - \sum_{\substack{j=1 \\ j\neq i}}^{N} \left\{ \frac{1}{8\pi\eta r_{ji}} \left[\boldsymbol{I} + \hat{\boldsymbol{r}}_{ji}\hat{\boldsymbol{r}}_{ji} + \frac{a_i^2 + a_j^2}{3r_{ji}^2} \left(\boldsymbol{I} - 3\hat{\boldsymbol{r}}_{ji}\hat{\boldsymbol{r}}_{ji} \right) \right] \cdot \boldsymbol{F}_j - \frac{\boldsymbol{\varepsilon} \cdot \hat{\boldsymbol{r}}_{ji}}{8\pi\eta r_{ji}^2} \cdot \boldsymbol{T}_j \right\} \tag{2.124}$$

and

$$\boldsymbol{\Omega}_i = -\frac{\boldsymbol{I} \cdot \boldsymbol{T}_i}{8\pi\eta a_i^3} - \sum_{\substack{j=1 \\ j\neq i}}^{N} \left[-\frac{\boldsymbol{\varepsilon} \cdot \hat{\boldsymbol{r}}_{ji}}{8\pi\eta r_{ji}^2} \cdot \boldsymbol{F}_j + \frac{1}{16\pi\eta r_{ji}^3} (\boldsymbol{I} - 3\hat{\boldsymbol{r}}_{ji}\hat{\boldsymbol{r}}_{ji}) \cdot \boldsymbol{T}_j \right], \tag{2.125}$$

whence it follows that the mobility matrix is formed by the blocks

$$\mathbf{a}_{ii} = \frac{\boldsymbol{I}}{6\pi\eta a_i}, \tag{2.126}$$

$$\mathbf{a}_{ij} = \frac{1}{8\pi\eta r_{ji}} \left[\boldsymbol{I} + \hat{\boldsymbol{r}}_{ji}\hat{\boldsymbol{r}}_{ji} + \frac{a_i^2 + a_j^2}{3r_{ji}^2} \left(\boldsymbol{I} - 3\hat{\boldsymbol{r}}_{ji}\hat{\boldsymbol{r}}_{ji} \right) \right], \quad j \neq i, \tag{2.127}$$

$$\boldsymbol{b}_{ii} = \boldsymbol{0}, \tag{2.128}$$

$$\boldsymbol{b}_{ij} = -\frac{\boldsymbol{\varepsilon} \cdot \hat{\boldsymbol{r}}_{ji}}{8\pi\eta r_{ji}^2}, \quad j \neq i, \tag{2.129}$$

$$\mathbf{b}_{ii} = \mathbf{0}, \tag{2.130}$$

$$\mathbf{b}_{ij} = -\frac{\boldsymbol{\varepsilon} \cdot \hat{\boldsymbol{r}}_{ji}}{8\pi\eta r_{ji}^2}, \quad j \neq i, \tag{2.131}$$

$$\mathbf{c}_{ii} = \frac{\boldsymbol{I}}{8\pi\eta a_i^3} \tag{2.132}$$

and

$$\mathbf{c}_{ij} = \frac{1}{16\pi\eta r_{ji}^3}(\boldsymbol{I} - 3\hat{\boldsymbol{r}}_{ji}\hat{\boldsymbol{r}}_{ji}), \quad j \neq i. \tag{2.133}$$

2.3 Electrodynamics

2.3.1 Maxwell's Equations

In order to calculate the forces which arise from dipolar interaction, it is necessary to describe the electric and magnetic fields produced by magnetic dipoles. Furthermore, the particles in a magnetic suspension are often subject to a force exerted by a magnet, whose magnetic field must be derived. Thus, one must resort to Maxwell's equations. These equations may be demonstrated by assuming the validity of Coulomb's law of the force between charged particles and requiring invariance to the Lorentz's transformations (SCHWARTZ, 2012). Their microscopic form is

$$\nabla \cdot \boldsymbol{e} = \frac{\varrho}{\varepsilon_0}, \tag{2.134}$$

$$\nabla \cdot \boldsymbol{b} = 0, \tag{2.135}$$

$$\nabla \times \boldsymbol{e} = -\frac{\partial \boldsymbol{b}}{\partial t}, \tag{2.136}$$

$$\nabla \times \boldsymbol{b} = \mu_0 \boldsymbol{j} + \mu_0 \varepsilon_0 \frac{\partial \boldsymbol{e}}{\partial t} \tag{2.137}$$

in SI units. Here, $\boldsymbol{e}$ is the electric field, $\boldsymbol{b}$ the magnetic induction, ϱ the electric charge density, $\boldsymbol{j}$ the current density, ε_0 the vacuum permittivity and μ_0 the vacuum permeability. Lowercase letters are used in the aforementioned fields to denote their microscopic character.

With the purpose of applying Eqs. (2.134) to (2.137) to dielectric media, one spatially averages them, smoothing out their rapidly fluctuating microscopic properties and consequently obtaining Maxwell's macroscopic equations[6] (JACKSON, 2012; GROOT; SUTTORP, 1972). In performing the referred averages, a Taylor series expansion of the local properties leads to the appearance of averages of the charge density multipoles in the macroscopic equations. Those contributions are related to the charge density distribution, hence are bulk properties of the medium (JACKSON, 2012). They are comprised

[6] Note that capital letters are used for macroscopic variables thereafter, to distinguish them from their microscopic equivalents, where there are any.

in the electric displacement $\boldsymbol{D}_e$ and magnetic field $\boldsymbol{H}$, which are called derived fields of the fundamental fields $\boldsymbol{E}$ and $\boldsymbol{B}$. To first order, we have

$$\boldsymbol{D}_e = \varepsilon_0 \boldsymbol{E} + \boldsymbol{P}, \tag{2.138}$$

where $\boldsymbol{P}$ is the electric polarization vector and

$$\boldsymbol{B} = \mu_0(\boldsymbol{M} + \boldsymbol{H}), \tag{2.139}$$

in which $\boldsymbol{M}$ is the magnetization, the average of the magnetic dipole moments. Thus, the macroscopic equations obtained are (GROOT; SUTTORP, 1972)

$$\nabla \cdot \boldsymbol{D}_e = \rho_e, \tag{2.140}$$

$$\nabla \cdot \boldsymbol{B} = 0, \tag{2.141}$$

$$\nabla \times \boldsymbol{E} = -\frac{\partial \boldsymbol{B}}{\partial t}, \tag{2.142}$$

$$\nabla \times \boldsymbol{H} = \boldsymbol{J}_f + \frac{\partial \boldsymbol{D}_e}{\partial t}, \tag{2.143}$$

ρ_e being the free electric charge.

Inasmuch as the scope of this dissertation is the study of magnetic dipolar interaction in a creeping flow of a non-conducting carrier fluid, transient effects are negligible and the free charge distribution is null, so we restrict ourselves to the magnetostatic limit of Maxwell's macroscopic equations, that is, permanent regime with $\boldsymbol{J}_f = \boldsymbol{0}$, $\boldsymbol{D}_e = \boldsymbol{0}$, $\boldsymbol{P} = \boldsymbol{0}$ and $\rho_e = 0$, such that only the following equations ought to be satisfied

$$\nabla \cdot \boldsymbol{B} = 0, \tag{2.144}$$

$$\nabla \times \boldsymbol{H} = \boldsymbol{0}. \tag{2.145}$$

The irrotationality of $\boldsymbol{H}$ implies that it can be written as the gradient of a magnetic potential function,

$$\boldsymbol{H} = -\nabla\varphi. \tag{2.146}$$

Furthermore, combining Eqs. (2.139), (2.144) and (2.146), it follows that

$$\nabla^2\varphi = \nabla \cdot \boldsymbol{M}. \tag{2.147}$$

This is a Poisson equation, which is linear, hence our approach is to develop a general solution in unbounded space from the fundamental solution, where the forcing is related to a delta distribution.

Now that the governing equations have been presented, we should discuss their boundary conditions. They are obtained by integrals of the differential equation over infinitesimal pillboxes which comprise both sides of a surface, illustrated in Fig. (10). Firstly we will integrate Eq. (2.144) using the divergence theorem. We take the limit as sides of the contour aligned with the normal vector shrink to zero, so that they do not

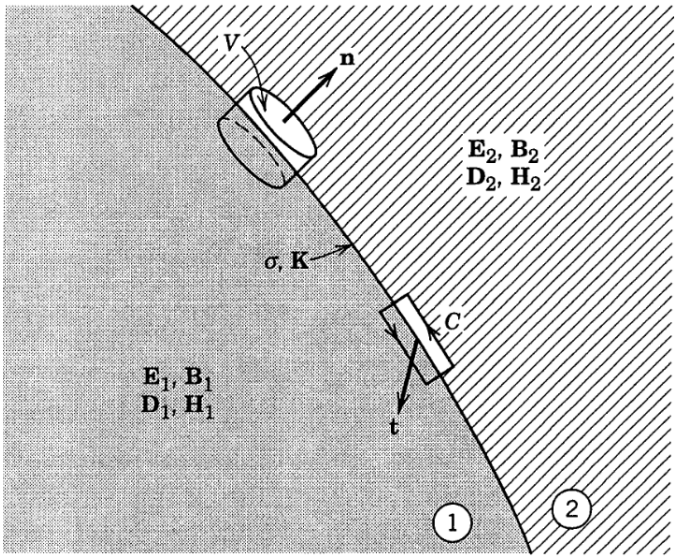

Figure 10 – A surface which separates two magnetically different media, 1 and 2 (JACKSON, 2012). The pillboxes illustrate the integration regions for the determination of boundary conditions.

contribute to the integral, and afterwards take the limit where the upper and lower areas of the volume go to zero, thereby obtaining

$$\boldsymbol{B}_1 \cdot \hat{\boldsymbol{n}} = \boldsymbol{B}_2 \cdot \hat{\boldsymbol{n}}, \tag{2.148}$$

i.e., the normal component of $\boldsymbol{B}$ is continuous. Then, we proceed likewise using Stokes' theorem to integrate Eq. (2.145), taking firstly the limit of vanishing normally oriented segments of the contour, and afterwards shrinking the rest of the contour to zero. There results

$$\boldsymbol{H}_1 \times \hat{\boldsymbol{n}} = \boldsymbol{H}_2 \times \hat{\boldsymbol{n}}, \tag{2.149}$$

that is, the tangential component of the derived field $\boldsymbol{H}$ is continuous.

2.3.2 Effects of Magnetic Fields over Matter

The physics of magnetic suspensions centers around the response of the immersed particles to external fields. Matter in general may present various responses according to its composition. In this section, we present briefly some classes of magnetic materials according to their response to a field in order to specify what kind of immersed particles are taken into consideration as well as how they interact with the external field and with one another.

In any case, the net effect of these interactions is to alter the magnetization, i.e., the average of magnetic moment dipoles, according to the preceding discussion of Sec. (2.3.1). From the standpoint of continuum mechanics, the magnetization can be interpreted as the volume average in the sensitive volume $\delta V_{\boldsymbol{x}}^*$ which surrounds the point $\boldsymbol{x}$. Regarding

the particles in this average as point dipoles (CUNHA, 2012),

$$\boldsymbol{M}(\boldsymbol{x}) = \lim_{\delta V_{\boldsymbol{x}} \to \delta V_{\boldsymbol{x}}^*} \frac{1}{\delta V_{\boldsymbol{x}}} \int_{\delta V_{\boldsymbol{x}}} \sum_{i=1}^{N} \boldsymbol{m}_i \delta(\boldsymbol{y} - \boldsymbol{x}_i)\, \mathrm{d}\boldsymbol{y}, \tag{2.150}$$

where the dummy integration vector $\boldsymbol{y}$ sweeps across the sensitive volume, $\boldsymbol{m}_i$ is the dipole moment of the i-th particle and $\boldsymbol{x}_i$ its position, as illustrated by Fig. (11). The

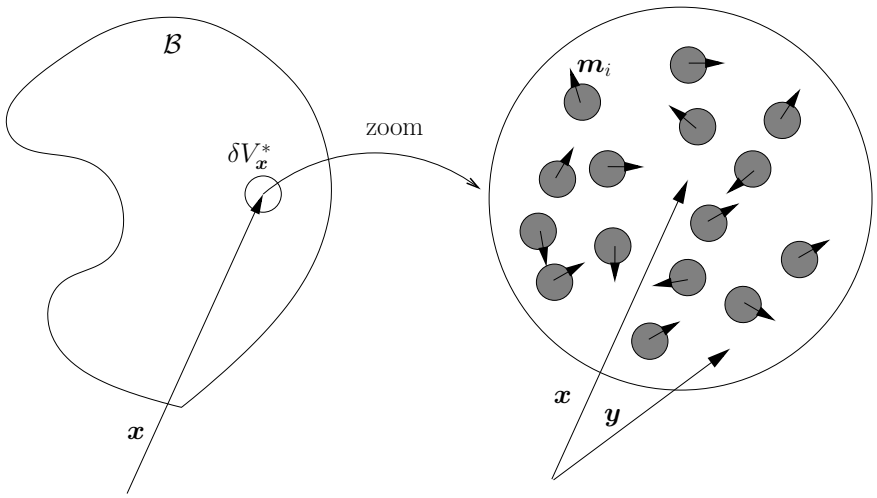

Figure 11 – Continuum mechanical interpretation of the magnetization as the volume average of magnetic dipoles in a sufficiently small volume $\delta V_{\boldsymbol{x}}^*$ (CUNHA, 2012).

volume average can be cast in a more transparent form by commuting the sum with the integral and integrating,

$$\boldsymbol{M}(\boldsymbol{x}) = \lim_{\delta V_{\boldsymbol{x}} \to \delta V_{\boldsymbol{x}}^*} \frac{n}{N} \sum_{i=1}^{N} \boldsymbol{m}_i. \tag{2.151}$$

where $n = N/\delta V_{\boldsymbol{x}}$. That is, the magnetization is the ensemble average of the dipole moment of the particles times their number density. This is an important formula since we use it in later sections to numerically determine the magnetization of our magnetic suspension. In the case of monodisperse particle magnetization, all the magnetic dipole moments have the same norm, so they are given by $\boldsymbol{m}_i = m\,\hat{\boldsymbol{m}}_i$, such that

$$\boldsymbol{M}(\boldsymbol{x}) = \lim_{\delta V_{\boldsymbol{x}} \to \delta V_{\boldsymbol{x}}^*} \frac{nm}{N} \sum_{i=1}^{N} \hat{\boldsymbol{m}}_i. \tag{2.152}$$

There, the magnetization is simply interpreted as the product of a saturation magnetization $M_s = nm$ and the average orientation of the particles, $\sum_{i=1}^{N} \hat{\boldsymbol{m}}_i/N$. That is, the highest achievable value of the magnetization is $M_s = nm$ when all particles are aligned in the same direction. This reasoning also provides a simple interpretation to the Langevin function (see Appendix A). In superparamagnetic materials, the magnetization is $\boldsymbol{M} = M_s \mathcal{L}(\alpha)\hat{\boldsymbol{H}}$, which comparing to Eq. (2.152) gives $\mathcal{L}(\alpha) = \hat{\boldsymbol{H}} \cdot \sum_{i=1}^{N} \hat{\boldsymbol{m}}_i/N$, i.e., the Langevin function is the average particle orientation projected onto the applied magnetic field direction.

Diamagnetic materials are composed of particles with no net magnetic moment, which develop orbital currents opposing external fields, hence presenting negative magnetization (i.e., magnetization in the opposite direction to the external field). However, diamagnetic effects are very mild compared to the other forms of magnetism, seldom being accounted for (JACKSON, 2012). In contrast, paramagnetic materials contain unpaired electrons whose dipole moments orient with an applied field, resulting in a net positive magnetization aligned with the field. In turn, ferromagnetic materials are made of paramagnetic particles which align along the direction of a very strong applied field. However, when the field is removed, the particles retain remnant magnetizations over sufficiently short distance ranges, determining so-called Weiss' domains, where the dipolar interaction tendency of alignment is stronger than exchange interactions (CHIKAZUMI; GRAHAM, 2009). This behavior persists for temperatures below Curie's point (1040 K for iron), where Brownian thermal fluctuation completely disorient the magnetic moments and the magnetization fizzles out. Fig. (12) illustrates Weiss' magnetic domains, each of which presents different magnetizations. Note that magnetic domains may be temporarily

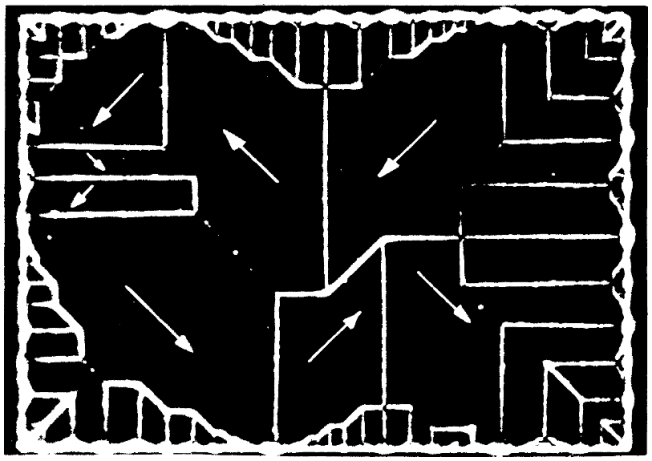

Figure 12 – Ferromagnetic domains (GRIFFITHS, 2005).

enlarged by the application of strong fields, henceforth producing magnets. In our analysis of magnetic suspensions in sedimentation, we consider the particles to be ferromagnetic magnets, permanently magnetized with a uniform magnetization.

There are many others responses to external fields, e.g. ferrimagnetism, antiferromagnetism, among others (MATTIS, 2006). The ones listed in this section are exemplary and by no means an attempt to fully cover the subject.

2.3.3 Formal Solution of Poisson's Equation

We derive the formal solution to Eq. (2.147). As desired, this provides the means to determine the magnetic field produced by a magnet, given that the magnetization distribution is known. First we write the divergence of the magnetization as a convolution

integral with the Dirac delta distribution,

$$\nabla^2\varphi = \int_{\mathbb{R}^3} \nabla_{\boldsymbol{x}'} \cdot \boldsymbol{M}(\boldsymbol{x}')\delta(\boldsymbol{x}-\boldsymbol{x}')\,\mathrm{d}\boldsymbol{x}'. \tag{2.153}$$

Then, we integrate by parts and, assuming that $\boldsymbol{M}(\boldsymbol{x})$ has compact support, the surface term vanishes and the remaining integral is carried over its support V, yielding

$$\nabla^2\varphi = -\int_V \boldsymbol{M}(\boldsymbol{x}') \cdot \nabla_{\boldsymbol{x}'}\delta(\boldsymbol{x}-\boldsymbol{x}')\,\mathrm{d}\boldsymbol{x}'. \tag{2.154}$$

Now we use the fundamental solution of Poisson's equation,

$$\nabla^2\left(-\frac{1}{4\pi|\boldsymbol{x}-\boldsymbol{x}'|}\right) = \delta(\boldsymbol{x}-\boldsymbol{x}'), \tag{2.155}$$

to replace the delta distribution in Eq. (2.154). The Laplacian commutes with the integral over $\boldsymbol{x}'$, hence by the uniqueness of solutions of Laplace's equation, we have

$$\varphi(\boldsymbol{x}) = \frac{1}{4\pi}\int_V \boldsymbol{M}(\boldsymbol{x}') \cdot \nabla_{\boldsymbol{x}'}\left(\frac{1}{|\boldsymbol{x}-\boldsymbol{x}'|}\right)\mathrm{d}\boldsymbol{x}'. \tag{2.156}$$

2.3.4 Magnetic Fields of a Sphere and a Prism

We exemplify the usage of Eq. (2.156) by applying it to our two cases of interest, namely the magnetic field produced by two uniformly magnetized permanent magnets: a sphere and a rectangular prism. The first is a model of the magnetic particles immersed in the suspension, whereas the latter is used as a magnet to generate an external field. In both cases, the uniform magnetization can be moved within the gradient and, by the divergence theorem, Eq. (2.156) can be recast in the form

$$\varphi(\boldsymbol{x}) = \frac{1}{4\pi}\int_S \frac{\boldsymbol{M}(\boldsymbol{x}') \cdot \hat{\boldsymbol{n}}(\boldsymbol{x}')}{|\boldsymbol{x}-\boldsymbol{x}'|}\,\mathrm{d}S'. \tag{2.157}$$

In the case of a sphere, illustrated in Fig. (13), we may assume the vectors $\boldsymbol{x}$ and $\boldsymbol{x}'$ to be coplanar due to azimuthal symmetry. Furthermore, we can choose the z-axis along the magnetization direction. In order to carry out the integral in Eq. (2.157), may write the Green kernel in terms of Legendre polynomials,

$$\frac{1}{|\boldsymbol{x}-\boldsymbol{x}'|} = \sum_{l=0}^{\infty}\left(\frac{a^l}{r^{l+1}}\right)P_l(\cos(\theta-\theta')). \tag{2.158}$$

The resulting integral is more readily calculated in terms of spherical harmonics, so we use the addition formula of Legendre polynomials (JACKSON, 2012; NIKIFOROV; UVAROV, 1988),

$$P_l(\cos(\theta-\theta')) = \frac{4\pi}{2l+1}\sum_{n=-l}^{l} Y^*_{ln}(\theta',\phi')Y_{ln}(\theta,\phi), \tag{2.159}$$

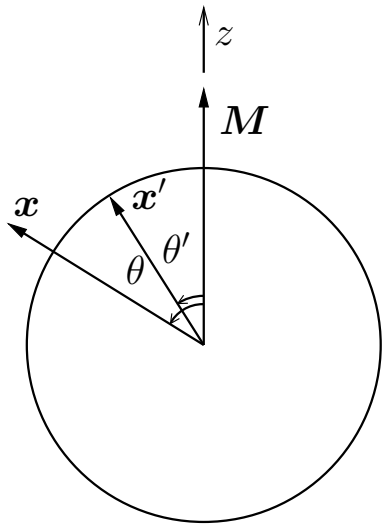

Figure 13 – Cross section of the magnetized sphere.

where Y_{ln} are the spherical harmonics and the asterisk stands for complex conjugation, such that Eq. (2.157) takes the form

$$\varphi(\boldsymbol{x}) = M \int \sum_{l=0}^{\infty} \sum_{n=-l}^{l} \frac{1}{2l+1} \left(\frac{a^l}{r^{l+1}} \right) Y_{ln}^*(\theta', \phi') Y_{ln}(\theta, \phi) \cos\theta' a^2 \mathrm{d}\Omega, \tag{2.160}$$

Ω being the solid angle. Writing the cosine in terms of spherical harmonics and integrating, their orthogonality relations yield

$$\varphi(\boldsymbol{x}) = \frac{m}{4\pi r^2} \cos\theta, \tag{2.161}$$

where $r = |\boldsymbol{x}|$ and $m = 4\pi a^3 M/3$, or in vector form,

$$\varphi(\boldsymbol{x}) = -\frac{\boldsymbol{m}}{4\pi} \cdot \nabla \left(\frac{1}{r} \right) = \frac{\boldsymbol{m} \cdot \boldsymbol{r}}{4\pi r^3}. \tag{2.162}$$

It can be noted that the magnetic field produced is equal to that of a dipole, $\boldsymbol{M}(\boldsymbol{x}) = \boldsymbol{m}\delta(\boldsymbol{x})$, while all other contributions vanish. From Eq. (2.146),

$$\boldsymbol{H} = \frac{3(\boldsymbol{m} \cdot \hat{\boldsymbol{r}})\hat{\boldsymbol{r}} - \boldsymbol{m}}{4\pi r^3}. \tag{2.163}$$

The gradient of this field will be of importance later, so we calculate it here in advance:

$$\nabla \boldsymbol{H} = \frac{3}{4\pi r^4} [\boldsymbol{m}\hat{\boldsymbol{r}} + \hat{\boldsymbol{r}}\boldsymbol{m} + (\boldsymbol{m} \cdot \hat{\boldsymbol{r}})\boldsymbol{I} - 5(\boldsymbol{m} \cdot \hat{\boldsymbol{r}})\hat{\boldsymbol{r}}\hat{\boldsymbol{r}}]. \tag{2.164}$$

A rectangular prismatic shaped magnet is depicted by in Fig. (14). Instead of calculating its potential, we turn directly to its magnetic field. Eqs. (2.146) and (2.157) furnish

$$\boldsymbol{H}(\boldsymbol{x}) = \frac{1}{4\pi} \int_S \frac{\boldsymbol{M}(\boldsymbol{x}') \cdot \hat{\boldsymbol{n}}(\boldsymbol{x}')(\boldsymbol{x} - \boldsymbol{x}')}{|\boldsymbol{x} - \boldsymbol{x}'|^3} \, \mathrm{d}S'. \tag{2.165}$$

Assuming that the magnetization is aligned in the positive direction of the z axis, only the top and bottom surfaces contribute to the integral, with opposite signs, resulting in

$$\boldsymbol{H}(\boldsymbol{x}) = \frac{M}{4\pi} \left\{ \int_{-\ell_y}^{\ell_y} \int_{-\ell_x}^{\ell_x} \frac{(x-x')\hat{\boldsymbol{e}}_1 + (y-y')\hat{\boldsymbol{e}}_2 + (z-z')\hat{\boldsymbol{e}}_3}{[(x-x')^2 + (y-y')^2 + (z-z')^2]^{3/2}} \, \mathrm{d}x' \, \mathrm{d}y' \right\} \Bigg|_{z'=-\ell_z}^{\ell_z}. \tag{2.166}$$

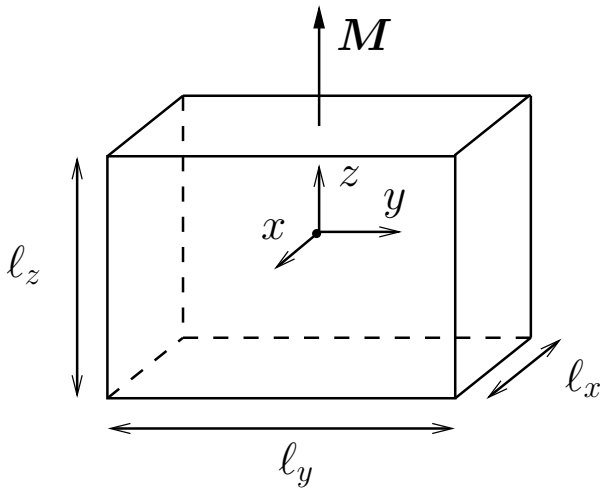

Figure 14 – Magnetized right rectangular prism.

Evaluation of the double integral with $d(\boldsymbol{x},\boldsymbol{x}') = \sqrt{(x-x')^2+(y-y')^2+(z-z')^2}$ provides

$$H_x = \frac{M}{4\pi}\left\{\frac{1}{2}\ln[(x-x')^2+(z-z')^2] - \ln[d(\boldsymbol{x},\boldsymbol{x}')+y-y']\right\}\Bigg|_{x'=-\ell_x}^{\ell_x}\Bigg|_{y'=-\ell_y}^{\ell_y}\Bigg|_{z'=-\ell_z}^{\ell_z}, \tag{2.167}$$

$$H_y = \frac{M}{4\pi}\left\{\frac{1}{2}\ln[(y-y')^2+(z-z')^2] - \ln[d(\boldsymbol{x},\boldsymbol{x}')+x-x']\right\}\Bigg|_{x'=-\ell_x}^{\ell_x}\Bigg|_{y'=-\ell_y}^{\ell_y}\Bigg|_{z'=-\ell_z}^{\ell_z}, \tag{2.168}$$

and

$$H_z = \tan^{-1}\left[\frac{(x-x')(y-y')}{(z-z')d(\boldsymbol{x},\boldsymbol{x}')}\right]\Bigg|_{x'=-\ell_x}^{\ell_x}\Bigg|_{y'=-\ell_y}^{\ell_y}\Bigg|_{z'=-\ell_z}^{\ell_z} \tag{2.169}$$

and the components of the magnetic field gradient are given by their derivatives,

$$\frac{\partial H_x}{\partial x} = \frac{M}{4\pi}\left\{\frac{x-x'}{(x-x')^2+(z-z')^2} - \frac{(x-x')}{d(\boldsymbol{x},\boldsymbol{x}')[d(\boldsymbol{x},\boldsymbol{x}')+y-y']}\right\}\Bigg|_{x'=-\ell_x}^{\ell_x}\Bigg|_{y'=-\ell_y}^{\ell_y}\Bigg|_{z'=-\ell_z}^{\ell_z}, \tag{2.170}$$

$$\frac{\partial H_x}{\partial y} = \frac{M}{4\pi}\left\{\frac{-1}{d(\boldsymbol{x},\boldsymbol{x}')+y-y'}\left[\frac{y-y'}{d(\boldsymbol{x},\boldsymbol{x}')}+1\right]\right\}\Bigg|_{x'=-\ell_x}^{\ell_x}\Bigg|_{y'=-\ell_y}^{\ell_y}\Bigg|_{z'=-\ell_z}^{\ell_z}, \tag{2.171}$$

$$\frac{\partial H_x}{\partial z} = \frac{M}{4\pi}\left\{\frac{z-z'}{(x-x')^2+(z-z')^2} - \frac{(z-z')}{d(\boldsymbol{x},\boldsymbol{x}')}\frac{1}{d(\boldsymbol{x},\boldsymbol{x}')+y-y'}\right\}\Bigg|_{x'=-\ell_x}^{\ell_x}\Bigg|_{y'=-\ell_y}^{\ell_y}\Bigg|_{z'=-\ell_z}^{\ell_z}, \tag{2.172}$$

$$\frac{\partial H_y}{\partial x} = \frac{M}{4\pi}\left\{\frac{-1}{d(\boldsymbol{x},\boldsymbol{x}')+x-x'}\left[\frac{x-x'}{d(\boldsymbol{x},\boldsymbol{x}')}+1\right]\right\}\Bigg|_{x'=-\ell_x}^{\ell_x}\Bigg|_{y'=-\ell_y}^{\ell_y}\Bigg|_{z'=-\ell_z}^{\ell_z}, \tag{2.173}$$

$$\frac{\partial H_y}{\partial y} = \frac{M}{4\pi}\left\{\frac{y-y'}{(y-y')^2+(z-z')^2} - \frac{(x-x')}{d(\boldsymbol{x},\boldsymbol{x}')}\frac{1}{d(\boldsymbol{x},\boldsymbol{x}')+x-x'}\right\}\Bigg|_{x'=-\ell_x}^{\ell_x}\Bigg|_{y'=-\ell_y}^{\ell_y}\Bigg|_{z'=-\ell_z}^{\ell_z}, \tag{2.174}$$

$$\frac{\partial H_y}{\partial z} = \frac{M}{4\pi}\left\{\frac{z-z'}{(y-y')^2+(z-z')^2} - \frac{(z-z')}{d(\boldsymbol{x},\boldsymbol{x}')}\frac{1}{d(\boldsymbol{x},\boldsymbol{x}')+x-x'}\right\}\Bigg|_{x'=-\ell_x}^{\ell_x}\Bigg|_{y'=-\ell_y}^{\ell_y}\Bigg|_{z'=-\ell_z}^{\ell_z}, \tag{2.175}$$

$$\begin{aligned}\frac{\partial H_z}{\partial x} = \frac{M}{4\pi}\Bigg\{&\frac{(y-y')(z-z')}{(z-z')^2 d^2(\boldsymbol{x},\boldsymbol{x}')] + (x-x')^2(y-y')^2} \\ &\times\left[d(\boldsymbol{x},\boldsymbol{x}') - \frac{(x-x')^2}{d(\boldsymbol{x},\boldsymbol{x}')}\right]\Bigg\}\Bigg|_{x'=-\ell_x}^{\ell_x}\Bigg|_{y'=-\ell_y}^{\ell_y}\Bigg|_{z'=-\ell_z}^{\ell_z},\end{aligned} \tag{2.176}$$

$$\begin{aligned}\frac{\partial H_z}{\partial y} = \frac{M}{4\pi}\Bigg\{&\frac{(x-x')(z-z')}{(z-z')^2 d^2(\boldsymbol{x},\boldsymbol{x}')] + (x-x')^2(y-y')^2} \\ &\times\left[d(\boldsymbol{x},\boldsymbol{x}') - \frac{(y-y')^2}{d(\boldsymbol{x},\boldsymbol{x}')}\right]\Bigg\}\Bigg|_{x'=-\ell_x}^{\ell_x}\Bigg|_{y'=-\ell_y}^{\ell_y}\Bigg|_{z'=-\ell_z}^{\ell_z}\end{aligned} \tag{2.177}$$

and

$$\begin{aligned}\frac{\partial H_z}{\partial z} = \frac{M}{4\pi}\Bigg\{&\frac{-(x-x')(y-y')}{(z-z')^2 d^2(\boldsymbol{x},\boldsymbol{x}')] + (x-x')^2(y-y')^2} \\ &\times\left[d(\boldsymbol{x},\boldsymbol{x}') - \frac{(z-z')^2}{d(\boldsymbol{x},\boldsymbol{x}')}\right]\Bigg\}\Bigg|_{x'=-\ell_x}^{\ell_x}\Bigg|_{y'=-\ell_y}^{\ell_y}\Bigg|_{z'=-\ell_z}^{\ell_z}.\end{aligned} \tag{2.178}$$

2.3.5 Magnetic Force and Torque on a Magnetic Dipole

Now we are able to determine the force and torque exerted by one magnetic dipole over another. First, we must seek the formulae that relate those quantities to magnetic fields. To this end, notice that when Ampère's law - Eq. (2.143) - is written in terms of $\boldsymbol{B}$ and $\boldsymbol{E}$ with the aid of Eqs. (2.138) and (2.139), the curl of $\boldsymbol{M}$ has the same form as a forcing as the current density. In fact, we have

$$\nabla\times\boldsymbol{B} - \mu_0\varepsilon_0\frac{\partial\boldsymbol{E}}{\partial t} = \mu_0\left(\boldsymbol{J}_f + \nabla\times\boldsymbol{M} + \frac{\partial\boldsymbol{P}}{\partial t}\right) \tag{2.179}$$

and we may define current densities

$$\boldsymbol{J}_{_M} = \nabla\times\boldsymbol{M} \tag{2.180}$$

and

$$\boldsymbol{J}_{_P} = \frac{\partial\boldsymbol{P}}{\partial t} \tag{2.181}$$

which are respectively due to circulation of magnetization and transient bound charge, whereas $\boldsymbol{J}_f$ results from the current of free charge, so that the sum of them acts as a total current density

$$\boldsymbol{J} = \boldsymbol{J}_f + \boldsymbol{J}_{M} + \boldsymbol{J}_{P}. \tag{2.182}$$

By Lorentz's force formula, we may write

$$\boldsymbol{F}_{M} = \int \boldsymbol{J} \times \boldsymbol{B}\, d\boldsymbol{x} \tag{2.183}$$

and for the torque around the center $\boldsymbol{x}_0$ of a particle,

$$\boldsymbol{T}_{M} = \int \boldsymbol{r} \times (\boldsymbol{J} \times \boldsymbol{B})\, d\boldsymbol{x}, \tag{2.184}$$

where $\boldsymbol{r} = \boldsymbol{x} - \boldsymbol{x}_0$. In the magnetostatic regime, we are left with

$$\boldsymbol{F}_{M} = \int \boldsymbol{J}_{M} \times \boldsymbol{B}\, d\boldsymbol{x} \tag{2.185}$$

and

$$\boldsymbol{T}_{M} = \int \boldsymbol{r} \times (\boldsymbol{J}_{M} \times \boldsymbol{B})\, d\boldsymbol{x}. \tag{2.186}$$

Let us derive a specific expression for the force over a magnetic dipole subject to an external magnetic induction $\boldsymbol{B}$, in the magnetostatic regime. From Eqs. (2.180), (2.141) with $\boldsymbol{M} = \boldsymbol{m}\delta(\boldsymbol{r})$,

$$\boldsymbol{J}_{M} \times \boldsymbol{B} = \nabla \cdot (\boldsymbol{B}\, \boldsymbol{m}\, \delta) - \nabla(\boldsymbol{m} \cdot \boldsymbol{B}\, \delta) + \nabla(\boldsymbol{m} \cdot \boldsymbol{B})\, \delta \tag{2.187}$$

eliding the arguments of the functions. Integrating (2.187) over free space and using the divergence's theorem for scalars and second-order tensors, the first two terms on the right-hand side yield null results since the singularity in the delta distribution is not contained in the boundary. Eq. (2.185), the constancy of $\boldsymbol{m}$ and the sampling property of the delta distribution give

$$\boldsymbol{F}_{M} = \boldsymbol{m} \cdot (\nabla \boldsymbol{B})^T|_{\boldsymbol{x}_0}. \tag{2.188}$$

Since the external field $\boldsymbol{B}$ does not account for the magnetization of the particle itself, we have

$$\boldsymbol{B} = \mu_0 \boldsymbol{H} \tag{2.189}$$

in that region[7]. Moreover, Eq. (2.145) implies

$$\nabla \boldsymbol{H} = (\nabla \boldsymbol{H})^T, \tag{2.190}$$

whereby Kelvin's force results,

$$\boldsymbol{F}_{M} = \mu_0 \boldsymbol{m} \cdot \nabla \boldsymbol{H}. \tag{2.191}$$

[7] The same argument can be extended to a discrete distribution of particles, where each particle has a neighborhood containing only that particle, resulting in no magnetization contribution to the external magnetic induction that acts over it.

Here, the evaluation of the gradient on the location of a particle is tacitly indicated, as the calculation aimed to determine the force *on a particle* all along.

The torque on a magnetic dipole is similarly calculated. To this end, a particular expression for the integrand of Eq. (2.186) is determined with the aid of vector operation identities as

$$\boldsymbol{r} \times (\boldsymbol{J}_{M} \times \boldsymbol{B}) = \nabla\delta \cdot (\boldsymbol{r} \times \boldsymbol{m})\, \boldsymbol{B} + \nabla\delta \times (\boldsymbol{r} \cdot \boldsymbol{B})\, \boldsymbol{m}. \tag{2.192}$$

Eq. (2.192) is integrated over free space analogously to the determination of Kelvin force: the product rule is used to obtain integrals of derivatives, which are then converted to surface integrals not containing the singularity of the delta function, thus being nullified. The remaining integrals contain delta distributions and yield the remainder of their integrands evaluated at the singularity, as follows:

$$\boldsymbol{T}_{M} = \nabla \cdot (\boldsymbol{m} \times \boldsymbol{r}\, \boldsymbol{B})|_{\boldsymbol{r}=\boldsymbol{0}} - \nabla \times (\boldsymbol{r} \cdot \boldsymbol{B}\, \boldsymbol{m})|_{\boldsymbol{r}=\boldsymbol{0}}. \tag{2.193}$$

Expanding the resulting terms and evaluating them at the singularity, bearing in mind that the external magnetic induction does not contain a magnetization contribution, there results from Eq. (2.184) that

$$\boldsymbol{T}_{M} = \mu_0 \boldsymbol{m} \times \boldsymbol{H}, \tag{2.194}$$

once more omitting that quantities must be evaluated at a magnetic dipole.

Now, considering the magnetic induction produced by one magnetic dipole, identified by the index j, as the incident field over another, tagged by the index i, the application of Eqs. (2.191) and (2.194) to the magnetic field of Eqs. (2.163) and (2.164) yields

$$\boldsymbol{F}_i = \frac{3\mu_0 m_i m_j}{4\pi r_{ji}^4}[(\hat{\boldsymbol{m}}_i \cdot \hat{\boldsymbol{m}}_j)\hat{\boldsymbol{r}}_{ji} + (\hat{\boldsymbol{m}}_i \cdot \hat{\boldsymbol{r}}_{ji})\hat{\boldsymbol{m}}_j + (\hat{\boldsymbol{m}}_j \cdot \hat{\boldsymbol{r}}_{ji})\hat{\boldsymbol{m}}_i - 5(\hat{\boldsymbol{m}}_i \cdot \hat{\boldsymbol{r}}_{ji})(\hat{\boldsymbol{m}}_j \cdot \hat{\boldsymbol{r}}_{ji})\hat{\boldsymbol{r}}_{ji}]. \tag{2.195}$$

and

$$\boldsymbol{T}_i = \frac{3\mu_0 m_i m_j}{4\pi r_{ji}^3}\left[(\hat{\boldsymbol{m}}_j \cdot \hat{\boldsymbol{r}}_{ji})\hat{\boldsymbol{m}}_i \times \hat{\boldsymbol{r}}_{ji} - \frac{1}{3}\hat{\boldsymbol{m}}_i \times \hat{\boldsymbol{m}}_j\right], \tag{2.196}$$

These force and torque formulae will be used in the dynamical simulations to investigate the behavior of magnetic suspensions.

3 Motion of an Isolated Particle

Our numerical study begins with the sedimentation of a spherical Brownian particle in a fluid without inertia. This is the case of small particles, with diameters of the order of micrometers. On that scale, viscous forces over the particle dominate inertial ones and since the particle itself is small, its trajectory is highly susceptible to the multiple collisions it suffers from the molecules of the carrier fluid, therefore it wanders erratically.

This regime is of interest in many practical applications of suspensions comprised of micrometer sized particles. In this setting, a first step towards the simulation of a suspension is a proper description of the dynamics of an isolated particle. Thus, our interest here is to determine the motion of an isolated particle and therefrom obtain macroscopic properties related to its motion. This approach is then readily extended to account for multiple particles and their interactions, providing a means for the calculation of transport properties in suspensions.

A key feature of this method is its non-dimensional formulation, which permits the identification of the influence of physical mechanisms over the macroscopic properties and the particle dynamics. We remark that the study of an isolated particle is also valuable because an analytic solution is available, so we present and compare it against the code which we developed, in order to validate it.

3.1 Formal Solution

In this section we present a solution to the equation of motion of the spherical isolated Brownian particle equivalent to that of Uhlenbeck and Ornstein (1930) but specialized to our problem by restricting attention to the case of a constant gravitational force field. We begin by stating this equation of motion, which is derived from Newton's second law applied to the particle,

$$\mathcal{M}\frac{d\boldsymbol{U}}{dt} = -6\pi\eta a\boldsymbol{U} + \boldsymbol{F}^b(t) + \mathcal{M}\boldsymbol{g}, \tag{3.1}$$

where $\boldsymbol{F}^b(t)$ is the Brownian force and all the other symbols have already been defined as in Chap. (2). The force interaction between particle and fluid is split into two contributions, a systematic drag $-6\pi\eta a\boldsymbol{U}$ and a random fluctuating force $\boldsymbol{F}^b$. Their balance keeps the particle in perpetual motion.

In this work, we take the Langevin dynamics approach of describing the motion in a timescale much longer than the correlation time of forces of the collisions which the carrier fluid particles impart on the mesoparticle. Under this description, we avoid the cumbersome details of these countless collisions and instead provide their statistical moments. Even if in doing so we lose the possibility of reporting the exact trajectory of the particle, our actual interest resides on the properties the system presents and those depend rather on the statistical properties of the motion.

With this characterization of the Brownian force, Eq. (3.1) is a stochastic ODE, where each realization of the particle trajectory provides different velocities. Under this condition, the quantities of interest must be characterized by ensemble averages, represented by

$$\langle G \rangle = \lim_{n_r \to \infty} \frac{1}{n_r} \sum_{i=1}^{n_r} G_i. \tag{3.2}$$

Here the general quantity $G = G(\alpha_i, t)$ is a stochastic process from a statistic point of view and n_r is the total number of realizations. In a constant time, G is a random variable of the process, depending on the realizations α_i.

The preceding discussion motivates us to assume that the Brownian force has no preferred direction, such that its average is null,

$$\langle \boldsymbol{F}^b(t) \rangle = \boldsymbol{0}, \tag{3.3}$$

and that it is uncorrelated at the timescale in which we describe it, i.e.,

$$\langle \boldsymbol{F}^b(t) \boldsymbol{F}^b(t+\tau) \rangle = 12 k_{_B} T \pi \eta a \delta(\tau)\, \boldsymbol{I} \tag{3.4}$$

where $k_{_B}$ is the Boltzmann constant, T the temperature, $\delta(\tau)$ Dirac's delta distribution and $\boldsymbol{I}$ the identity second-rank tensor. The intensity of this autocorrelation at equal times follows from the fluctuation-dissipation theorem (ZWANZIG, 2001).

Before presenting the solution of Eq. (3.1), we write it in non-dimensional form. To this end, we define the following characteristic scales:

$$|\boldsymbol{U}| \sim U_s, \quad t \sim \frac{a}{U_s}, \quad |\boldsymbol{F}^b| \sim \left(\frac{2 D_0 U_s}{a} \right)^{1/2} 6\pi\eta a. \tag{3.5}$$

The Brownian force scale comes from the square root of the coefficient in Eq. (3.4), with the Stokes-Einstein diffusivity defined by

$$D_0 = \frac{k_{_B} T}{6\pi\eta a}, \tag{3.6}$$

bearing in mind that $\delta(\tau)$ has the dimensions of $[t]^{-1}$. The non-dimensional parameters which result from this process are the Stokes number,

$$St = \frac{\mathcal{M} U_s}{6\pi\eta a}, \tag{3.7}$$

which measures the ratio between the inertia of the particle and the hydrodynamic drag exerted by the fluid, and the Péclet number,

$$Pe = \frac{aU_s}{D_0}, \tag{3.8}$$

a measure of the hydrodynamic drag over the thermal Brownian forces imposed over the particle. Denoting non-dimensional variables by tildes and noting that $\mathcal{M}g = 6\pi\eta a U_s$, we have

$$St\frac{d\tilde{\boldsymbol{U}}}{d\tilde{t}} + \tilde{\boldsymbol{U}} = \sqrt{\frac{2}{Pe}}\,\tilde{\boldsymbol{F}}^b(\tilde{t}) - \hat{\boldsymbol{e}}_3, \tag{3.9}$$

where $\hat{\boldsymbol{e}}_3$ is the versor which points in the direction opposite to gravity. Eq. (3.9) is a linear first-order ODE, thus it has the straightforward solution

$$\tilde{\boldsymbol{U}}(\tilde{t}) = \tilde{\boldsymbol{U}}(0)e^{-\tilde{t}/St} + \sqrt{\frac{2}{PeSt^2}}\int_0^{\tilde{t}} \tilde{\boldsymbol{F}}^b(\tilde{t}')e^{-(\tilde{t}-\tilde{t}')/St}\,d\tilde{t}' - \hat{\boldsymbol{e}}_3(1-e^{-\tilde{t}/St}), \tag{3.10}$$

by the integrating factor method.

We can also calculate the particle displacement by integrating Eq. (3.10),

$$\tilde{\boldsymbol{x}}(\tilde{t}) - \tilde{\boldsymbol{x}}(0) = \tilde{\boldsymbol{U}}(0)\int_0^{\tilde{t}} e^{-\tilde{t}''/St}\,d\tilde{t}'' + \sqrt{\frac{2}{PeSt^2}}\int_0^{\tilde{t}}\int_0^{\tilde{t}''} \tilde{\boldsymbol{F}}^b(\tilde{t}')e^{-(\tilde{t}''-\tilde{t}')/St}\,d\tilde{t}'\,d\tilde{t}'' - \hat{\boldsymbol{e}}_3\int_0^{\tilde{t}}(1-e^{-\tilde{t}''/St})\,d\tilde{t}''. \tag{3.11}$$

Changing the order of integration in the double integral,

$$\int_0^{\tilde{t}}\int_0^{\tilde{t}''} \tilde{\boldsymbol{F}}^b(\tilde{t}')e^{-(\tilde{t}''-\tilde{t}')/St}\,d\tilde{t}'\,d\tilde{t}'' = \int_0^{\tilde{t}}\int_{\tilde{t}'}^{\tilde{t}} \tilde{\boldsymbol{F}}^b(\tilde{t}')e^{-(\tilde{t}''-\tilde{t}')/St}\,d\tilde{t}''\,d\tilde{t}' \tag{3.12}$$

which can now be directly integrated, yielding

$$\int_0^{\tilde{t}}\int_0^{\tilde{t}''} \tilde{\boldsymbol{F}}^b(\tilde{t}')e^{-(\tilde{t}''-\tilde{t}')/St}\,d\tilde{t}'\,d\tilde{t}'' = St\int_0^{\tilde{t}} \tilde{\boldsymbol{F}}^b(\tilde{t}')\left[1-e^{-(\tilde{t}-\tilde{t}')/St}\right]d\tilde{t}'. \tag{3.13}$$

Consequently, denoting the displacement by $\Delta\tilde{\boldsymbol{x}}(\tilde{t}) = \tilde{\boldsymbol{x}}(\tilde{t}) - \tilde{\boldsymbol{x}}(0)$,

$$\Delta\tilde{\boldsymbol{x}}(\tilde{t}) = \tilde{\boldsymbol{U}}(0)St(1-e^{-\tilde{t}/St}) + \sqrt{\frac{2}{Pe}}\int_0^{\tilde{t}} \tilde{\boldsymbol{F}}^b(\tilde{t}')\left[1-e^{-(\tilde{t}-\tilde{t}')/St}\right]d\tilde{t}' - \hat{\boldsymbol{e}}_3\left[\tilde{t} - St(1-e^{-\tilde{t}/St})\right]. \tag{3.14}$$

The macroscopic properties of the process are related to the fluctuation of the stochastic variable $\tilde{\boldsymbol{U}}$, i.e., its deviation with respect to the mean, which we denote by a prime and calculate as $\tilde{\boldsymbol{U}}' = \tilde{\boldsymbol{U}} - \langle\tilde{\boldsymbol{U}}\rangle$. Taking the ensemble average of Eq. (3.10), which commutes with time integrals, and using Eq. (3.3),

$$\langle\tilde{\boldsymbol{U}}\rangle(\tilde{t}) = \tilde{\boldsymbol{U}}(0)e^{-\tilde{t}/St} - \hat{\boldsymbol{e}}_3(1-e^{-\tilde{t}/St}). \tag{3.15}$$

From Eqs. (3.10) and (3.15), it follows that

$$\tilde{\boldsymbol{U}}'(\tilde{t}) = \sqrt{\frac{2}{PeSt^2}}\int_0^{\tilde{t}} \tilde{\boldsymbol{F}}^b(\tilde{t}')e^{-(\tilde{t}-\tilde{t}')/St}\,d\tilde{t}'. \tag{3.16}$$

The important physical conclusion to be drawn from Eqs. (3.15) and (3.16) is that gravity only contributes to the mean motion of the particle, whereas the Brownian force contributes to the fluctuation of the particle velocity about the mean.

We are now in a position to calculate the properties of interest, namely the autocorrelation of velocity fluctuations, their variance, and the diffusivity. The first one is given by

$$\tilde{\boldsymbol{C}}(\tilde{\tau}) = \lim_{\tilde{t}\to\infty} \langle \tilde{\boldsymbol{U}}'(\tilde{t})\tilde{\boldsymbol{U}}'(\tilde{t}+\tilde{\tau})\rangle, \tag{3.17}$$

where the time limit assures that the stochastic process may be rendered statistically permanent, the effects of the initial conditions will already have decayed and the process will attain its thermodynamic limit. From Eq. (3.16),

$$\tilde{\boldsymbol{C}}(\tilde{\tau}) = \frac{2}{PeSt^2} \lim_{\tilde{t}\to\infty} \int_0^{\tilde{t}} \int_0^{\tilde{t}+\tilde{\tau}} \langle \tilde{\boldsymbol{F}}^b(\tilde{t}')\tilde{\boldsymbol{F}}^b(\tilde{t}'')\rangle e^{-(2\tilde{t}+\tilde{\tau}-\tilde{t}'-\tilde{t}'')/St}\, d\tilde{t}''\, d\tilde{t}'. \tag{3.18}$$

Eq. (3.4), which in non-dimensional form is $\langle \tilde{\boldsymbol{F}}^b(\tilde{t})\tilde{\boldsymbol{F}}^b(\tilde{t}+\tilde{\tau})\rangle = \tilde{\delta}(\tau)\,\boldsymbol{I}$, implies

$$\tilde{\boldsymbol{C}}(\tilde{\tau}) = \frac{2\boldsymbol{I}}{PeSt^2} \lim_{\tilde{t}\to\infty} \int_0^{\tilde{t}} \int_0^{\tilde{t}+\tilde{\tau}} \tilde{\delta}(\tilde{t}''-\tilde{t}') e^{-(2\tilde{t}+\tilde{\tau}-\tilde{t}'-\tilde{t}'')/St}\, d\tilde{t}''\, d\tilde{t}'. \tag{3.19}$$

By the sampling property of the delta distribution,

$$\tilde{\boldsymbol{C}}(\tilde{\tau}) = \frac{2\boldsymbol{I}}{PeSt^2} \lim_{\tilde{t}\to\infty} \int_0^{\tilde{t}} e^{-(2\tilde{t}-2\tilde{t}'+\tilde{\tau})/St}\, d\tilde{t}', \tag{3.20}$$

First integrating and then calculating the limit, we have

$$\tilde{\boldsymbol{C}}(\tilde{\tau}) = \frac{e^{-\tilde{\tau}/St}}{PeSt}\,\boldsymbol{I}. \tag{3.21}$$

Note that, by Eq. (3.21), the non-dimensional correlation time of the velocity fluctuations is the Stokes number. In dimensional form, this correlation time is the relaxation time of the particle, $\mathcal{M}/6\pi\eta a$. The variance of the velocity fluctuations, which is the autocorrelation for a null time shift, is equal to

$$\langle \tilde{\boldsymbol{U}}(t)\tilde{\boldsymbol{U}}(t)\rangle = \frac{\boldsymbol{I}}{PeSt}. \tag{3.22}$$

We perceive that when Pe or St is increased, the velocity fluctuations are hindered. Physically, this occurs when the intensity of Brownian forces diminishes or when the inertia of the particle increases, respectively, relative to the hydrodynamic drag. This second mechanism is worth remarking, since it is absent is the often studied case of particles with negligible inertia.

The diffusivity is given by the integral of the autocorrelation of velocity fluctuations,

$$\tilde{\boldsymbol{D}} = \int_0^{\infty} \tilde{\boldsymbol{C}}(\tilde{\tau})\, d\tilde{\tau}. \tag{3.23}$$

Integrating Eq. (3.21),

$$\tilde{\boldsymbol{D}} = \frac{\boldsymbol{I}}{Pe}. \tag{3.24}$$

The inertia of the particle does not affect the diffusivity because even though it hinders the variance of velocity fluctuations, it also enhances the correlation time, i.e., the memory of the system, and both contributions cancel out in the integral. It should be noted that, in dimensional form, we have $\boldsymbol{D} = D_0\,\boldsymbol{I}$, that is, isotropic diffusion with the Stokes-Einstein diffusion coefficient. In this case, gravity only affects the mean velocity, thus it does not alter the diffusivity, caused exclusively by Brownian velocity fluctuations.

That is not the case in a suspension, cf. (KOCH, 1994; LADD, 1993), where the hydrodynamic interaction between particles couples their motion, and gravity inserts memory in the system. Furthermore, in this scenario, hydrodynamic interaction induces dispersion and enhances the diffusivity. The code which we have developed aims to determine velocity fluctuations and diffusivity in suspensions, using the isolated particle as a validation, since its motion has the analytic solution presented.

As an addendum to this section, we calculate the ensemble average of the particle displacements, which provides the appropriate form of the argument of Einstein (1956) when gravity is present, similarly to the more general results of Uhlenbeck and Ornstein (1930). Note that in this case gravity does exert an effect over the displacement since the latter is not a fluctuation, but rather the integral of the velocity, including its mean value. Since we are only interested in the contribution which gravity exerts over the motion, it suffices to address the case where the initial velocity is null. Thus, Eqs. (3.3), (3.4) and (3.14) yield

$$\langle \Delta\tilde{\boldsymbol{x}}(\tilde{t})\Delta\tilde{\boldsymbol{x}}(\tilde{t})\rangle = \hat{\boldsymbol{e}}_3\hat{\boldsymbol{e}}_3[\tilde{t} - St(1-e^{-\tilde{t}/St})]^2 + \frac{2\boldsymbol{I}}{Pe}\left[\tilde{t} - \frac{St}{2}(3 - 4e^{-\tilde{t}/St} + e^{-2\tilde{t}/St})\right]. \quad (3.25)$$

In particular, when $St \to 0$, finite times are much greater the correlation time of velocity fluctuations, so thermodynamic equilibrium is attained and we have

$$\langle \Delta\tilde{\boldsymbol{x}}(\tilde{t})\Delta\tilde{\boldsymbol{x}}(\tilde{t})\rangle = \tilde{t}^2\hat{\boldsymbol{e}}_3\hat{\boldsymbol{e}}_3 + \frac{2\tilde{t}}{Pe}\boldsymbol{I}, \quad (3.26)$$

which in dimensional form is precisely Einstein's argument, $\langle \Delta\tilde{\boldsymbol{x}}\Delta\tilde{\boldsymbol{x}}\rangle = 2D_0 t\,\boldsymbol{I}$, plus a contribution due to gravity which is quadratic in time, related to sedimentation at the Stokes velocity.

3.2 Computational Procedure

Now we describe the Langevin dynamics computational algorithm which we have developed to determine macroscopic properties of the aforementioned problem, i.e., the motion of a spherical isolated particle in the presence of Brownian and gravitational forces at low particle Reynolds numbers and a nonzero Stokes number.

The non-dimensional stochastic differential equation that describes the particle dynamics is the same as Eq. (3.9), but with the approximation

$$\tilde{\boldsymbol{F}}^b(t) \approx \frac{\mathbf{n}^F(t)}{\Delta\tilde{t}}, \quad (3.27)$$

which enables the numerical implementation of the Brownian force. Here $\mathbf{n}^F(t)$ is a pseudo-random vector with Gaussian distribution, null average $\langle \mathbf{n}^F(t) \rangle = \mathbf{0}$ and unitary variance, $\langle \mathbf{n}^F(t)\mathbf{n}^F(t) \rangle = \boldsymbol{I}$ (NÄGELE, 2006). In addition, the term $1/\Delta\tilde{t}$ is an approximation of the Delta distribution by the impulse associated with the numerical time step $\Delta\tilde{t}$. Under these conditions, we have

$$St \frac{d\tilde{\boldsymbol{U}}}{d\tilde{t}} + \tilde{\boldsymbol{U}} = \sqrt{\frac{2}{Pe\,\Delta\tilde{t}}}\,\mathbf{n}^F(t) - \hat{\boldsymbol{e}}_3, \tag{3.28}$$

Eq. (3.28) is numerically integrated via a standard Euler method. We remind that Eq. (3.28) defines a stochastic process, thus the particle velocity as a function of time is different in each realization of it that we make. The quantities of interest are, as usual, calculated as averages over all the realizations we carry out, given by Eq. (3.2) but for a finite number of realizations.

A typical particle trajectory obtained in a numerical realization is exhibited in Fig. (15), along with the mean square displacement, both in the direction of gravity and orthogonal to it. The mean square displacement is calculated by

$$\langle \Delta\tilde{\boldsymbol{x}}(\tilde{t}) \Delta\tilde{\boldsymbol{x}}(\tilde{t}) \rangle = \frac{1}{n_r} \sum_{i=1}^{n_r} \Delta\tilde{\boldsymbol{x}}_i(\tilde{t}) \Delta\tilde{\boldsymbol{x}}_i(\tilde{t}), \tag{3.29}$$

where the index i refers to the value of the random variable obtained at the i-th realization. There are no restrictions on the initial time, according to the discussion leading to Eq. (3.26), since we simulated the case $St = 0$. The numerical results agree very well with Eq. (3.26) in both directions. Fig. (16) pictures the influence of the Péclet number over the motion of the particle. It can be seen that at small values of Pe, the hydrodynamic drag dominates the Brownian diffusion and the motion is more deterministic. On the other hand, for low Pe, these thermal Brownian effects dominate, the motion is more erratic and prominently diffusive.

Another property of the process which we calculate numerically is the variance of the velocity fluctuations, obtained from Eq. (3.2) as

$$\langle \tilde{\boldsymbol{U}}'(\tilde{t}) \tilde{\boldsymbol{U}}'(\tilde{t}) \rangle = \frac{1}{n_r} \sum_{i=1}^{n_r} \tilde{\boldsymbol{U}}'_i(\tilde{t}) \tilde{\boldsymbol{U}}'_i(\tilde{t}), \tag{3.30}$$

where $\tilde{t}$ is a time much larger than the correlation time of velocity fluctuations, in order for the process to be statistically steady. We take a particular interest in this property because it is the simplest measure of the intensity of the velocity fluctuations. Figure (17) shows the variance of velocity fluctuations to scale with St^{-1} in contrast with scaling analysis based on a purely inertial regime, which finds $St^{-2/3}$ (CUNHA, 1997). In any case, this result points out that particle inertia has a role in suppressing the velocity fluctuations. This is particularly important as a type of screening mechanism for the velocity fluctuations at low Reynolds suspensions, where the interplay between viscous hydrodynamic interactions and the inertia of the particles determines the order of velocity fluctuations. We argue that this finding could be fundamental for our understanding of

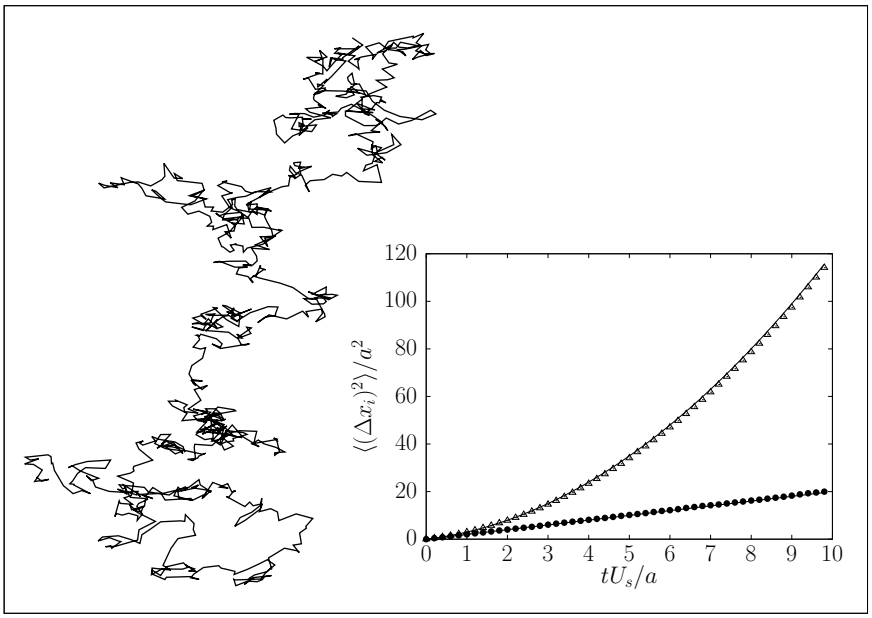

Figure 15 – Typical stochastic trajectory of an isolated sedimenting particle in Brownian motion. The insert shows the mean square displacement of the particle. The directions perpendicular and parallel to gravity are denoted by • and △, respectively. Eq. (3.26) for the square displacement is represented by a continuous line (—). Numerical simulation carried out for $St = 0$ and $Pe = 1$.

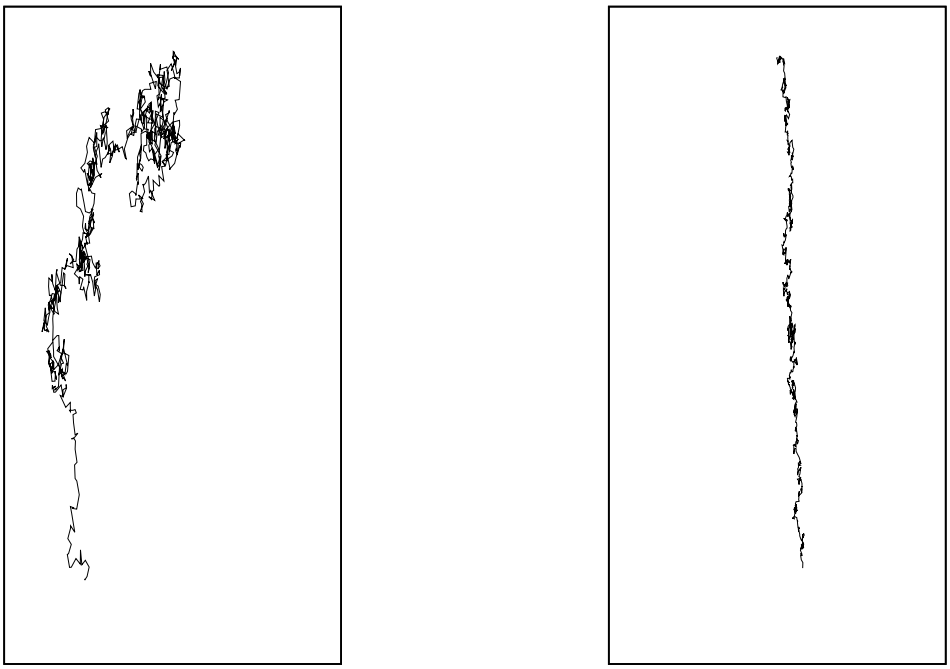

(a) $Pe = 1$. (b) $Pe = 10$.

Figure 16 – Typical stochastic trajectories as a function of the Péclet number.

the velocity fluctuations divergence in dilute sedimenting suspensions with particles free of inertia and distributed randomly and independently in a numerical box (i.e. divergence

paradox (CUNHA, 1997; HINCH, 1988)).

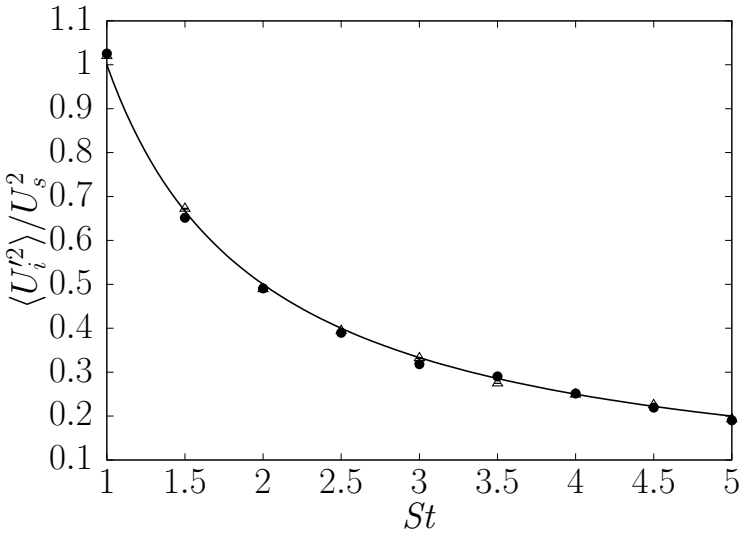

Figure 17 – Vertical component of the velocity fluctuation variance of a massive isolated particle as a function of St, to $Pe = 1$. The directions perpendicular and parallel to gravity are denoted by • and △, respectively.

The autocorrelation is calculated in the same way as the variance, but for velocity fluctuations relative to two different times: a sufficiently large $\tilde{t}$, and a posterior one, $\tilde{t}+\tilde{\tau}$, that is,

$$\langle \tilde{\boldsymbol{U}}'(\tilde{t})\tilde{\boldsymbol{U}}'(\tilde{t}+\tilde{\tau})\rangle = \frac{1}{n_r}\sum_{i=1}^{n_r} \tilde{\boldsymbol{U}}_i'(\tilde{t})\tilde{\boldsymbol{U}}_i'(\tilde{t}+\tilde{\tau}). \tag{3.31}$$

Here we present the autocorrelations are normalized by the variance, namely

$$c_{ij}(\tilde{\tau}) = \frac{\langle \tilde{U}_i'(\tilde{t})\tilde{U}_j'(\tilde{t}+\tilde{\tau})\rangle}{\langle \tilde{U}_i'(\tilde{t})\tilde{U}_j'(\tilde{t})\rangle}, \tag{3.32}$$

which is already non-dimensional by definition. The results of Eq. (3.31) are presented in Fig. (18). The autocorrelations calculated numerically agree very well with the analytic result. The role of inertia in the insertion of memory can be clearly seen. As St is increased, these autocorrelations take a much longer time to decay.

The diffusivity is calculated by the integral of the autocorrelation of velocity fluctuations, that is,

$$\tilde{\boldsymbol{D}} = \int_0^{\tilde{T}} \langle \tilde{\boldsymbol{U}}'(\tilde{t})\tilde{\boldsymbol{U}}'(\tilde{t}+\tilde{\tau})\rangle d\tilde{\tau}, \tag{3.33}$$

where $\tilde{t}$ and $\tilde{T}$ are times much larger than the correlation time of the velocity fluctuations, such that the autocorrelations integrated are already statistically steady and the integral converges, such that the particle diffusivity plateau is reached. Fig. (19) presents the diffusivity as a function of the Péclet number. The values obtained for the diagonal terms in both the directions orthogonal and parallel to gravity are in accordance with the Stokes-Einstein diffusion coefficient, given in non-dimensional form by Eq. (3.24), also indicating the isotropy of the Brownian diffusivity.

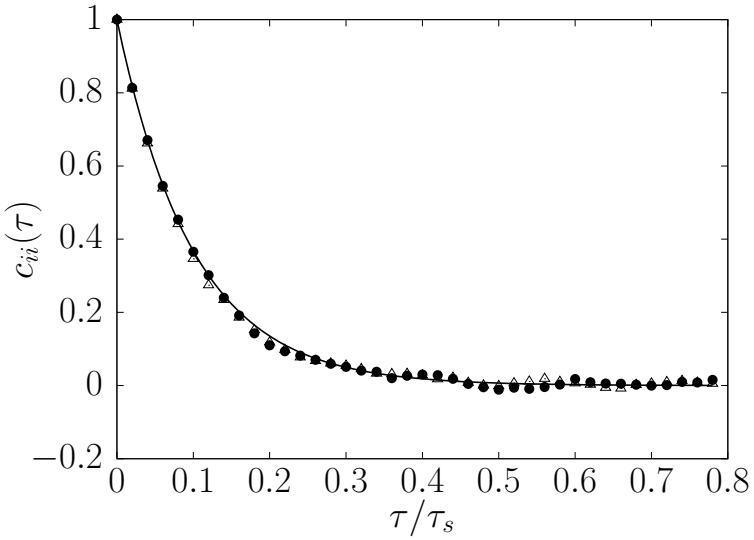

(a) $St = 0.1$.

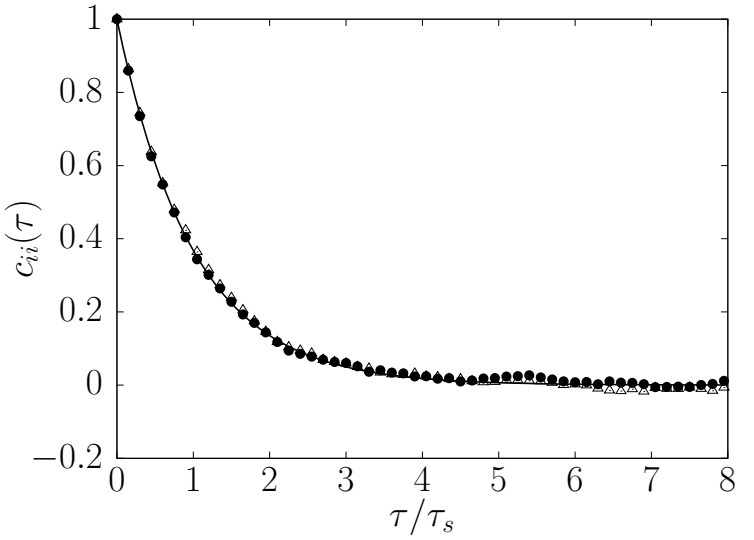

(b) $St = 1$.

Figure 18 – Normalized velocity fluctuations autocorrelation for different values of St and $Pe = 1$. The directions perpendicular and parallel to gravity are denoted by $\bullet$ and $\triangle$, respectively. Eq. (3.21) normalized, $c(\tilde{\tau}) = \exp(-\tilde{\tau}/St)$, is represented by solid lines (—).

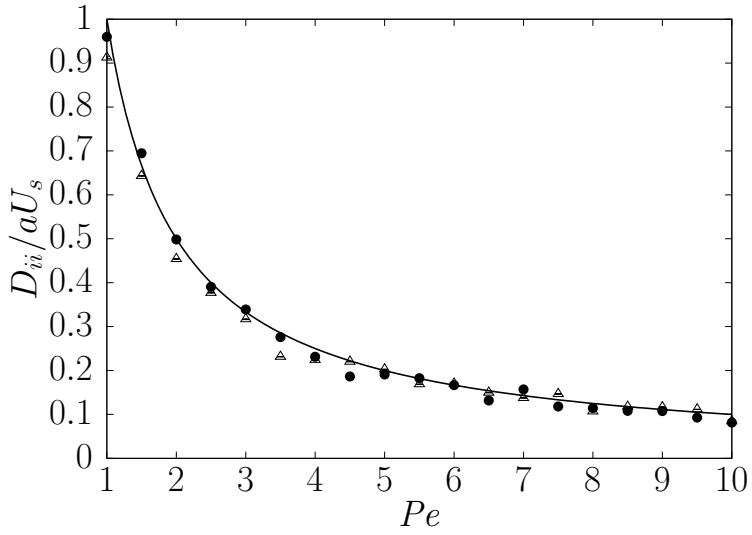

Figure 19 – Diagonal components of the diffusivity of a massive isolated particle as a function of Pe for $St = 1$. The directions perpendicular and parallel to gravity are denoted by $\bullet$ and $\triangle$, respectively.

4 Many-Body Simulations

In this chapter, we describe our Langevin dynamics simulation of magnetic suspensions. We developed a Fortran code to implement this model. We stress that the range of parameters explored is fitting for a gas-solid suspension, such as a magnetic dusty gas. However, this model is also suitable for simulations of liquid-solid suspensions, such as magnetorheological fluids, with a proper choice of the physical parameters. Typical simulations take about 2 days to be run.

4.1 Langevin Dynamics

In order to simulate a dilute suspension of spherical micron-sized particles in sedimentation at low Reynolds number, we extend Eq. (3.28) by accounting for the forces caused by hydrodynamic and magnetic dipolar interactions between particles, as well as an external magnetic field. In addition, we also consider short-range repulsion forces due to both a stabilizing steric layer of surfactants and Hertzian contact when the particles overlap. Thus, Newton's second laws for the translation and rotation of a particle i take the forms

$$\mathcal{M}_i \frac{d\boldsymbol{U}_i}{dt} = \boldsymbol{F}_i^h + \boldsymbol{F}_i^d + \boldsymbol{F}_i^m + \boldsymbol{F}_i^b + \boldsymbol{F}_i^r + \boldsymbol{F}_i^c + \boldsymbol{F}_i^g \tag{4.1}$$

and

$$J_i \frac{d\boldsymbol{\Omega}_i}{dt} = \boldsymbol{T}_i^h + \boldsymbol{T}_i^d + \boldsymbol{T}_i^m + \boldsymbol{T}_i^b, \tag{4.2}$$

where the indices h, d, m, b, r, c and g stand for hydrodynamic, magnetic dipolar, external magnetic, Brownian, repulsive, contact and gravitational forces or torques.

We also assume that the dipolar moments of the particles are fixed to them, thus they rotate with their angular velocities. This is a fair assumption for sufficiently large particles, which are not influenced by quantum-mechanical effects of intrinsic dipole rotation. Indeed, this hypothesis is applicable to our study, since the Néel relaxation time of micron-sized particles is far larger than their Brownian relaxation times (ODENBACH, 2009). Therefore,

$$\frac{d\hat{\boldsymbol{m}}_i}{dt} = \boldsymbol{\Omega}_i \times \hat{\boldsymbol{m}}_i. \tag{4.3}$$

The hydrodynamic forces and torques are given by the inversion of the mobility relation (2.113), with the mobility matrices (2.126) to (2.133). Other works, e.g. Nitsche

and Batchelor (1997), have shown that even point particle approximations provide a good qualitative picture of the hydrodynamic interaction in dilute suspensions. Therefore, our mobility matrices with first-order corrections due to particle size are suitable for this simulation. The magnetic dipolar forces and torques are given by the sums of Eqs. (2.195) and (2.196) over all other particles, assuming this superposition to be valid. Such an assumption is sensible in very dilute suspensions. It should be noted the magnetic dipole moments are extensive properties, proportional to the volume of the particles. This is an important effect in the analysis of polydisperse suspensions. The external magnetic force and torque follow from Eqs. (2.191) and (2.194), with a magnetic field of our choice. While the Brownian forces and torques are modeled in the same fashion as in Eq. (3.28), it should be borne in mind that their intensity varies with the radius of the particles, according to Eq. (3.4).

We account for mechanisms which prevent the overlap of particles over the course of the simulation. Instead of considering the detailed lubrication forces arising from hydrodynamic interactions at short range, which are computationally costly, we only consider short range repulsion due to surfactants or contact. Nevertheless, the effect produced is qualitatively the same, the superposition of particles is avoided. The surfactant layer repulsion force between two particles is given by the Rosensweig, Nestor and Timmins (1965) formula, reproduced in Rosensweig (2013),

$$\boldsymbol{F}_{ij}^{r} = \begin{cases} -\dfrac{\pi N_{sup} k_B T (a_i + a_j - 2\delta_s)^2}{2\delta_s} \ln\left(\dfrac{a_i + a_j}{r_{ij}}\right) \hat{\boldsymbol{r}}_{ij}, & -2\delta_s < \varepsilon_{ij} < 0, \\ \boldsymbol{0} \quad \text{otherwise.} \end{cases} \tag{4.4}$$

where N_{sup} is the surface density of surfactants, δ_s is the thickness of the surfactant layer and the gap between particles is defined by $\varepsilon_{ij} = r_{ij} - a_i - a_j$. The steric layer covering the particles is illustrated by Fig. (20). The Hertz force due to contact of two overlapping[1] spheres is (TIMOSHENKO; GOODIER, 1970; ABADE; CUNHA, 2007)

$$\boldsymbol{F}_{ij}^{c} = \begin{cases} -\kappa \left[\left(\dfrac{1}{a_i - \delta_s} + \dfrac{1}{a_j - \delta_s} \right)^{-1} \delta_{ij}^3 \right]^{1/2} \hat{\boldsymbol{r}}_{ij}, & \delta_{ij} > 0, \\ \boldsymbol{0} \quad \text{otherwise,} \end{cases} \tag{4.5}$$

where κ is a constant related to material properties of the particles and $\delta_{ij} = \varepsilon_{ij} - 2\delta_s$ is the virtual overlap of the magnetic cores i and j, cf. Fig. (21). The total repulsion and contact forces are respectively given by sums of Eqs. (4.4) and (4.5) over all other particles j.

We account for the possibility of different particle radii in our scaling by taking the average radius as the length scale of the problem. Therefore, the characteristic scales

[1] With overlapping magnetic cores.

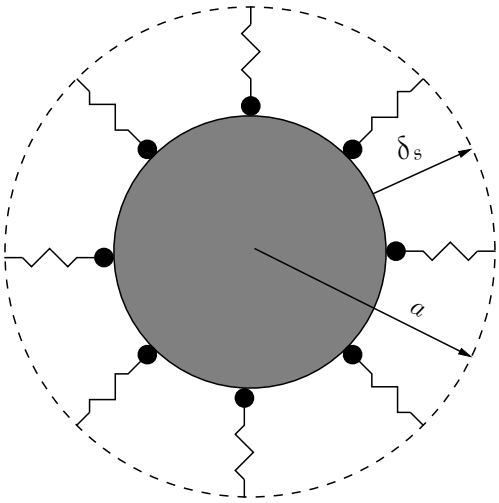

Figure 20 – Schematic depiction of the steric repulsion layer. Surfactants represented by spring with beads attached to the magnetic core surface.

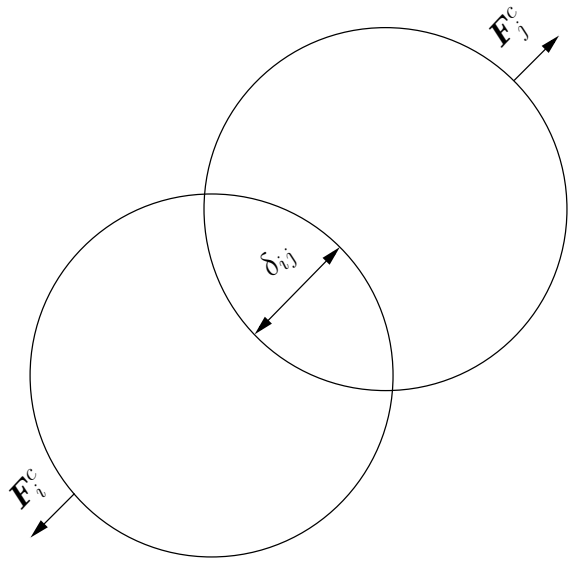

Figure 21 – Schematic depiction of the virtual overlap between the magnetic cores of two particles.

are

$$r_{ij} \sim \langle a \rangle, \quad U_i \sim U_s, \quad t \sim \frac{\langle a \rangle}{U_s}, \quad \Omega_i \sim \frac{U_s}{\langle a \rangle} \quad F_i \sim 6\pi\eta\langle a \rangle U_s,$$
$$T_i \sim 8\pi\eta\langle a \rangle^2 U_s \quad \text{and} \quad H \sim H_0, \quad (4.6)$$

where $U_s = 2\Delta\rho\langle a \rangle^2 g/9\eta$ is the Stokes velocity of a particle of radius $\langle a \rangle$ and H_0 is a suitable scale of the external magnetic field: the intensity of a constant field or $M/4\pi$ in the case of a rectangular prismatic magnet.

In non-dimensional form the equations of motion become

$$St\,\tilde{a}_i^3 \frac{d\tilde{\boldsymbol{U}}_i}{d\tilde{t}} = \tilde{\boldsymbol{F}}_i^h + \tilde{\boldsymbol{F}}_i^d + \tilde{\boldsymbol{F}}_i^m + \tilde{\boldsymbol{F}}_i^b + \tilde{\boldsymbol{F}}_i^r + \tilde{\boldsymbol{F}}_i^c + \tilde{\boldsymbol{F}}_i^g \quad (4.7)$$

and

$$\frac{3St\,\tilde{a}_i^5}{10} \frac{d\tilde{\boldsymbol{\Omega}}_i}{d\tilde{t}} = \tilde{\boldsymbol{T}}_i^h + \tilde{\boldsymbol{T}}_i^d + \tilde{\boldsymbol{T}}_i^m + \tilde{\boldsymbol{T}}_i^b. \quad (4.8)$$

In the following, we provide the non-dimensional expressions of these forces and torques.

- **Hydrodynamical**:

$$\begin{bmatrix} \tilde{\boldsymbol{U}}_1 \\ \vdots \\ \tilde{\boldsymbol{U}}_N \\ \tilde{\boldsymbol{\Omega}}_1 \\ \vdots \\ \tilde{\boldsymbol{\Omega}}_N \end{bmatrix} = - \begin{bmatrix} \tilde{\mathbf{a}}^{11} & \cdots & \tilde{\mathbf{a}}^{1N} & \tilde{\boldsymbol{b}}^{11} & \cdots & \tilde{\boldsymbol{b}}^{1N} \\ \vdots & \ddots & \vdots & \vdots & \ddots & \vdots \\ \tilde{\mathbf{a}}^{N1} & \cdots & \tilde{\mathbf{a}}^{NN} & \tilde{\boldsymbol{b}}^{N1} & \cdots & \tilde{\boldsymbol{b}}^{NN} \\ \tilde{\mathbf{b}}^{11} & \cdots & \tilde{\mathbf{b}}^{1N} & \tilde{\mathbf{c}}^{11} & \cdots & \tilde{\mathbf{c}}^{1N} \\ \vdots & \ddots & \vdots & \vdots & \ddots & \vdots \\ \tilde{\mathbf{b}}^{N1} & \cdots & \tilde{\mathbf{b}}^{NN} & \tilde{\mathbf{c}}^{N1} & \cdots & \tilde{\mathbf{c}}^{NN} \end{bmatrix} \begin{bmatrix} \tilde{\boldsymbol{F}}_1^h \\ \vdots \\ \tilde{\boldsymbol{F}}_N^h \\ \tilde{\boldsymbol{T}}_1^h \\ \vdots \\ \tilde{\boldsymbol{T}}_N^h \end{bmatrix}, \tag{4.9}$$

where the non-dimensional mobility matrices are

$$\tilde{\mathbf{a}}^{ii} = \frac{\boldsymbol{I}}{\tilde{a}_i}, \tag{4.10}$$

$$\tilde{\mathbf{a}}^{ij} = \frac{3}{4\tilde{r}_{ji}} \left[\boldsymbol{I} + \hat{\boldsymbol{r}}_{ji}\hat{\boldsymbol{r}}_{ji} + \frac{\tilde{a}_i^2 + \tilde{a}_j^2}{3\tilde{r}_{ji}^2} \left(\boldsymbol{I} - 3\hat{\boldsymbol{r}}_{ji}\hat{\boldsymbol{r}}_{ji} \right) \right], \quad j \neq i, \tag{4.11}$$

$$\tilde{\boldsymbol{b}}^{ii} = \mathbf{0}, \tag{4.12}$$

$$\tilde{\boldsymbol{b}}^{ij} = -\frac{\boldsymbol{\varepsilon} \cdot \hat{\boldsymbol{r}}_{ji}}{\tilde{r}_{ji}^2}, \quad j \neq i, \tag{4.13}$$

$$\tilde{\mathbf{b}}^{ii} = \mathbf{0}, \tag{4.14}$$

$$\tilde{\mathbf{b}}^{ij} = -\frac{3\boldsymbol{\varepsilon} \cdot \hat{\boldsymbol{r}}_{ji}}{4\tilde{r}_{ji}^2}, \quad j \neq i, \tag{4.15}$$

$$\tilde{\mathbf{c}}^{ii} = \frac{\boldsymbol{I}}{\tilde{a}_i^3} \tag{4.16}$$

and

$$\tilde{\mathbf{c}}^{ij} = \frac{1}{2\tilde{r}_{ji}^3} (\boldsymbol{I} - 3\hat{\boldsymbol{r}}_{ji}\hat{\boldsymbol{r}}_{ji}), \quad j \neq i. \tag{4.17}$$

- **Magnetic dipolar**:

$$\tilde{\boldsymbol{F}}_i^d = \lambda \sum_{\substack{j=1 \\ j \neq i}}^{N} \frac{(\tilde{a}_i - \tilde{\delta}_s)^3 (\tilde{a}_j - \tilde{\delta}_s)^3}{\tilde{r}_{ji}^4} [(\hat{\boldsymbol{m}}_i \cdot \hat{\boldsymbol{m}}_j)\hat{\boldsymbol{r}}_{ji} + (\hat{\boldsymbol{m}}_i \cdot \hat{\boldsymbol{r}}_{ji})\hat{\boldsymbol{m}}_j + (\hat{\boldsymbol{m}}_j \cdot \hat{\boldsymbol{r}}_{ji})\hat{\boldsymbol{m}}_i - 5(\hat{\boldsymbol{m}}_i \cdot \hat{\boldsymbol{r}}_{ji})(\hat{\boldsymbol{m}}_j \cdot \hat{\boldsymbol{r}}_{ji})\hat{\boldsymbol{r}}_{ji}] \tag{4.18}$$

and

$$\tilde{\boldsymbol{T}}_i^d = \frac{3\lambda}{4} \sum_{\substack{j=1 \\ j \neq i}}^{N} \frac{(\tilde{a}_i - \tilde{\delta}_s)^3 (\tilde{a}_j - \tilde{\delta}_s)^3}{\tilde{r}_{ji}^3} \left[(\hat{\boldsymbol{m}}_j \cdot \hat{\boldsymbol{r}}_{ji})\hat{\boldsymbol{m}}_i \times \hat{\boldsymbol{r}}_{ji} - \frac{1}{3}\hat{\boldsymbol{m}}_i \times \hat{\boldsymbol{m}}_j \right], \tag{4.19}$$

with $\tilde{\delta}_s = \delta_s / \langle a \rangle$.

- **External magnetic field**:

$$\tilde{\boldsymbol{F}}_i^m = \alpha \tilde{a}_i^3 \hat{\boldsymbol{m}}_i \cdot \tilde{\nabla} \tilde{\boldsymbol{H}} \tag{4.20}$$

and

$$\tilde{\boldsymbol{T}}_i^m = \frac{3\alpha \tilde{a}_i^3}{4} \hat{\boldsymbol{m}}_i \times \tilde{\boldsymbol{H}}. \tag{4.21}$$

- **Brownian**:

$$\tilde{\boldsymbol{F}}_i^b = \left(\frac{2\tilde{a}_i}{Pe \Delta \tilde{t}} \right)^{1/2} \mathbf{n}^F \tag{4.22}$$

and

$$\tilde{\boldsymbol{T}}_i^b = \left(\frac{3\tilde{a}_i}{2Pe \Delta \tilde{t}} \right)^{1/2} \mathbf{n}^T \tag{4.23}$$

with $\langle \mathbf{n}^F \rangle = \langle \mathbf{n}^T \rangle = \mathbf{0}$ and $\langle \mathbf{n}^F(\tilde{t}) \mathbf{n}^F(\tilde{t}) \rangle = \langle \mathbf{n}^T(\tilde{t}) \mathbf{n}^T(\tilde{t}) \rangle = \boldsymbol{I}$.

- **Steric layer repulsion**:

$$\tilde{\boldsymbol{F}}_{ij}^r = \begin{cases} -\dfrac{\pi \tilde{N}_{sup} (\tilde{a}_i + \tilde{a}_j - 2\tilde{\delta}_s)^2}{2\tilde{\delta}_s Pe} \ln \left(\dfrac{\tilde{a}_i + \tilde{a}_j}{\tilde{r}_{ij}} \right) \hat{\boldsymbol{r}}_{ij}, & -2\delta_s < \varepsilon_{ij} < 0, \\ \mathbf{0} \quad \text{otherwise}, \end{cases} \tag{4.24}$$

with

$$\tilde{\boldsymbol{F}}_i^r = \sum_{\substack{j=1 \\ j \neq i}}^{N} \tilde{\boldsymbol{F}}_{ij}^r \tag{4.25}$$

and $\tilde{N}_{sup} = N_{sup} \langle a \rangle^2$.

- **Contact forces**:

$$\tilde{\boldsymbol{F}}_{ij}^c = \begin{cases} -\tilde{\kappa} \left[\left(\dfrac{1}{\tilde{a}_i - \tilde{\delta}_s} + \dfrac{1}{\tilde{a}_j - \tilde{\delta}_s} \right)^{-1} \tilde{\delta}_{ij}^3 \right]^{1/2} \hat{\boldsymbol{r}}_{ij}, & \delta_{ij} > 0, \\ \mathbf{0} \quad \text{otherwise}, \end{cases} \tag{4.26}$$

with

$$\tilde{\boldsymbol{F}}_i^c = \sum_{\substack{j=1 \\ j \neq i}}^{N} \tilde{\boldsymbol{F}}_{ij}^c, \tag{4.27}$$

$\tilde{\kappa} = \langle a \rangle \kappa / 6\pi\eta U_s$ and $\tilde{\delta}_{ij} = \delta_{ij} / \langle a \rangle$.

- **Gravitational**:

$$\tilde{\boldsymbol{F}}_i^g = -\tilde{a}_i^3 \hat{\boldsymbol{e}}_3. \tag{4.28}$$

Now we define the non-dimensional parameters which appear in Eqs. (4.9) to (4.28). First, the already encountered Stokes and Péclet parameters are slightly altered, since the length scale is now the average radius of particles, but their form and meaning remain the same:

$$St = \frac{\mathcal{M} U_s}{6\pi\eta \langle a \rangle^2}, \tag{4.29}$$

quantifying the inertia of the particle relative to flow drag, with $\mathcal{M} = 4\pi\langle a\rangle^3\rho_s/3$ and

$$Pe = \frac{D_0}{\langle a\rangle U_s}, \tag{4.30}$$

a measure of Brownian forces, relative to flow forces, where

$$D_0 = \frac{k_{_B}T}{6\pi\eta\langle a\rangle}. \tag{4.31}$$

In addition to those, we also define a parameter of external magnetic field intensity,

$$\alpha = \frac{\mu_0 m_0 H_0}{6\pi\eta\langle a\rangle^2 U_s}, \tag{4.32}$$

and another of dipolar field intensity

$$\lambda = \frac{\mu_0 m_0^2}{8\pi^2\eta\langle a\rangle^5 U_s}. \tag{4.33}$$

We remark that these magnetic parameters α and λ are not the exact same parameters encountered in ferrofluids. They are defined by quotients of external magnetic field and dipolar interaction forces, respectively, and a fluid viscous drag scale not a thermal force, as in ferrofluids. A tacit physical parameter which is of utmost importance to the time evolution of the suspension is the volumetric fraction of particles, defined as the volume of particles over the total volume of the suspension. In our simulations, it amounts to

$$\phi = \frac{4\pi\langle a\rangle^3 N}{3\ell_x\ell_y\ell_z}, \tag{4.34}$$

where ℓ_x, ℓ_y and ℓ_z are the lengths of the sides of the container.

In view of the many simultaneous physical mechanisms at play in the suspension, a judicious choice of the numerical integration time step must be made. It should be sufficiently refined to capture all effects, yet not small enough that the computational cost of the simulation ceases to be feasible. In this work, we have chosen

$$\Delta\tilde{t} = \frac{1}{100}\min(1, 5Pe, 5St, \tilde{\varepsilon}), \tag{4.35}$$

where $\tilde{\varepsilon} = \max(\min(\varepsilon_{ij}), 5.10^{-4})$. This lower bound for $\tilde{\varepsilon}$ is a numerical strategy to avoid freezing of the simulation. We also set the parameters $\tilde{\delta}_s = 0.2$, $\tilde{N}_{sup} = 200$ and $\tilde{\kappa} = 10$ for all the particles.

4.2 Boundary Conditions, Initial Conditions and Geometry

The particle initial positions are randomly generated within a box of length $\ell_x = 25a$, width $\ell_y = 25a$ and height $\ell_z = 75a$, with an uniform probability distribution of the initial position in each direction, excluding volumes which had already been occupied by the previously generated particles. Initial linear velocities are null. Analogously, the

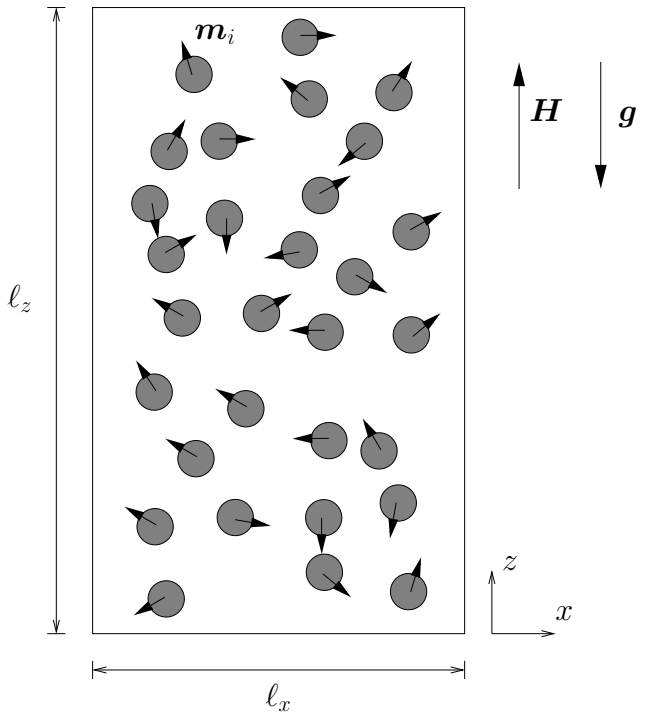

Figure 22 – Illustration of the initial condition of the numerical simulation. Magnetic field applied along the z direction, opposite to gravity.

initial orientations are uniformly distributed over a sphere of unitary radius and their initial angular velocites are null. Fig. (22) illustrates the initial condition.

We assumed a boundary condition of periodicity in all directions, such that the particles whose centers exit the box through one side are brought back inside through the opposite one. If this translation would result in an overlap of particles, Brownian displacements are applied to the center of the translated particle until no overlap occurs. Ensemble averages of all properties are calculated as averages first in the particles comprised in the box, then in the realizations.

We have not simulated polydisperse suspensions in this work, however we account for this possibility in our modeling, since we will address them in future works. The possibly unequal magnetic cores radii $\tilde{a}_{m,i} = \tilde{a}_i - \tilde{\delta}_s, i = 1, \cdots, N$, are generated according to a pseudo-random approximation to the log-normal distribution, since this is the distribution typically observed in experiments (MASSART et al., 1995). To this end, a pseudo-Gaussian distribution was produced by a Box-Muller algorithm (PRESS et al., 1992) providing a variable Y. Then the pseudo-log-normally distributed variable X was obtained by the variable transformation $X = \exp(Y)$. In fact, note that if Y has a Gaussian PDF

$$\tilde{P}(Y) = \frac{1}{\sqrt{2\pi\langle Y'^2; \tilde{P}\rangle}} \exp\left[-\frac{(Y - \langle Y; \tilde{P}\rangle)^2}{2\langle Y'^2; \tilde{P}\rangle}\right], \tag{4.36}$$

then the PDF of X is given by

$$P(X) = \frac{1}{\sqrt{2\pi\langle Y'^2; \tilde{P}\rangle}\, X} \exp\left[-\frac{(\ln X - \langle Y; \tilde{P}\rangle)^2}{2\langle Y'^2; \tilde{P}\rangle}\right] \tag{4.37}$$

where $\langle Y;\tilde{P}\rangle$ denotes an average with respect to the PDF $\tilde{P}$, rather than to P. Also note that the algorithm used furnishes Y with specified mean and variance but actually the quantities of interest are the mean and variance of X, which specify the actual radii distribution, therefore we are interested in writing $\langle Y;\tilde{P}\rangle$ and $\langle Y'^2;\tilde{P}\rangle$ in terms of $\langle X;P\rangle$ and $\langle X'^2;P\rangle$, so that these latter quantities enter the code as parameters of average radius and polydispersity. Eq. (4.37) implies

$$\langle X;P\rangle = \exp\left(\langle Y;\tilde{P}\rangle + \frac{1}{2}\langle Y'^2;\tilde{P}\rangle\right) \tag{4.38}$$

and

$$\langle X'^2;P\rangle = \left[\exp\left(\langle Y'^2;\tilde{P}\rangle\right) - 1\right]\exp\left(2\langle Y;\tilde{P}\rangle + \langle Y'^2;\tilde{P}\rangle\right), \tag{4.39}$$

thus the inversion of Eqs. (4.38) and (4.39) achieves the desired end,

$$\langle Y;\tilde{P}\rangle = \ln\left[\frac{\langle X;P\rangle^2}{\sqrt{\langle X;P\rangle^2 + \langle X'^2;P\rangle}}\right] \tag{4.40}$$

and

$$\sqrt{\langle Y'^2;\tilde{P}\rangle} = \ln\left(\frac{\langle X;P\rangle^2 + \langle X'^2;P\rangle}{\langle X;P\rangle^2}\right). \tag{4.41}$$

When this procedure is applied for the particle magnetic core radii, the choice of non-dimensional length scale establishes the constraint $\langle\tilde{a}_{m,i}\rangle = 1-\tilde{\delta}_s$, which enters as an input. Furthermore, the radii standard deviation is interpreted as a measure of polydispersity of the radii.

A magnetic core radii distribution found by this method is displayed in Fig. (23).

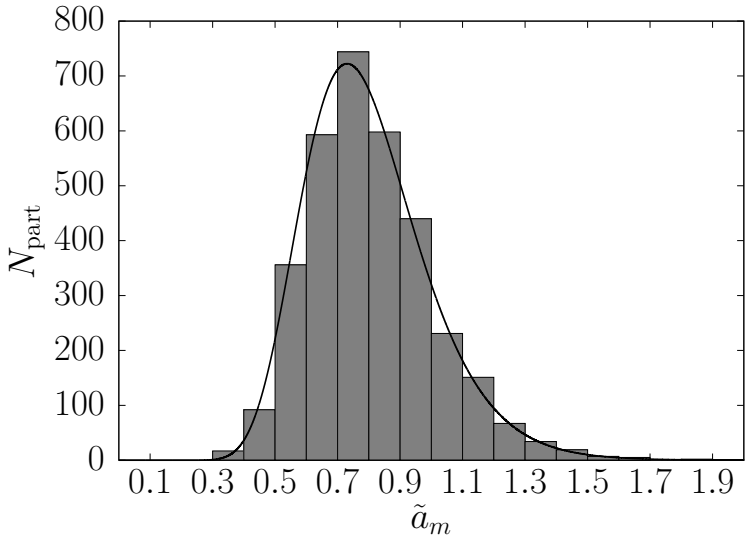

Figure 23 – Histogram of the hydrodynamic radii given by the computer generated pseudo log-normal distribution. The actual corresponding log-normal distribution is represented by a continuous line (—).

4.3 Properties of Suspensions

Besides the new mechanisms in the dynamics of particles in a suspension, another difference with respect to the analysis of a single particle is the possibility to use other descriptors to characterize it. In particular, since the hydrodynamic interactions depend on the relative distance of particles, describing the suspension configuration is fundamental. A quantity which provides an insight on this position distribution is the structure factor. Essentially, it is the ensemble average of the correlation of number densities in Fourier space, normalized by a suitable factor. That is, it measures how likely it is that the particles are at a given distance corresponding to a given wavenumber. In mathematical terms, the structure factor is given by

$$S(\boldsymbol{k}) = \frac{1}{N}\langle n^*(\boldsymbol{k},t)n(\boldsymbol{k},t)\rangle. \tag{4.42}$$

where $n(\boldsymbol{k},t)$ is the number density on the wavenumber $\boldsymbol{k}$ and the asterisk denotes complex conjugation. For point particles, the number density in configuration space is

$$n(\boldsymbol{x},t) = \sum_{\alpha=1}^{N} \delta(\boldsymbol{x}-\boldsymbol{x}_\alpha), \tag{4.43}$$

such that, when integrated over a region, it yields the total number of particles in that region. Its dependence on the wavenumber follows from its Fourier transform,

$$n(\boldsymbol{k},t) = \int_{\mathbb{R}^3} n(\boldsymbol{x},t)\exp(-i\boldsymbol{k}\cdot\boldsymbol{x})\,\mathrm{d}\boldsymbol{x}, \tag{4.44}$$

whence

$$n(\boldsymbol{k},t) = \sum_{\alpha=1}^{N} \exp(-i\boldsymbol{k}\cdot\boldsymbol{x}_\alpha). \tag{4.45}$$

Therefore, the structure factor for point particles reduces to

$$S(\boldsymbol{k}) = \frac{1}{N}\left\langle \sum_{\alpha,\beta=1}^{N} \exp[i\boldsymbol{k}\cdot(\boldsymbol{x}_\beta-\boldsymbol{x}_\alpha)]\right\rangle, \tag{4.46}$$

and by symmetry, it is calculated by

$$S(\boldsymbol{k}) = 1 + \frac{2}{N}\left\langle \sum_{\alpha=1}^{N}\sum_{\beta<\alpha} \cos[\boldsymbol{k}\cdot(\boldsymbol{x}_\beta-\boldsymbol{x}_\alpha)]\right\rangle \tag{4.47}$$

It should be noted that in general, the structure factor depends on the direction of the wavenumber, so in our simulations we calculate it along directions parallel and perpendicular to gravity, in order to compare them.

In a brief side note, it should be mentioned that some authors prefer to work with the pair-distribution function than with the structure factor. Given the probability that any particle is found at $\boldsymbol{x}_1$ and any other at $\boldsymbol{x}_2$, $n^{(2)}(\boldsymbol{x}_1,\boldsymbol{x}_2)$, the pair-distribution function, $g(r)$, is given by (MCQUARRIE, 2000)

$$n^{(2)}(\boldsymbol{x}_1,\boldsymbol{x}_2) = n^2 g(\boldsymbol{x}_1,\boldsymbol{x}_2) \tag{4.48}$$

with $n = N/V$. If the positions of both particles were independent, we would have $g(r) = 1$, with $r = |\boldsymbol{x}_2 - \boldsymbol{x}_1|$. Therefore, the pair-distribution function measures the correlation between the spacial location of the particles, its higher values indicating higher likeliness of the corresponding particle distances. However, note that the structure factor is directly related to the pair-distribution function by a Fourier transform. Indeed, it can be shown that (DHONT, 1996)

$$S(\boldsymbol{k}) = 1 + n \int g(r) \exp(i\boldsymbol{k} \cdot \boldsymbol{r})\, d\boldsymbol{r}. \tag{4.49}$$

Since the structure factor is more directly calculated and provides the same information, we chose to use it rather than the pair-distribution function to obtain information about the microstructure.

In addition to the likeliness of relative positions of particles, the structure factor also conveys information about convective currents induced in the fluid domain. In fact, an imbalance in particle number leads to a weight excess of volumes containing greater numbers of particles. Thus, they settle at relatively higher speeds, inducing convective currents. Their relation to the structure factor follows from the fact that fluctuations in the number density are proportional to the average modulus of the number density, i.e., $\sqrt{n'^2} \sim \sqrt{\langle |n|^2 \rangle}$. For example, in a system in thermodynamic equilibrium, the structure factor is equal to 1 (MATTIS, 2004), such that Eq. (4.42) yields $\sqrt{n'^2} \sim \sqrt{N}$. Fig. (24) presents a box of particles in thermodynamic equilibrium which is divided by an imaginary line in two equal parts. Instead of having an equal number of particles in each side, we find that one side will typically contain a surplus of the order of $\sqrt{N}$ particles, and the other side a deficit of the same amount, inducing these convective currents that tend to mix both sides.

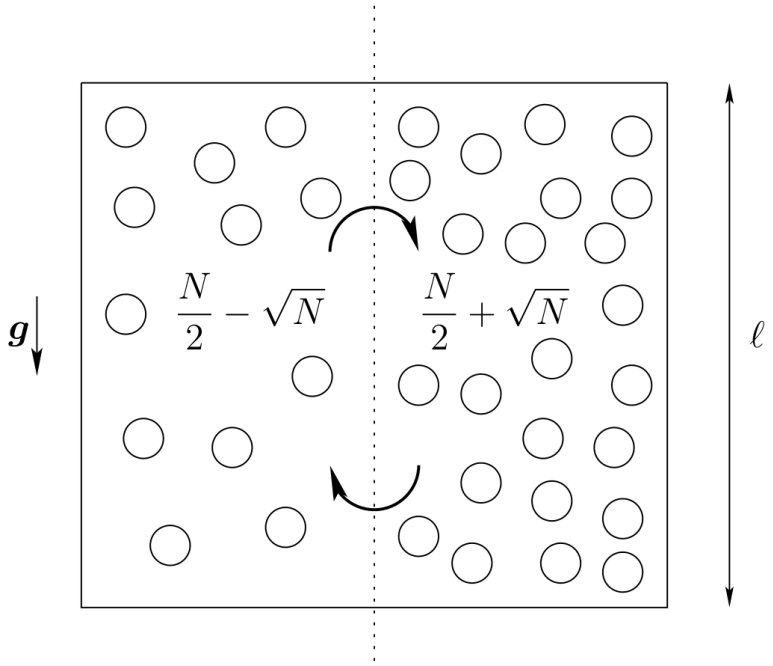

Figure 24 – Convective current induces by the extra weight in one side of the box. Adapted from (HINCH, 1988; ABADE, 2005).

Especially in magnetic suspensions, the number of aggregates and their average size are an important feature implicit in the particle configuration, with relevance to the dynamics of the suspension. Indeed, particles in chains linked by dipolar interaction have a restrained motion, however the action of large chains over an isolated particle may promote large velocity fluctuations. The competition between these mechanisms is important to the particle-phase pressure of the system and the conclusion of which mechanism dominates the collective motion may be drawn from the distribution of number of particles per aggregate.

In order to determine the number of particles per aggregate, we developed a simple depth-first search algorithm. It tags a given particle and then every other one connected to it by a chain recursively. We consider that two particles form an aggregate if they overlap, since this configuration is favored by the conjunct action of the external field and dipolar forces. The depth-first search works as described in Algorithm (1). Fig. (25) illustrates the method by a simple example, where the connected particles are schematically linked by continuous line. In this example, the algorithm would proceed as follows:

1. Tag particle 1;
2. Tag particle 2, since it is connected to 1, and restart the search starting from particle 2;
3. Tag particle 5, which is the only one connected to 2 and not tagged;
4. Go back to particle 1 to finish the search, because every restart (new search) has been finished;
5. Tag particle 3 and finish the search which started with particle 1, counting a total of 4 particles in the aggregate;
6. Similarly, a new search would be started at particle 4, tag it, count particle 8 and tag it, and finish, counting a two-particle aggregate;
7. Tag particle 6 and count it as a one-particle "aggregate";
8. Likewise for particle 7, tag it and count it as a one-particle "aggregate".

Input: links(i,j) between overlapping particles
Result: The histogram of number particles per aggregate
Initialization: tagged $\leftarrow$ false
for $i \leftarrow 1$ **to** N **do**
  if tagged *(i) false* **then**
    count=0;
    DFS (i,tagged (i),count);
  end
end
Function: DFS(i,tagged *(i)*,*count*)
tagged(i)$\leftarrow$true;
count=count+1;
for $j \leftarrow 1$ **to** N **do**
  if links(i,j) *true* ***and*** tagged(i) *false* **then**
    DFS(j);
  end
end
Algorithm 1: Algorithm of depth-first search to count number of aggregates.

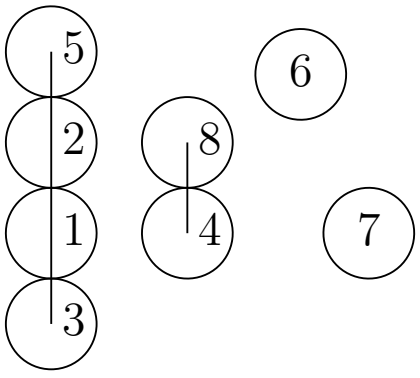

Figure 25 – Schematic representation of aggregates. The particles are numbered, as in the simulation, and the aggregates are indicated by continuous lines that connect the centers of the particles.

5 Numerical Simulation of Transport Properties

In this chapter, we numerically simulate dilute suspensions of massive sedimenting particles. We characterize their velocity fluctuations through both short-time and long-time statistical properties. In this first group, we are interested in the variance of velocity fluctuations and their associated particle-phase pressure. In the second, we are concerned with the autocorrelation of the velocity fluctuations and the diffusivity. In addition, we investigate the structure evolution of the suspension. Our intention is to describe the formation of chain-like structures in the magnetic case and determine the property changes promoted by the presence of these structures. The regime explored is only weakly Brownian, with $Pe = 10$.

5.1 Non-Magnetic Suspensions

We start by the characterization of non-magnetic suspensions. Our interest lies in determining how the main parameters of non-magnetic suspensions influence their short-time and long-time properties. These parameters are the Stokes number, the Péclet number and the volume fraction of particles. We remark that a typical configuration of $\phi = 0.01$ corresponds to a total of $N = 111$ particles in the box, with dimensions $\ell_x = 25a$, $\ell_y = 25a$ and $\ell_z = 75a$. The size of the container is kept constant throughout all the simulations, so the number of particles grows linearly with the volume fraction, attaining a maximum of $N = 333$ for simulations with $\phi = 0.03$.

Fig. (26) illustrates a typical time evolution of the suspension obtained from our numerical simulations, from the initial particle distribution until a non-dimensional time $\tilde{t} = 2.5$, respectively. While in Fig. (26a) the particle distribution appears to be more statistically homogeneous, in Fig. (26e) we observe a shift in the distribution of large void regions inside the numerical box. The particle velocity fluctuations induced by their hydrodynamic interactions and the near field forces can produce different transitions in the particle distribution, as shown by the structure factors, as well as they define the effect of a particle pressure in the suspension. Indeed, a shift in the peaks of the structure factors is observed over time, outlining the time evolution of the most probable distances of particles

and also the length scale of the structures in the suspension. The configuration anisotropy is also verified in the structure factor, with peaks at different wavenumbers for both directions. Our simulations for dilute suspensions show clear evidence of a particle-phase pressure opposite to aggregate formation or suspension instability, which also reflects in the gradual modification of the distribution of local maxima and minima in the structure factors. In fact, the presence of remarked local maxima and minima throughout the whole wavenumber range indicates that convective currents occur in all observed lengthscales.

The results of a simulation performed with $St = 0.1$, $Pe = 10$ and $\phi = 0.01$ are shown in Figs. (27) and (28). The variance of velocity fluctuations is observed to attain a statistically steady regime. The bumps noticed in its values are statistical fluctuations due to the number of realizations of the simulation, which is limited by computational cost. It is seen that the variance of the velocity fluctuations is enhanced due to the effects of hydrodynamic interactions. Furthermore, it takes a longer time to reach its steady state value, i.e., it has a longer correlation time parallel to gravity, showing that the velocity variance and the correlation time are significantly anisotropic, with $\langle U_{\parallel}'^2\rangle/\langle U_{\perp}'^2\rangle \sim 2$. This in turn ensues a slower decay of the velocity autocorrelation in the gravity direction, with a non-dimensional correlation time $\tilde{\tau}_{c\parallel} \sim 0.7$, thus the suspension presents a higher diffusivity when hydrodynamic interactions are present. In fact, in the absence of an imposed shear flow, the velocity fluctuations of non-Brownian particles arise solely due to the hydrodynamic interactions among the particles. In addition, it shows that when the motion of the particles is coupled by hydrodynamic interactions, cf. Eqs. (4.7) and (4.9), the action of gravity inserts memory in the system, especially along its direction, yielding the non-exponential decay of Fig. (28) and resulting in a non-Markovian diffusion process and anisotropic diffusivities. Under this condition a diffusivity tensor can be defined as follows:

$$\boldsymbol{D} = D_{\parallel}\hat{\boldsymbol{e}}_3\hat{\boldsymbol{e}}_3 + D_{\perp}(\boldsymbol{I} - \hat{\boldsymbol{e}}_3\hat{\boldsymbol{e}}_3), \tag{5.1}$$

with coefficients parallel to gravity denoted by $\parallel$ and those perpendicular to it by $\perp$.

Next, we explore the dependence of the properties on the particle volume fraction. The velocity fluctuations variance is depicted in Fig. (29). In the direction parallel to gravity, it is seen to grow roughly linearly with ϕ, whereas it remains approximately constant in the direction perpendicular to gravity. It should be noted that the coefficient $1/PeSt$ is incorporated for consistency with Eq. (3.22), which is the correct solution for the limit $\phi \to 0$. Similarly, we see from Fig. (30) that the diffusivity parallel to gravity grows steeply with the volumetric fraction. Meanwhile, it depends much more mildly on ϕ in the direction orthogonal to gravity.

In consonance with the preceding study of an isolated particle, the same parameters present there also appear in the equation of motion of the suspension and retain their importance over its macroscopic properties. Fig. (32) depicts this influence over the velocity fluctuations, showing that they are strongly hindered by the inertia of particles. In the horizontal direction, they show good qualitative agreement with the isolated particle

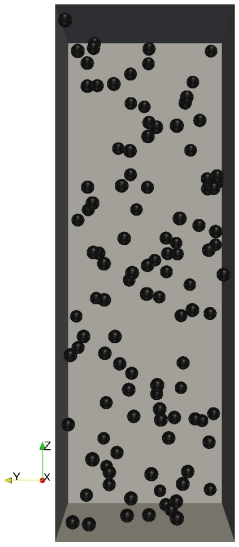

(a) $\tilde{t} = 0$.

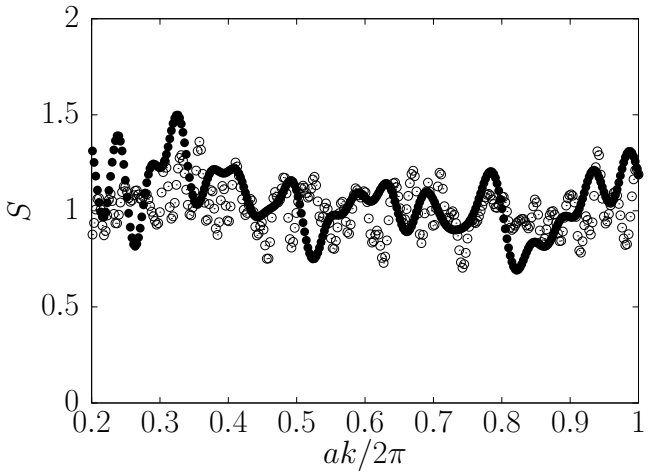

(b) Structure factor at $\tilde{t} = 0$.

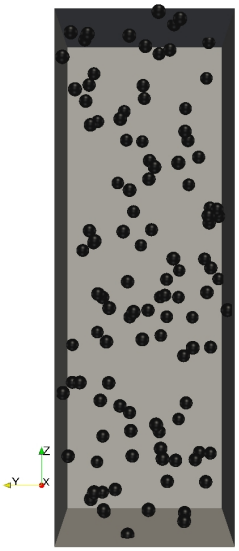

(c) $\tilde{t} = 1.25$.

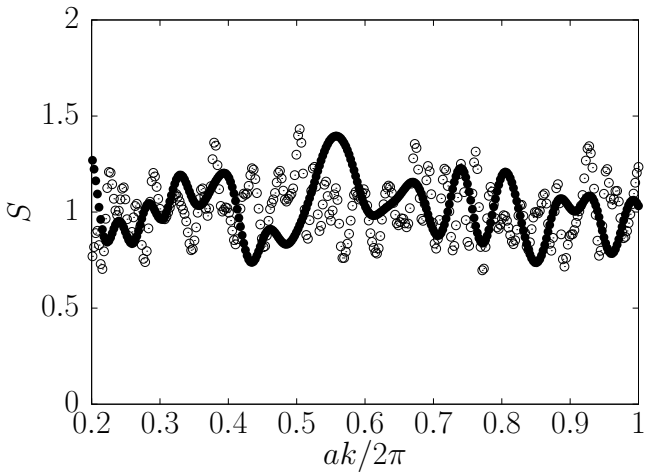

(d) Structure factor at $\tilde{t} = 1.25$.

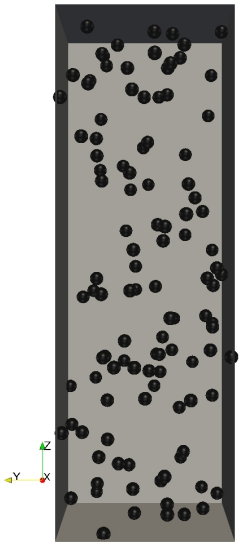

(e) $\tilde{t} = 2.5$.

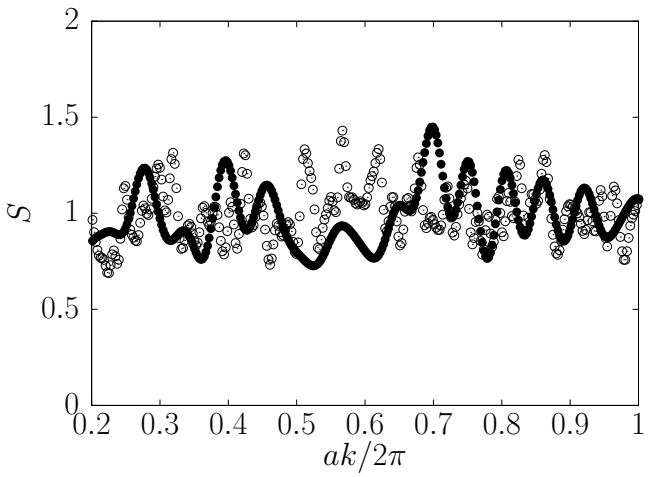

(f) Structure factor at $\tilde{t} = 2.5$.

Figure 26 – Typical time evolution of the suspension configuration in a three-dimensional numerical box and the corresponding structure factors, in the directions perpendicular (•) and parallel (○) to gravity. The numerical simulation was performed with $\phi = 0.01$, $St = 0.1$ and $Pe = 10$.

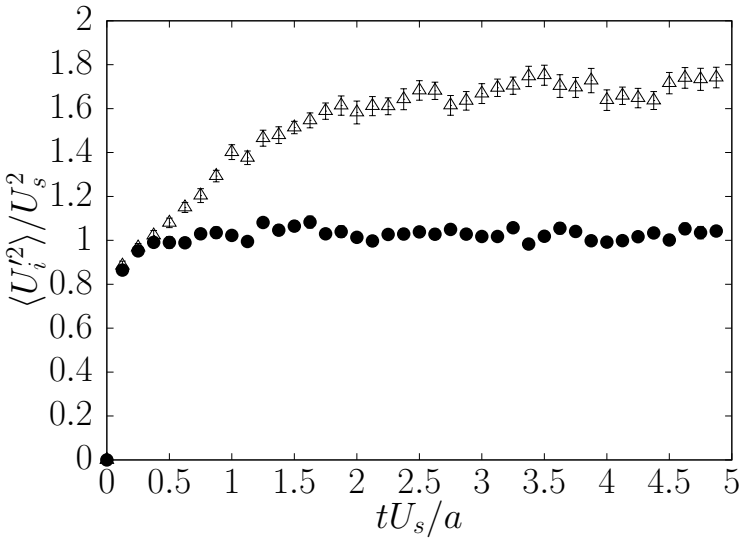

Figure 27 – Non-dimensional velocity fluctuation variances perpendicular (•) and parallel (△) to gravity for a monodisperse low Reynolds number suspension with $St = 0.1$, $Pe = 10$ and $\phi = 0.01$. Statistics were made over 50 realizations.

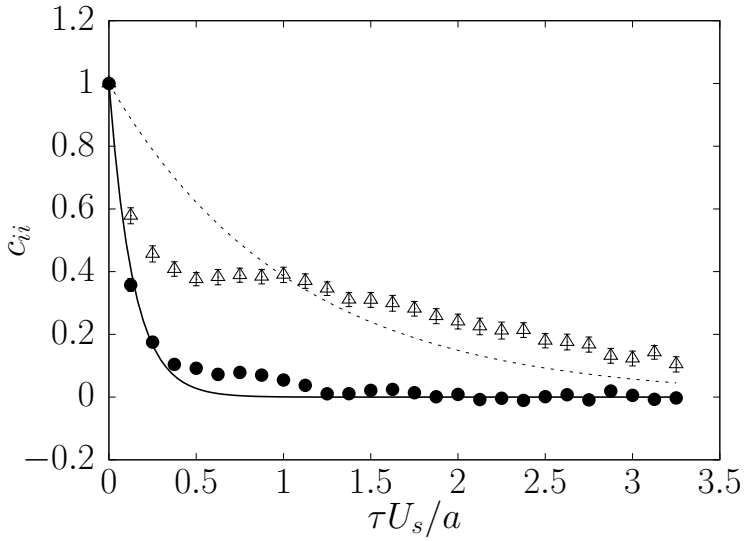

Figure 28 – Normalized autocorrelation of velocity fluctuations perpendicular (•) and parallel (△) to gravity for a monodisperse low Reynolds number suspension with $St = 0.1$, $Pe = 10$ and $\phi = 0.01$. Statistics were made over 50 realizations. Exponential fits $c_{11} = \exp(-\tau/\tau_{c1})$ (continuous line), with $\tau_{c1} = 0.139 \pm 0.002$ and $c_{33} = \exp(-\tau/\tau_{c3})$ (dashed line), with $\tau_{c3} = 1.05 \pm 0.02$.

decay given by Eq. (3.22), in contrast to the direction parallel to gravity. However, the anisotropy caused by hydrodynamic interactions is seen to decrease with an increasing of the Stokes number. We argue that this reduction results from an increase in the relaxation time of the particles, $\tau_r = \mathcal{M}/6\pi\eta a$. Indeed, the Stokes number is the non-dimensional relaxation time of the particles. When it becomes much larger than a characteristic time of hydrodynamic interaction between two particles, $\tau_h \sim \ell_h/\sqrt{\langle U'^2 \rangle}$ (ℓ_h is a characteristic length of hydrodynamic interaction between particles), the particles settle through this region of hydrodynamic interaction with a neighbor without responding to the forces that it produces. Fig. (31) illustrates this effect. It should be pointed out that as the Stokes

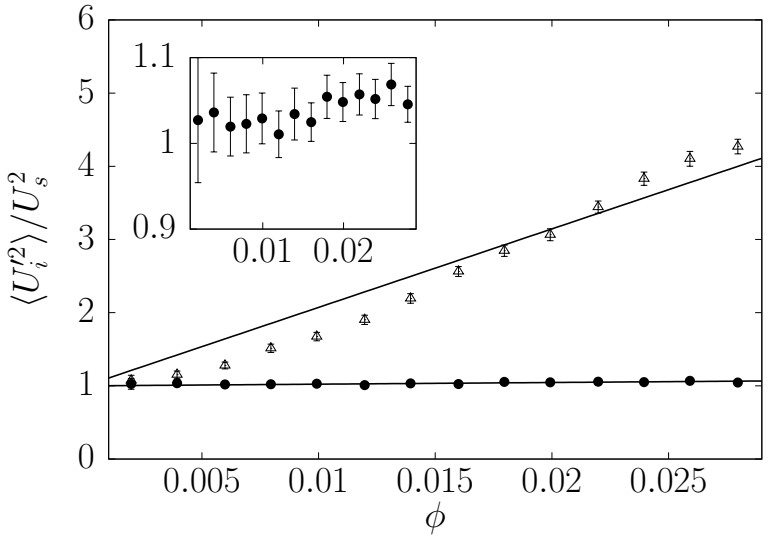

Figure 29 – Non-dimensional velocity fluctuation variances perpendicular (•) and parallel (△) to gravity in terms of the volume fraction of particles, for a monodisperse low Reynolds number suspension with $St = 0.1$ and $Pe = 10$. Statistics were performed over 50 realizations. The associated error bars are also shown in the plot. Linear fits $\langle \tilde{u}_\parallel'^2 \rangle = [1 + (107 \pm 4)\phi]/PeSt$ and $\langle \tilde{u}_\perp'^2 \rangle = [1 + (2.3 \pm 0.2)\phi]/PeSt$. The inset amplifies the variance of perpendicular velocity fluctuations.

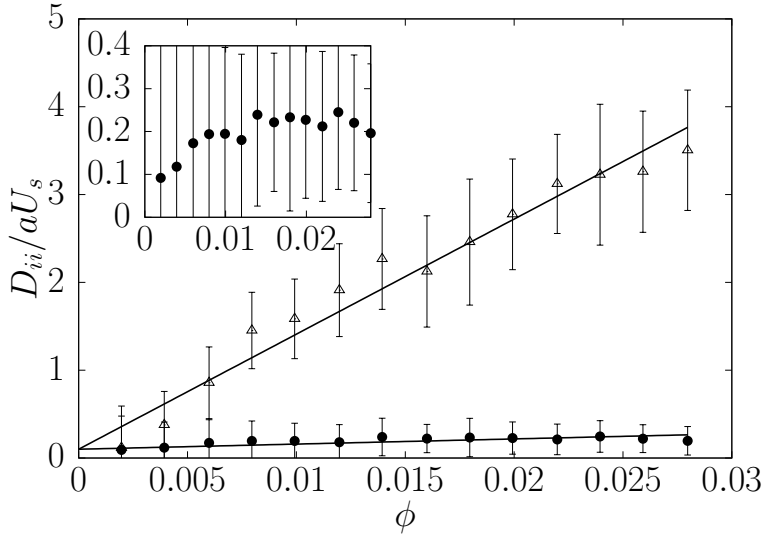

Figure 30 – Non-dimensional diffusivity perpendicular (•) and parallel (△) to gravity in terms of the volume fraction of particles, for a monodisperse low Reynolds number suspension with $St = 0.1$ and $Pe = 10$. Statistics were performed over 50 realizations. The associated error bars are also shown in the plot. Linear fits $\tilde{D}_\parallel = [1 + (131 \pm 3)\phi]/Pe$ and $\tilde{D}_\perp = [1 + (5.8 \pm 0.5)\phi]/Pe$. The inset amplifies the perpendicular diffusivity.

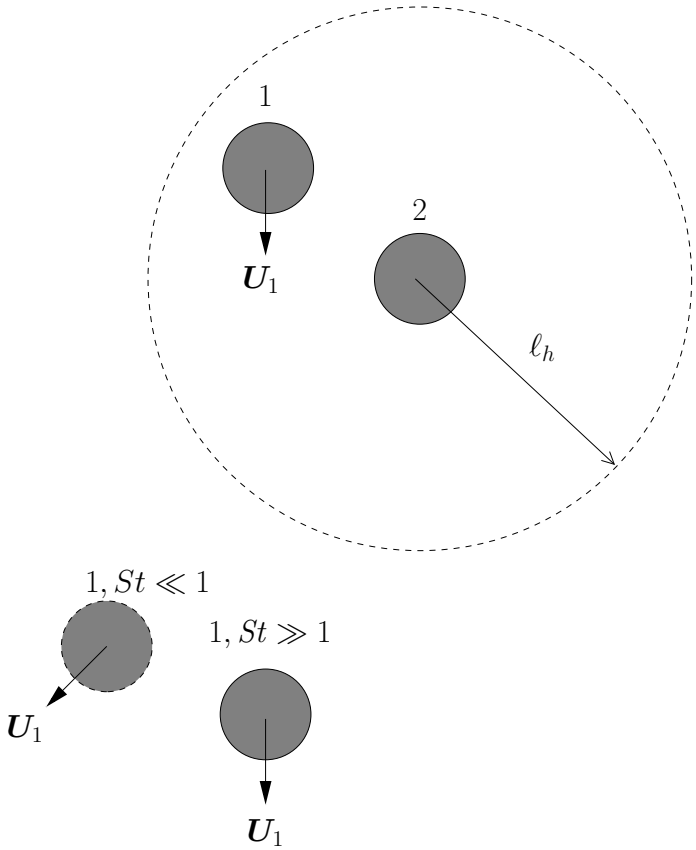

Figure 31 – Velocity fluctuations produced by hydrodynamic interactions of a particle 2 over a particle 1, in a suspension. When the Stokes number is high, particle 1 is less susceptible to hydrodynamic interactions and it settles beyond the region of interaction without alteration of its trajectory. For small Stokes numbers, particle 1 changes significantly its trajectory and velocity due to hydrodynamic interactions.

number is increased, collisions increase their relative importance as the mechanism responsible for the velocity fluctuations, therefore we claim that this change in the nature may be responsible for altering their decay scaling from St^{-1} to $St^{-2/3}$ in an inertial regime. A quantitative observation of this claim is computationally costly, once the regime of high Stokes numbers is associated to elevated relaxation times, requiring longer times of simulation in order to attain steady states of the properties.

5.1.1 Particle Pressure

Knowing the velocity fluctuations at a hydrodynamic scale, we obtain a hydrodynamic fluctuations tensor of the solid phase by analogy with the kinetic theory of gases, cf. Sec. (2.1.5),

$$\boldsymbol{\sigma}_h = -\rho_s \phi \langle \boldsymbol{U}' \boldsymbol{U}' \rangle. \tag{5.2}$$

Its isotropic part is associated with a particle pressure,

$$p_p = \frac{\rho_s \phi}{3} \langle \boldsymbol{U}' \cdot \boldsymbol{U}' \rangle, \tag{5.3}$$

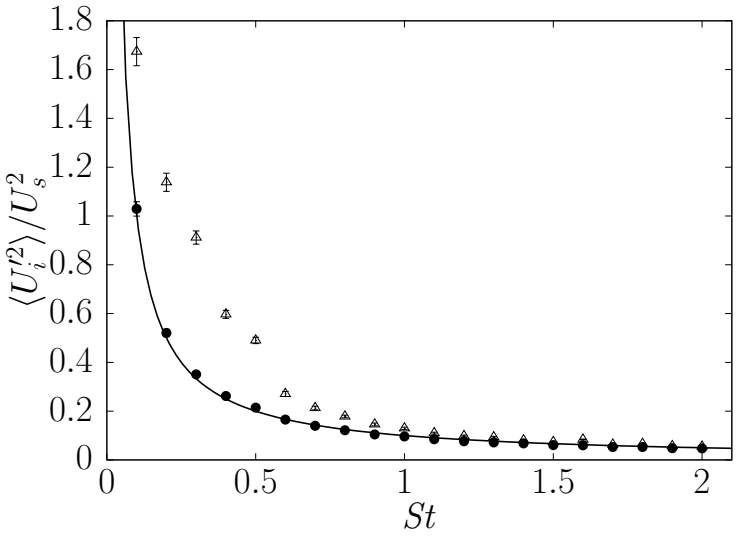

Figure 32 – Non-dimensional velocity fluctuation variances perpendicular (•) and parallel (△) to gravity in terms of the Stokes number, for a monodisperse low Reynolds number suspension with $\phi = 0.01$ and $Pe = 10$. Statistics were performed over 50 realizations. The associated error bars are also shown in the plot. Eq. (3.22) is represented by a solid line (—).

whereas its deviatoric part furnishes a particle viscosity, say

$$\eta_p = \frac{\rho_s \phi}{\dot{\gamma}} \langle U_2' U_3' \rangle. \tag{5.4}$$

In the present context, a particle pressure arises when momentum is transported by the hydrodynamic particle velocity fluctuations and also by eventual interparticle collisions (i.e. near field interactions), which transport momentum from the center of one particle to another. This particle pressure acts against particle concentration gradients, tending to homogenize the solid phase, whereas a particle viscosity attenuates low wavenumber fluctuations. As mentioned before, Fig. (26) shows from a qualitative point of view the action of the particle pressure in our dilute suspension, just filling out depleted volumes of particles or in a reverse way spreading aggregative regions of particles and so giving rise to several transitions of the spatial particle distribution.

Suitable choices for the dependence of the solid phase pressure and viscosity on the particle volume fraction are often proposed (DURU et al., 2002; SUNDARESAN, 2003) since the continuum models of interacting phases frequently use Newtonian constitutive equations for the stress tensor describing the dispersed phase. For instance

$$\boldsymbol{\sigma}_p = -p_p(\phi)\boldsymbol{I} + 2\eta_p(\phi)\left(\boldsymbol{d} - \frac{\nabla \cdot \boldsymbol{v}}{3}\boldsymbol{I}\right), \tag{5.5}$$

where $\boldsymbol{d}$ is the rate of strain tensor and $\boldsymbol{v}$ the solid phase velocity field, used in attempts to solve two-phase flows and determine conditions of their stability (HOMSY; EL-KAISSY; DIDWANIA, 1980; KOCH, 1990). This connection between the properties provided by computational simulations of mesoscopic suspensions and their use in continuum models highlights the relevance of hybrid methods, in which both approaches are combined.

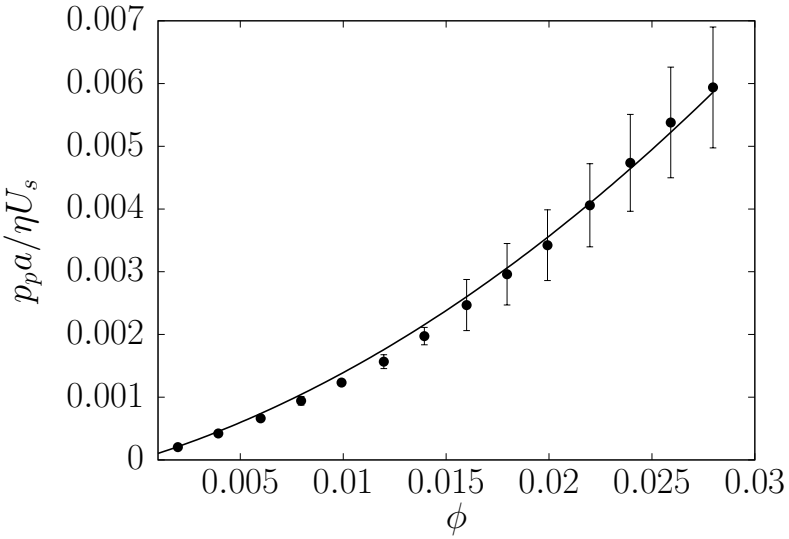

Figure 33 – Non-dimensional particle pressure in terms of the volume fraction of particles, for a monodisperse low Reynolds number suspension with $St = 0.1$ and $Pe = 10$. Statistics made over 50 realizations, quadratic fit $\tilde{p}_p = [\phi + (39 \pm 1)\phi^2]/Pe$.

We determined the particle pressure from our simulations for different values of particle volume fraction, as shown in Fig. (33), whence we obtained a first-order correction in ϕ for this property, as presented in Tab. (2). We can see that our correction of the diffusivity perpendicular to gravity as a direct consequence of hydrodynamic interactions is comparable to the theoretical result of Batchelor (1976) for an isotropic suspension, $D = 1.45\phi$. Furthermore, Batchelor's result is based upon an assumption of a statistically homogeneous suspension. In contrast, the time evolution of our suspension leads to anisotropic configurations, which is reflected by the anisotropy of transport coefficients. Thus, for instance, we are able to determine the ratio of the diffusion coefficients parallel and perpendicular to gravity, $D_\parallel/D_\perp \approx 20$, which is an order greater than the one found in experiments, cf. (GUAZZELLI; HINCH, 2011), but in good agreement with other numerical simulations, see (CUNHA et al., 2002; KOCH, 1994). On the other hand, the effect of particle viscosity associated with the velocity fluctuations is still negligible in the dilute regimes explored here. In a dilute regime the particle pressure has a stabilizing effect on the suspension making the suspension more statistically homogeneous. This occurs because the particle pressure in a dilute regime always increases with an increasing of the particle volume fraction ϕ.

Table 2 – Approximate numerical values for the first-order correction of macroscopic properties.

$\langle U_\parallel'^2 \rangle$	$\langle U_\perp'^2 \rangle$	$D_\parallel$	$D_\perp$	p_p
$\frac{110 k_B T}{m}\phi$	$\frac{2 k_B T}{m}\phi$	$130 D_0 \phi$	$6 D_0 \phi$	$\frac{40 D_0 \eta}{a^2}\phi^2$

5.2 Magnetic Suspensions

5.2.1 Dipolar Interactions

Now we present results of simulations for a magnetic suspension of spherical particles. We examine how the external magnetic field and the dipolar interactions influence transport properties as well the time evolution of the suspension configuration. First we analyze the effect of dipolar interactions with a fixed field. A fundamental difference with respect to the case of non-magnetic suspensions is the formation of chain-like structures of aggregated particles. We examine how the aggregative effect of magnetic dipolar interactions influences the dynamical behavior of the suspension, in contrast to the dispersive effect of hydrodynamic interactions.

Fig. (34) shows the time evolution of velocity fluctuations in the suspension. Its values remain anisotropic, larger in the direction of gravity than in the orthogonal direction. Their anisotropy ratio is of order $\langle U_{\parallel}'^2 \rangle / \langle U_{\perp}'^2 \rangle \sim 2$, comparable to the non-magnetic case, cf. Fig. (27). In the presence of stronger dipolar interactions, velocity fluctuations orthogonal to gravity decay with time at a steady rate, breaking the stationary character of the statistical process. This is due to a continued formation of larger chains of particles, suppressing motions of the aggregated particles, especially in the direction orthogonal to the field. Also for this reason, the time averages[1] of these fluctuations decrease with the increasing of the dipolar interactions, as shown in Fig. (35). However, for sufficiently elevated values of dipolar interaction, not all points do seem to follow this downward trend. We argue that this is associated with the formation of larger chains, of 3 or 4 particles, which are now clusters heavily influencing the motion of isolated particles. From this point on, it is likely that magnetic interactions between clusters and particles becomes more relevant and determines the velocity fluctuations. However their effect is not obvious, since the larger induced magnetic fields are now compensated by increased inertia of the clusters and this interplay of mechanisms may induce further reduction of velocity fluctuations.

This screening of velocity fluctuations is observed as well in numerical simulations of magnetic fluidized beds (WANG et al., 2013), where it promotes voidage control and enhances the bed performance. This hindrance is also reflected in the particle pressure presented in Fig. (36). A core contribution of our work, the characterization of a particle pressure associated to the fluctuations, shows to be especially valuable in magnetic suspensions, where expressions relating it to external field and dipolar interaction effects are lacking.

Our observations about chain-like structure formation and its influence over the dynamics of the velocity fluctuations are further supported by a histogram of the relative

[1] Time averages are calculated starting after a sufficient number of steps to render the statistics independent of initial conditions.

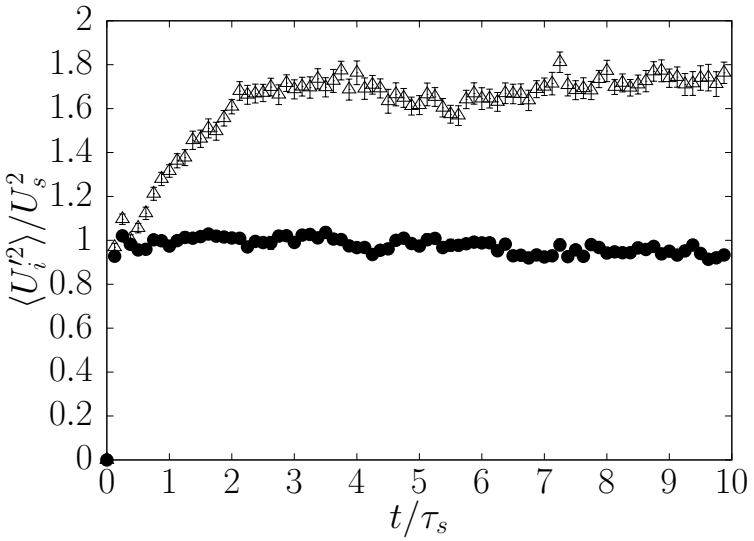

(a) $\lambda = 20$.

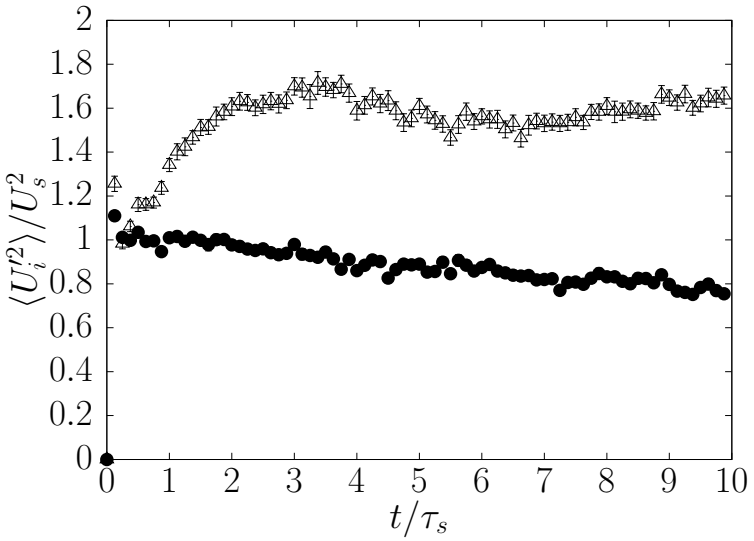

(b) $\lambda = 80$.

Figure 34 – Non-dimensional variance of the velocity fluctuations perpendicular (•) and parallel (△) to gravity as a function of time for a monodisperse magnetic low Reynolds number suspension with $St = 0.1$, $Pe = 10$, $\phi = 0.01$ and $\alpha = 20$. Statistics performed over 50 realizations.

frequency of aggregates in the suspension. Fig. (37) shows that the number of aggregates in the suspension is indeed enhanced when the effect of dipolar interactions is stronger. Fig. (37b) shows that aggregates of 4 particles may be found in the suspension microstructure for $\lambda = 80$. Furthermore, the fraction of dimers is increased from 5% to 15% when the dipolar interaction is increased from $\lambda = 20$ to $\lambda = 80$. Fig. (38) shows that this increase in dipolar interactions also disrupts the magnetization values that would otherwise be attained due to the action of the external field. In thermal equilibrium and in the absence of dipolar or hydrodynamic interactions, the magnetization would be equal to its Langevin value at that field, of approximately 1. That is, the dipole moments would be aligned with the magnetic field, on average. We argue that the loss of magnetization with the increasing of dipolar interactions results from the increase in the number of larger chains.

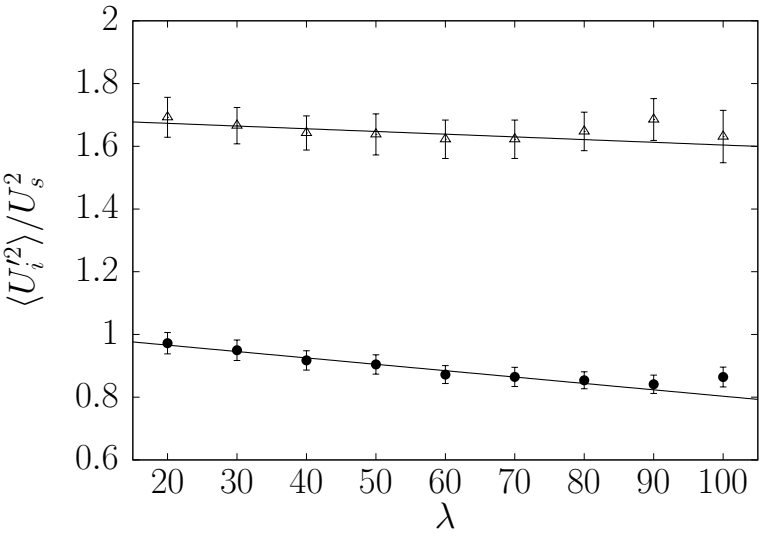

Figure 35 – Non-dimensional variance of velocity fluctuations perpendicular (•) and parallel (△) to gravity, as a function of the dipolar interaction parameter. Simulation performed over 50 realizations with $St = 0.1$, $Pe = 10$, $\phi = 0.01$ and $\alpha = 20$. Linear fits: $\langle U_\parallel'^2 \rangle = 1.72 \pm 0.01 - (0.017 \pm 0.002)\lambda$, $\langle U_\perp'^2 \rangle = 0.99 \pm 0.02 - (0.014 \pm 0.002)\lambda$.

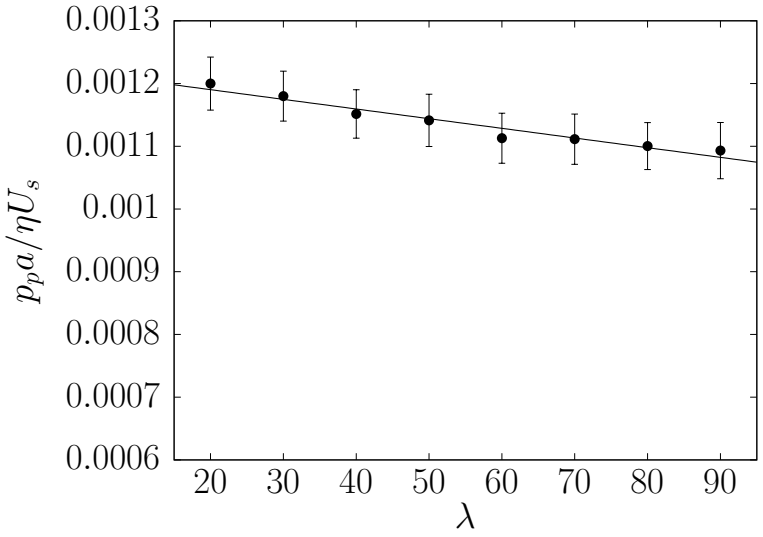

Figure 36 – Non-dimensional particle pressure of a monodisperse magnetic low Reynolds number suspension with $St = 0.1$, $Pe = 10$, $\phi = 0.01$ and $\alpha = 20$. Simulations performed over 50 realizations. Linear fit: $p_p a/\eta U_s = [122 \pm 1 - (0.2 \pm 0.01)\lambda] \times 10^{-5}$.

This induces cluster-particle and cluster-cluster magnetic interactions, causing an increase in the velocity fluctuations over isolated particles and diffusion of orientations, in some cases even permitting the formation of chains aligned opposed to the field.

The structure factor as a function of the wavenumber is presented in Figs. (39) and (40) for different times and dipolar interaction parameters. It measures the correlation between density numbers as a function of the reciprocal wavelength. From a physical point of view, the structure factor gives the fluctuation in the number of particles at different length scales of the numerical box. We can see that at the initial configuration, the ran-

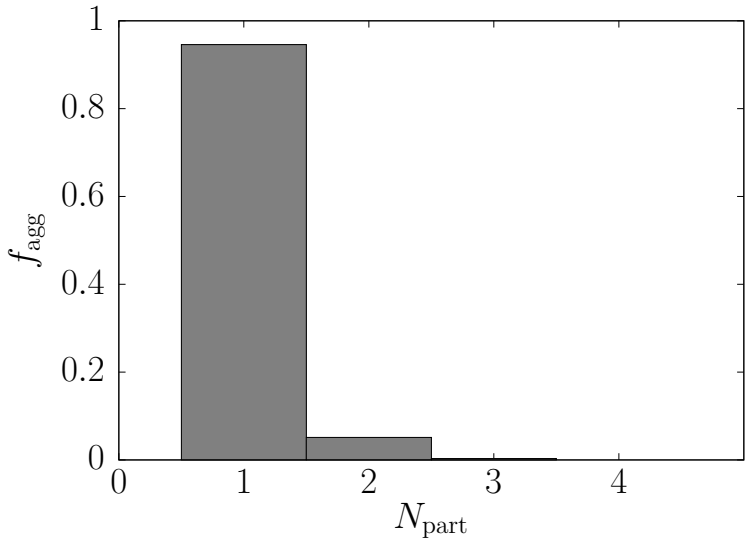

(a) $\lambda = 20$.

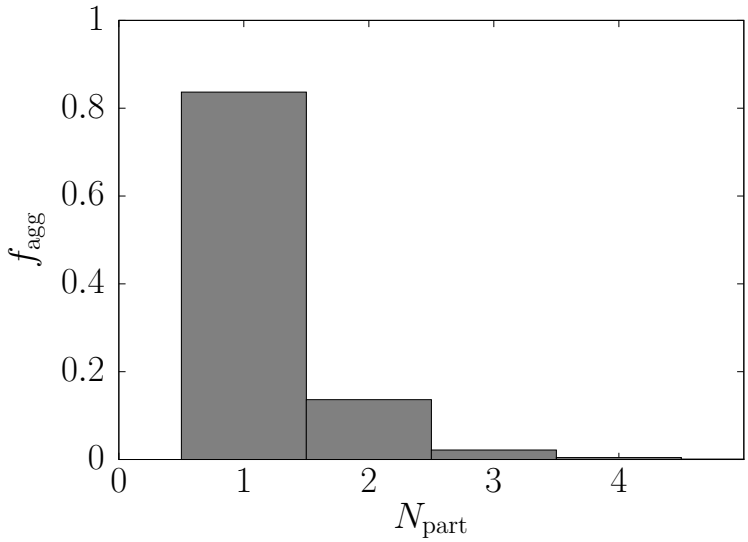

(b) $\lambda = 80$.

Figure 37 – Histogram with the relative frequency of number of particles per aggregate. Simulation performed over 50 realizations with $St = 0.1$, $Pe = 10$, $\alpha = 20$ and $\phi = 0.01$.

dom dispersion presents a structure factor which oscillates around its thermal equilibrium value[2] of 1 in both directions. However, horizontal and vertical structure factors behave differently as time evolves. The structure factor parallel to the field develops a broad maximum band close to a reciprocal wavelength of 0.5 (i.e., a wavelength of 2), indicating that aggregates of two particles become more likely to be found. In contrast, the structure factor orthogonal to the field has its peaks shifted to lower reciprocal wavelengths, corresponding to greater separation of particles along horizontal directions. We attribute both of these behaviors to dipolar interactions, since particles with dipole moments aligned with the field have attractive interactions when their distance vectors are aligned to the field and repulsive interactions when these vectors are orthogonal to the field. In fact, we see the aforementioned effects are even more remarked when dipolar interactions are in-

[2] See Mattis (2004) or Dhont (1996) for a proof of the equilibrium value of the structure factor.

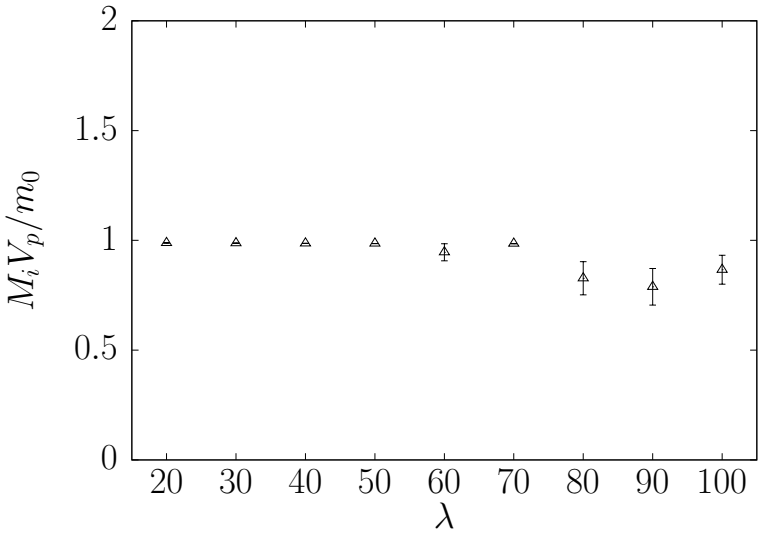

Figure 38 – Non-dimensional magnetization perpendicular (•) and parallel (△) to gravity as a function of the dipolar interaction parameter. Simulation performed over 50 realizations with $St = 0.1$, $Pe = 10$, $\phi = 0.01$ and $\alpha = 100$.

creased. Since $S(\boldsymbol{k}) \sim \langle n'^2(\boldsymbol{k})\rangle$, we also argue that the increase of the horizontal structure factor over all wavelengths indicates an increase of convective currents in the xy plane with time, with highest values on $ak_x/2\pi = 0.4$. On the other hand, these convective currents are apparently hindered in the z plane, except near $ak_z/2\pi = 0.4$.

The velocity fluctuations autocorrelation in the direction of gravity intriguingly rises for a time of $\tau U_s/a = 5$, after nearly being nullified, as displayed in Fig. (41) and in contrast to the non-magnetic case. This behavior may also be attributed to the formation of chain-like structures in the suspension, which restrain motions orthogonal to the field, in this way binding fluctuations parallel to the field. Consequently, the time integral of these autocorrelations diverges and does not define a diffusive process. It should also be noted that this observed behavior of a non-zero correlation function at long times is closely related to the formation of chains, also indicated by the structure factor. In fact, it may be a consequence to the characteristic time of this formation, as is also seen in the progressive evolution of the structure factor shown in Figs. (39) and (40). The integral of velocity autocorrelations shown in Fig. (42) diverges because of the positiveness attained by the autocorrelation at long times.

A curious result can be seen as the dipolar interactions exceed a certain critical value. For instance, from $\lambda = 90$ on, the values of velocity fluctuation autocorrelations function in the direction of gravity are also drastically attenuated, causing a sharp decrease of the diffusivity[3] parallel to gravity, along with the anisotropy between diffusion coefficients, as seen in Fig. (43). We argue that the sharp decrease in the diffusivity parallel to gravity marks the change from a regime dominated by hydrodynamic interactions to another dominated by dipolar interactions. In this way, the dominant physical mechanism

[3] Even though the integral of the velocity autocorrelations does not appear to converge as time goes to infinity, we present its partial value as integrated until the end of the simulations.

becomes aggregative instead of dispersive, such that a drop in the diffusivity results. In this process, the anisotropy in the diffusivities goes from $D_{\parallel}/D_{\perp} \sim 25$ to $D_{\parallel}/D_{\perp} \sim 3$.

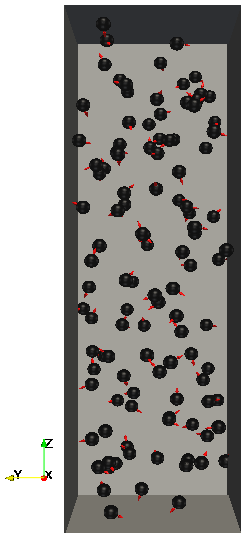

(a) Box at $\tilde{t} = 0$.

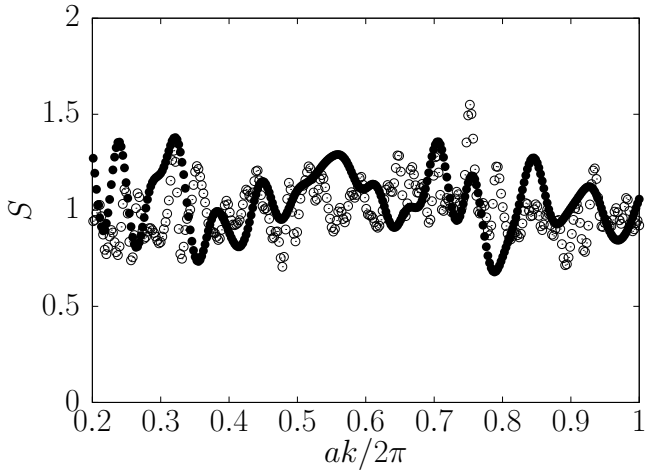

(b) $\alpha = 20$ at $\tilde{t} = 0$.

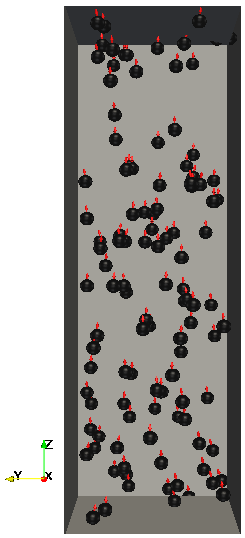

(c) Box at $\tilde{t} = 5$.

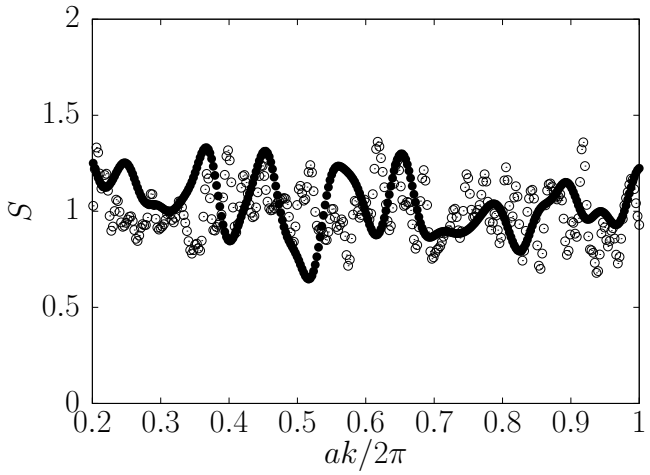

(d) $\alpha = 20$ at $\tilde{t} = 5$.

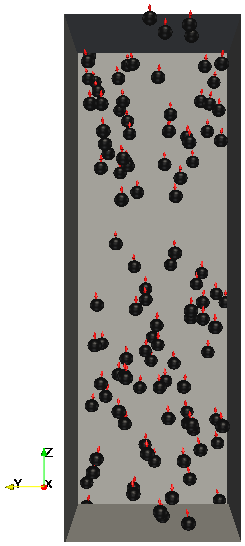

(e) Box at $\tilde{t} = 10$.

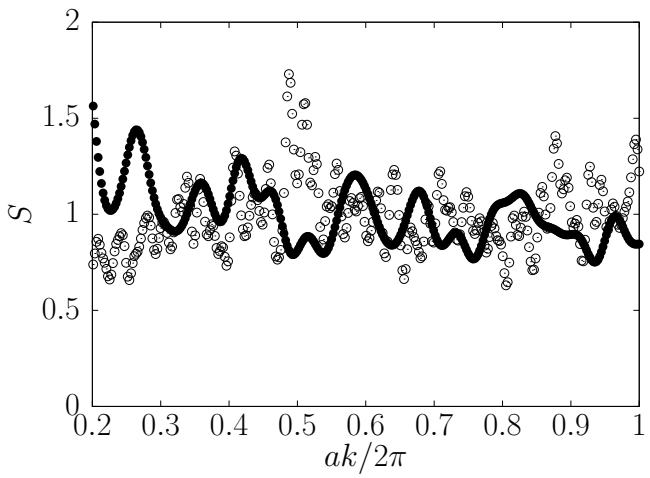

(f) $\alpha = 20$ at $\tilde{t} = 10$.

Figure 39 – Structure factors perpendicular (•) and parallel (○) to gravity at different times. Simulation carried out for $St = 0.1$, $Pe = 10$, $\alpha = 20$, $\lambda = 20$ and $\phi = 0.01$.

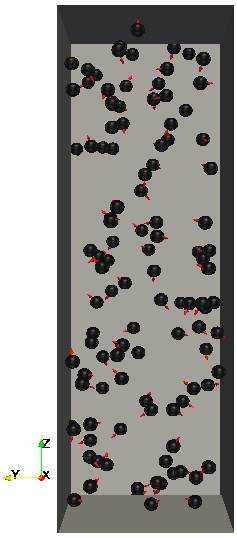

(a) Box at $\tilde{t} = 0$.

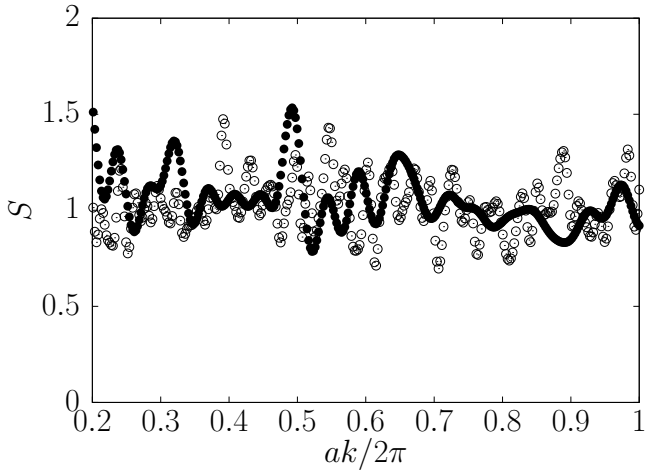

(b) $\alpha = 10$ at $\tilde{t} = 0$.

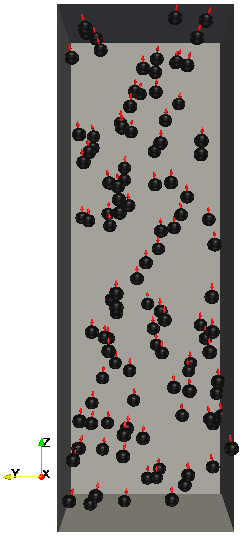

(c) Box at $\tilde{t} = 5$.

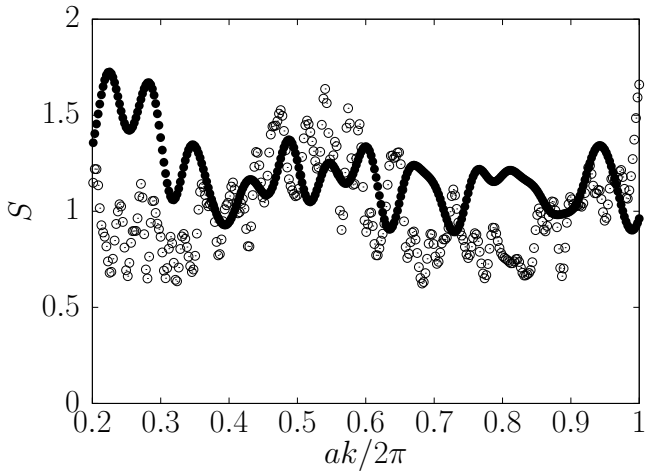

(d) $\alpha = 10$ at $\tilde{t} = 5$.

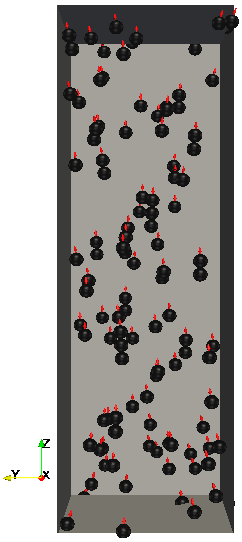

(e) Box at $\tilde{t} = 10$.

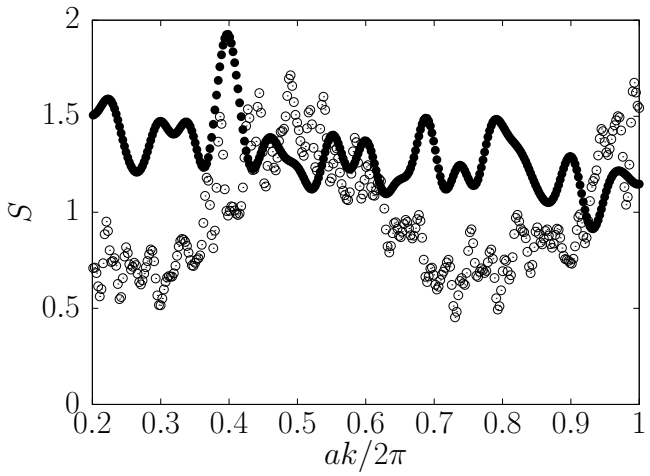

(f) $\alpha = 10$ at $\tilde{t} = 10$.

Figure 40 – Structure factors perpendicular (•) and parallel (○) to gravity at different times. Simulation carried out for $St = 0.1$, $Pe = 10$, $\alpha = 20$, $\lambda = 80$ and $\phi = 0.01$.

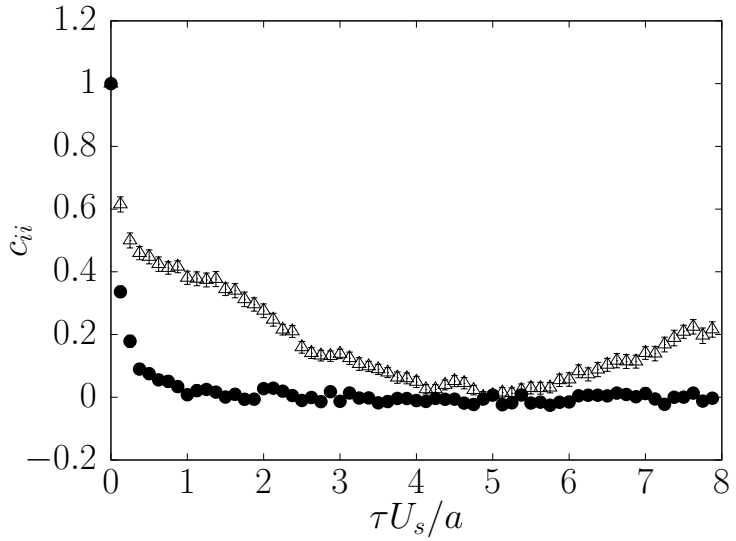

(a) $\lambda = 20$.

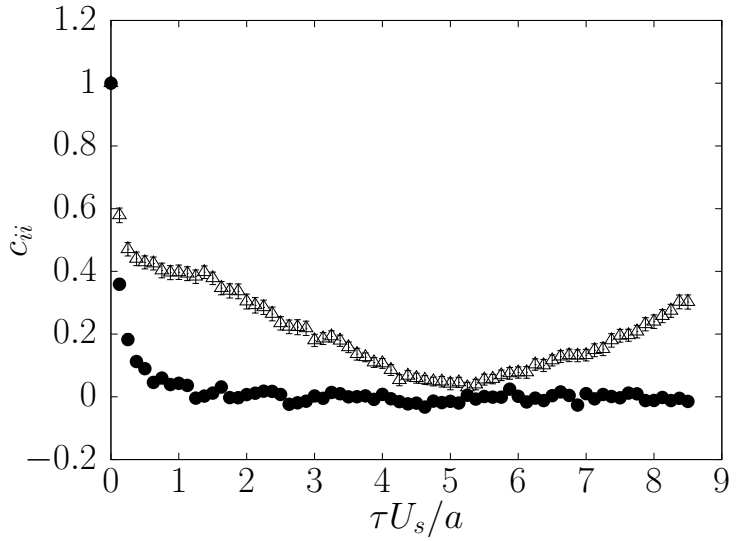

(b) $\lambda = 80$.

Figure 41 – Normalized autocorrelation of velocity fluctuations perpendicular (•) and parallel (△) to gravity for a magnetic monodisperse low Reynolds number suspension with $St = 0.1$, $Pe = 10$, $\phi = 0.01$ and $\alpha = 20$.

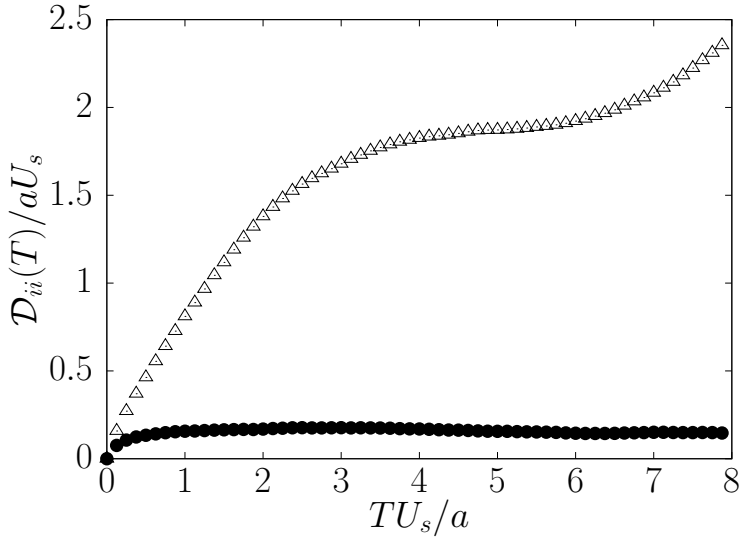

(a) $\lambda = 20$.

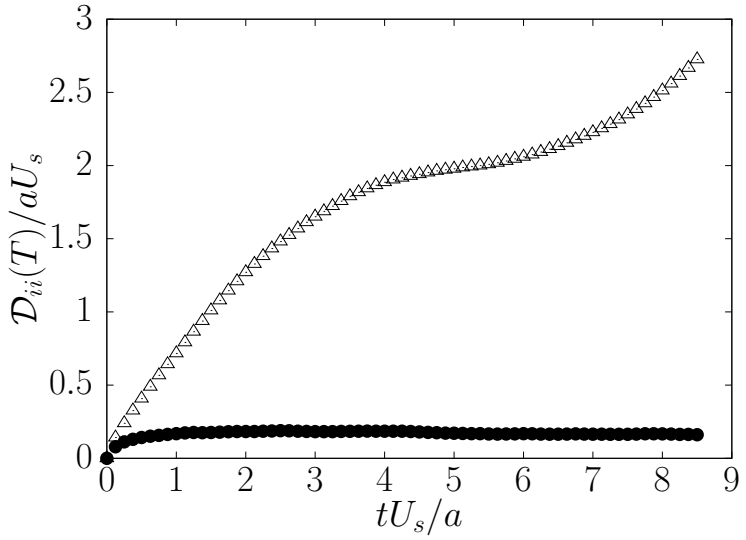

(b) $\lambda = 80$.

Figure 42 – Non-dimensional integral of velocity fluctuations autocorrelation perpendicular (•) and parallel (△) to gravity as a function of the time of integration. Simulation performed for $St = 0.1$, $Pe = 10$, $\alpha = 20$ and $\phi = 0.01$. Statistics performed over 50 realizations.

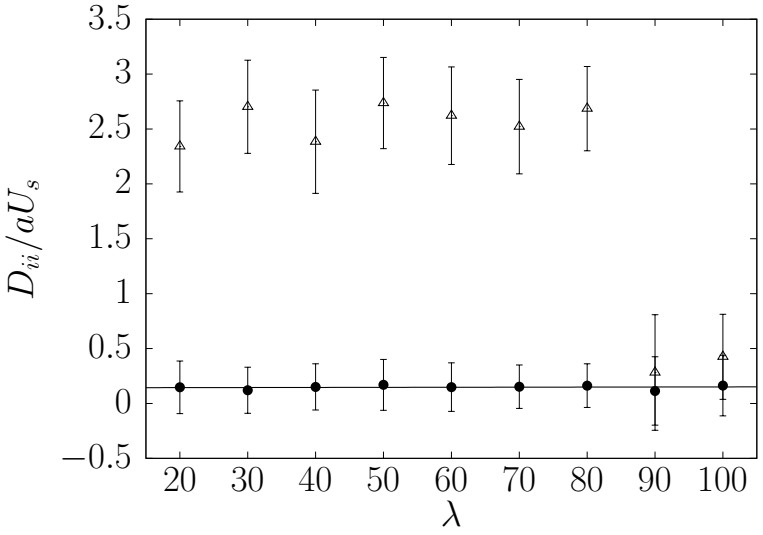

Figure 43 – Non-dimensional diffusion perpendicular (•) and parallel (△) to gravity in a monodisperse magnetic low Reynolds number suspension with $St = 0.1$, $Pe = 10$, $\phi = 0.01$ and $\alpha = 20$. Statistics performed over 50 realizations.

5.2.2 External Field

Now we keep the dipolar interactions parameter fixed at $\lambda = 100$ and vary the intensity of the external magnetic field, applied in the opposite direction to gravity. The time evolution of the velocity fluctuations is plotted in Fig. (44), where both time series do not present a clearcut distinction. At a higher field, Fig. (44b), it is seen that in early stages of the motion the velocity fluctuations in the gravity direction appear to be mildly hindered, whereas they grow towards the end of the simulation. We argue that this could be due to the formation of larger chains of particles, which induce large velocity fluctuations over single particles. This is reasonable assumption, since this structure formation is observed to take times comparable to the total time of simulation. Furthermore, larger applied fields orient the particles quicker along its lines, favoring faster structure formation and permitting the observation of such velocity fluctuations peaks, as seen is Fig. (44b). Indeed, at low applied fields and elevated values of dipolar interactions, there is a competition for orientation induced by the external field and that promoted by the dipolar interactions. In fact, we see from Fig. (45) that the magnetization for the range $\alpha \in (0, 20)$ is much lower than its thermodynamic equilibrium value (see Appendix A), however for magnetic fields close to $\alpha = 20$ it begins to saturate to values close to unity.

Fig. (46) depicts the dependence of the velocity fluctuations time average on the external field. A slight decrease in the velocity fluctuations is observed when α is increased from 0 to 20 but saturates from this value onward. We argue that this reflects the distinct roles of the external field and the dipolar interactions. While the latter are responsible for the attractive forces that lead to aggregation, their increase signifying a direct change in the configuration and properties of the suspension, the former is associated to the orientation of the dipole moments along the field. Thus, after a critical value of the external field, the dipoles are already aligned along the field and aggregation befalls by the action of dipolar interactions. Further increases in the field do not contribute any more. This is an inductor-atractor scenario, where the field acts as an inductor, promoting proper conditions for the action of the atractor, the dipolar forces. Analogously, the particle pressure is presented in Fig. (47). We also see that it is insensitive to the magnetic field intensity, except perhaps in the interval $\alpha \in (0, 20)$. A more detailed investigation of this interval of magnetic fields is in order.

Histograms of number of particles per aggregate are presented in Fig. (48) for the two different fields intensities. The distribution remains approximately unchanged, with only a feeble increase in dimer frequency, in consonance with our description of the field action.

The structure factor time evolution is presented in Figs. (49) and (50). The remarks made about Fig. (40) for the high dipolar interaction regime, which still hold. An interesting difference to be observed is that, in the particular realization depicted in Fig. (49), the particles orient on average in the direction opposite to the field. It shows that

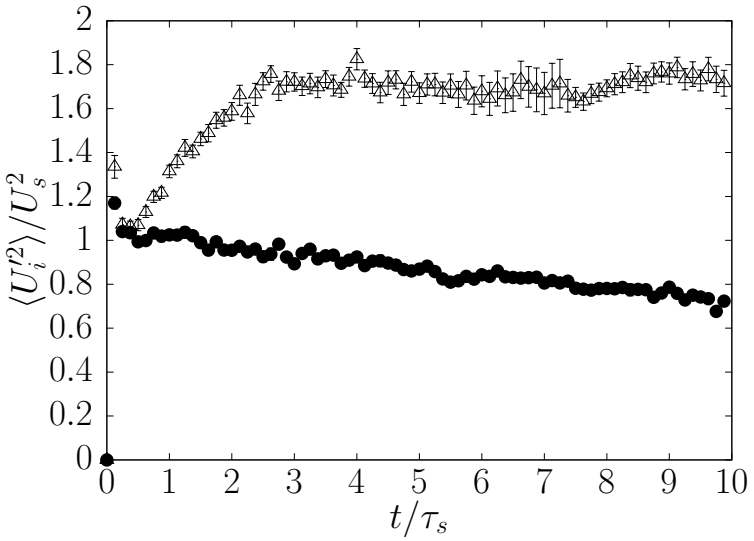

(a) $\alpha = 10$.

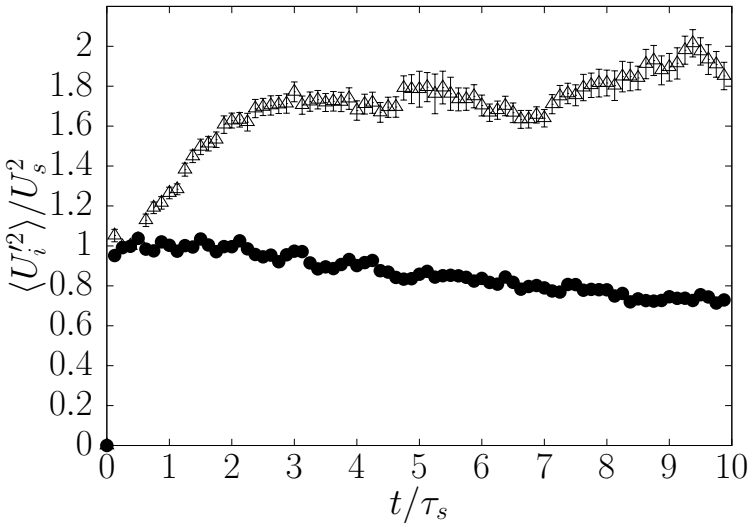

(b) $\alpha = 100$.

Figure 44 – Non-dimensional variance of the velocity fluctuations perpendicular (•) and parallel (△) to gravity for a monodisperse magnetic low Reynolds number suspension with $St = 0.1$, $Pe = 10$, $\phi = 0.01$ and $\lambda = 100$. Statistics performed over 50 realizations.

the orientational action of dipolar forces dominates that of the external field in this particular instance, contributing to the low magnetization value found in Fig. (45). We also see from Fig. (49) that the horizontal (in the xy plane) structure factor peaks shift to lower wavelengths along time at low applied fields. This result could indicate a repulsive character of the dipolar interactions in this regime of low magnetic fields, perhaps as a consequence of unaligned orientations of chains of particles. In contrast, Fig. (50) shows that the horizontal structure factor average on the wavenumbers rises in a roughly homogeneous fashion. This could point out to an attractive effect of dipolar interactions, such that chain formation is still in progress, giving rise to convective currents in the field associated to low lengthscale number density fluctuations $\sqrt{n_{k_x}'^2} \sim \sqrt{\langle |n(k_x)|^2 \rangle}$.

The breaking in autocorrelation anisotropy indirectly noted in Fig. (43) is observed

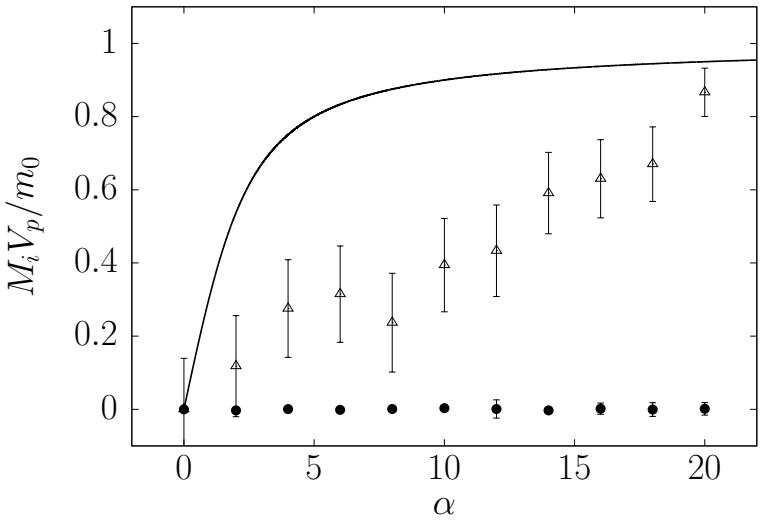

Figure 45 – Non-dimensional magnetization perpendicular (•) and parallel (△) to gravity as a function of the external field parameter. Simulations performed over 50 realizations with $St = 0.1$, $Pe = 10$, $\phi = 0.01$ and $\lambda = 100$. Langevin function represented by a continuous line (—).

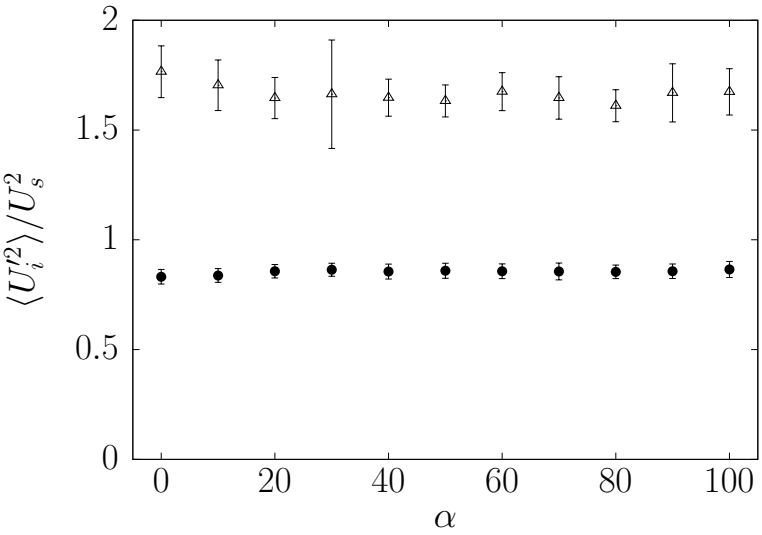

Figure 46 – Non-dimensional variance of velocity fluctuations perpendicular (•) and parallel (△) to gravity as a function of the external field parameter. Simulation performed over 50 realizations with $St = 0.1$, $Pe = 10$, $\phi = 0.01$ and $\lambda = 100$.

again in Fig. (51b). It is seen that the complex effects of the interplay of external field and dipolar interactions leads to recorrelation, as in Fig. (51a), as well as to mitigation of velocity fluctuation correlations, as in Fig. (51b). In a tentative explanation for these apparently contradictory phenomena, we claim that the suppression of velocity fluctuations autocorrelation in the direction of gravity might occur due to an overshooting instability in the orientation of the particles produced by strong fields. In fact, hydrodynamic torque interactions couple the rotational and translational motion of all the particles, possibly transmitting the short-time orientation fluctuations induced by the field as alternating velocity fluctuations to the particles, damping the memory inserted by gravity. Nevertheless, at long times the effect of recorrelation introduced by the dipolar interactions persists

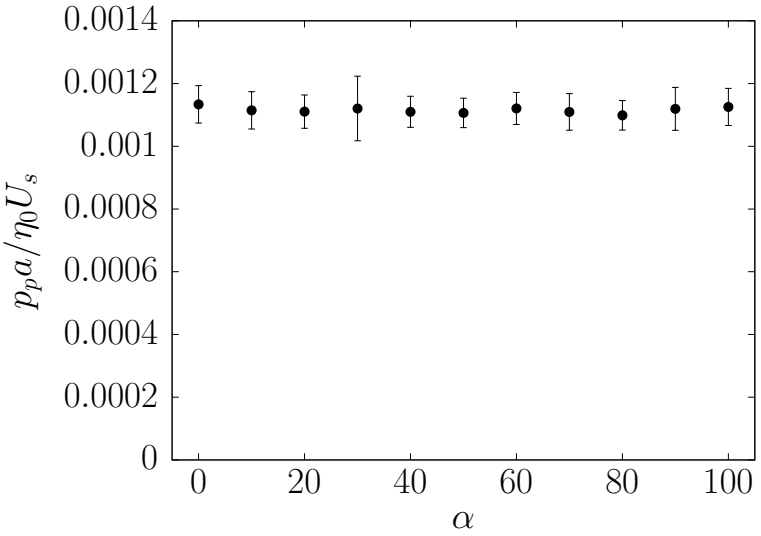

Figure 47 – Non-dimensional particle-phase pressure as a function of the external field parameter. Simulation performed over 50 realizations with $St = 0.1$, $Pe = 10$, $\phi = 0.01$ and $\lambda = 100$.

even in high magnetic fields, albeit faded. Indeed, the velocity fluctuation correlations in the direction of gravity continue to be greater than the ones orthogonal to it, as seen by their time integral presented in Fig. (52). We attribute this behavior to the formation of chains of particles, whose fluctuations are bound by the magnetic link between them. The additional inertia of the chain, compared to a single particle, inserts additional memory and ties the fluctuation at a given time to that of a later time.

The inset in Fig. (52) amplifies the integral of velocity fluctuation correlations perpendicular to gravity. In contrast to their parallel counterpart, they do not appear to increase continuously over time. Thus, these correlations orthogonal to gravity seem to define a diffusive Markovian process along this direction, the influence of gravity and the magnetic field over it being less appreciable than along the parallel direction. We see that though the correlation appears to oscillate around zero resulting in a decay of their integral at short times, this integral appears to converge at long times, actually characterizing a diffusive process with a well defined diffusion coefficient.

Similarly to Fig. (43), Fig. (53) illustrates the drastic suppression of the diffusion along the direction of gravity caused by the dipolar interactions. Furthermore, it sets an approximate threshold of $\alpha = 20$ for the occurrence of this phenomenon.

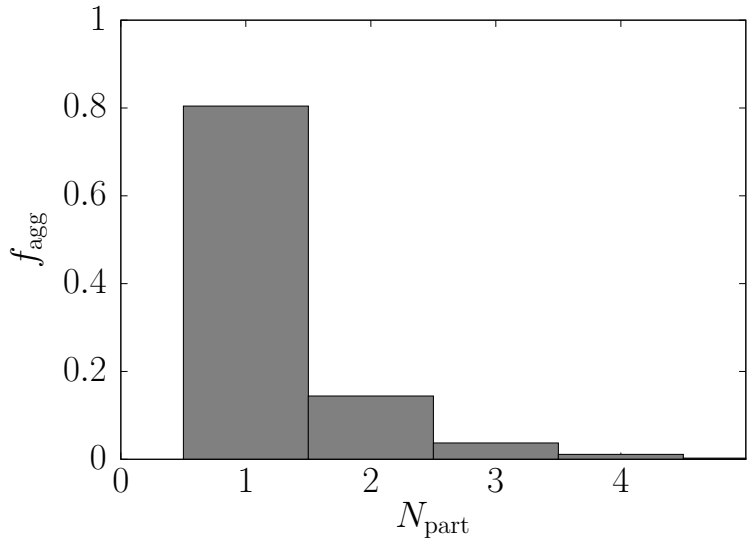

(a) $\alpha = 10$.

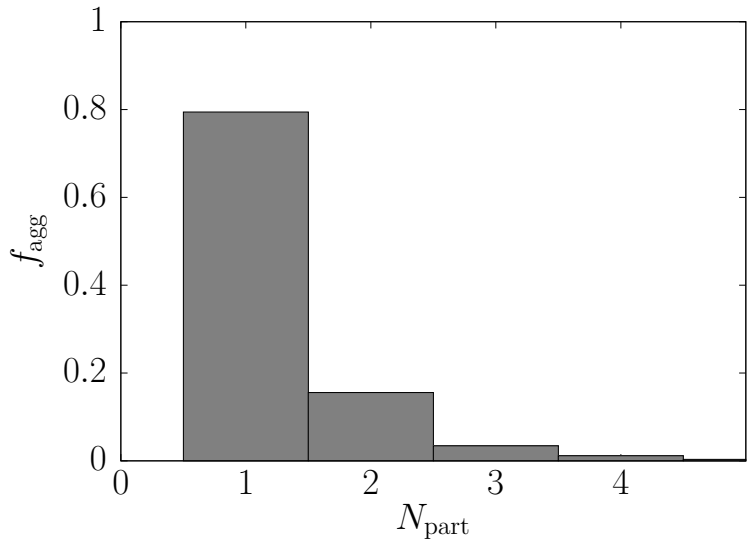

(b) $\alpha = 100$.

Figure 48 – Histogram of the relative frequency of number of particles per aggregate. Simulation carried out with $St = 0.1$, $Pe = 10$, $\lambda = 100$ and $\phi = 0.01$.

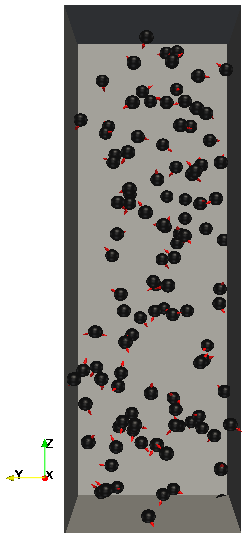

(a) Box at $\tilde{t} = 0$.

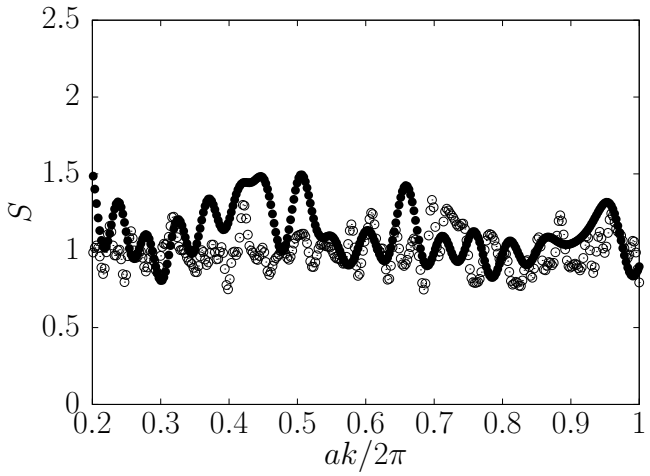

(b) $\alpha = 10$ at $\tilde{t} = 0$.

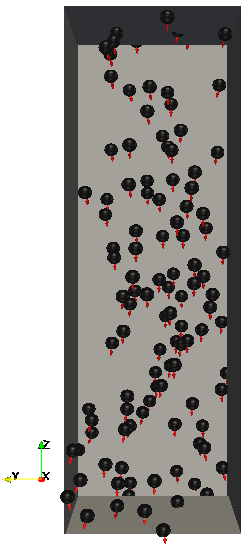

(c) Box at $\tilde{t} = 5$.

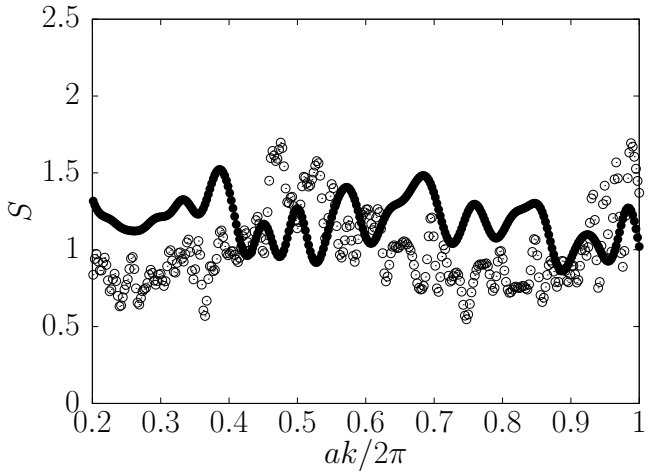

(d) $\alpha = 10$ at $\tilde{t} = 5$.

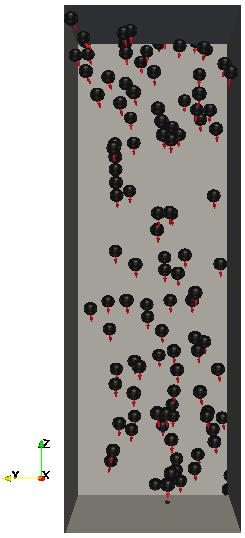

(e) Box at $\tilde{t} = 10$.

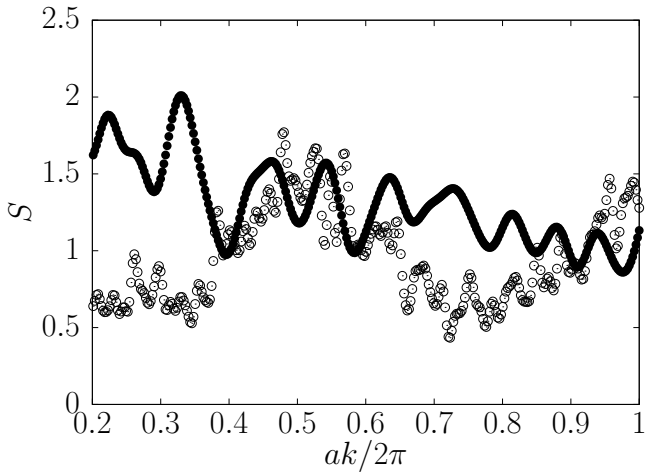

(f) $\alpha = 10$ at $\tilde{t} = 10$.

Figure 49 – Structure factors perpendicular (•) and parallel (○) to gravity at different times. Simulation carried out for $St = 0.1$, $Pe = 10$, $\alpha = 10$, $\lambda = 100$ and $\phi = 0.01$.

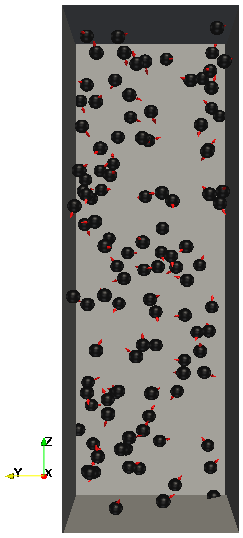

(a) Box at $\tilde{t} = 0$.

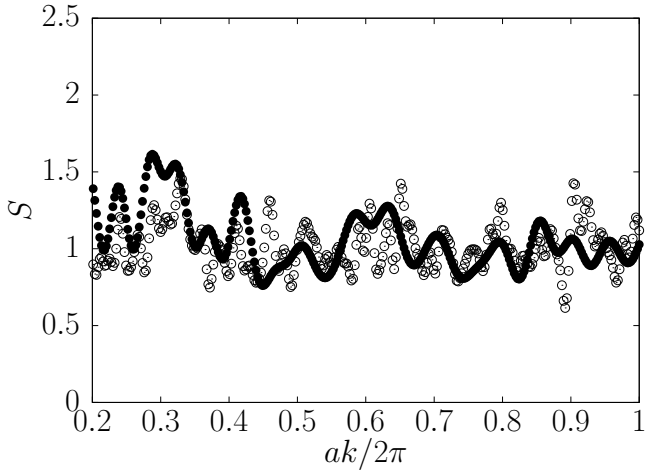

(b) $\alpha = 10$ at $\tilde{t} = 0$.

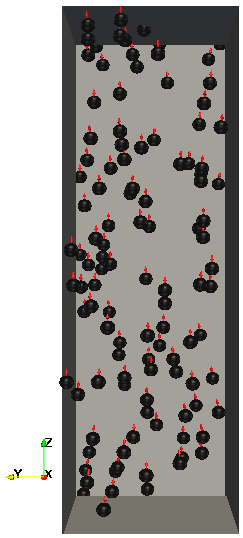

(c) Box at $\tilde{t} = 5$.

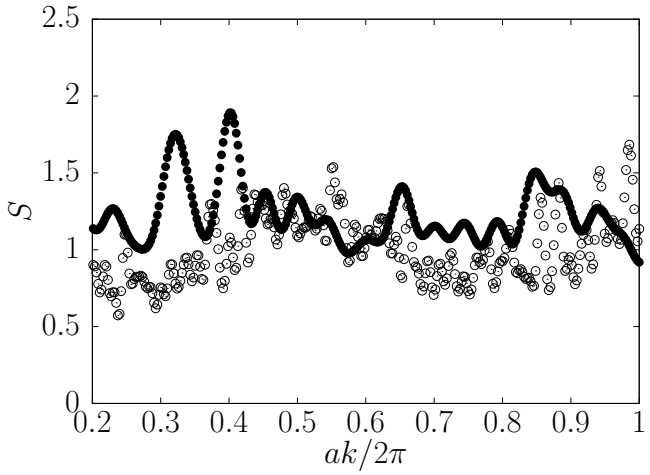

(d) $\alpha = 10$ at $\tilde{t} = 5$.

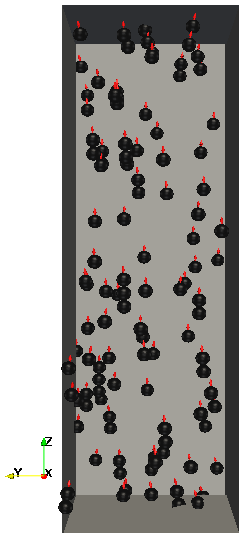

(e) Box at $\tilde{t} = 10$.

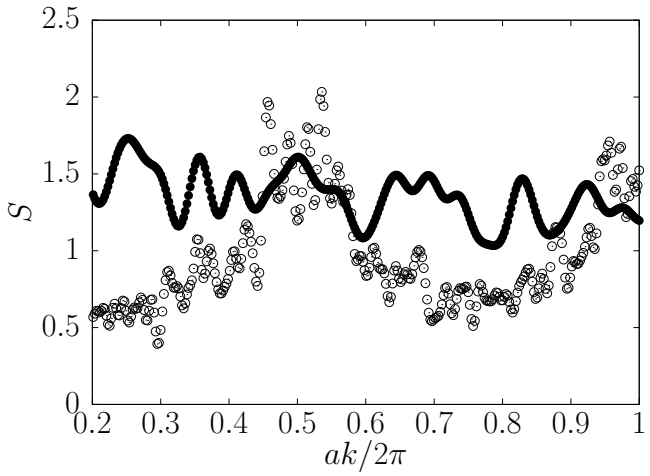

(f) $\alpha = 10$ at $\tilde{t} = 10$.

Figure 50 – Structure factors perpendicular (•) and parallel (○) to gravity at different times. Simulation carried out for $St = 0.1$, $Pe = 10$, $\alpha = 100$, $\lambda = 100$ and $\phi = 0.01$.

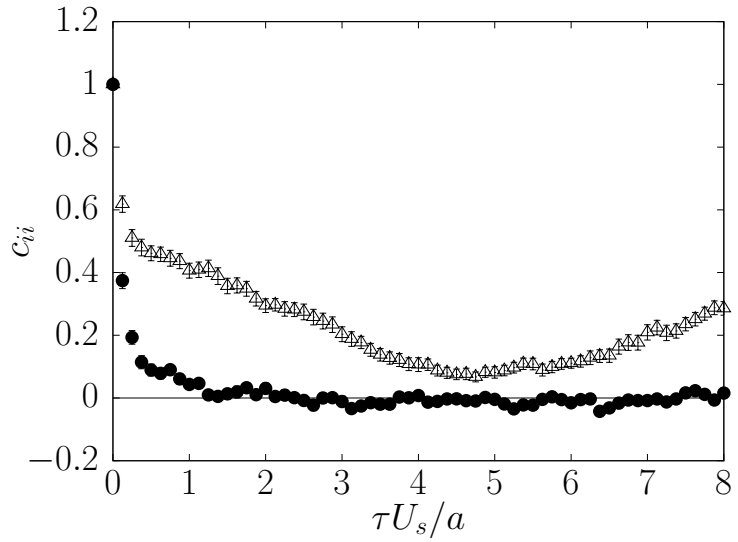

(a) $\alpha = 10$.

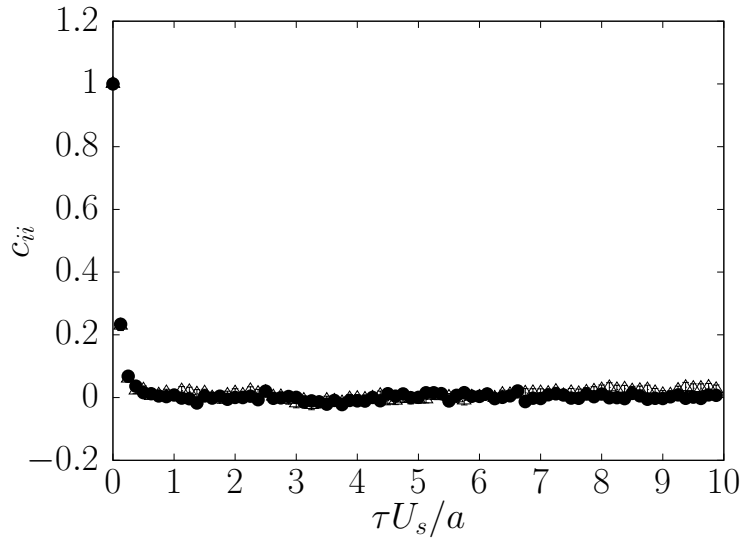

(b) $\alpha = 100$.

Figure 51 – Normalized autocorrelation of velocity fluctuations perpendicular (•) and parallel (△) to gravity for a magnetic monodisperse low Reynolds number suspension with $St = 0.1$, $Pe = 10$, $\phi = 0.01$ and $\lambda = 100$. The zero value is highlighted by a continuous line.

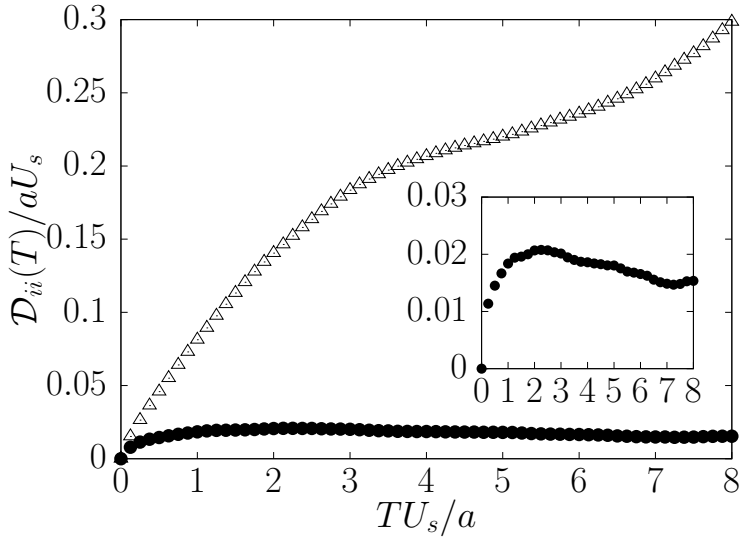

(a) $\alpha = 10$.

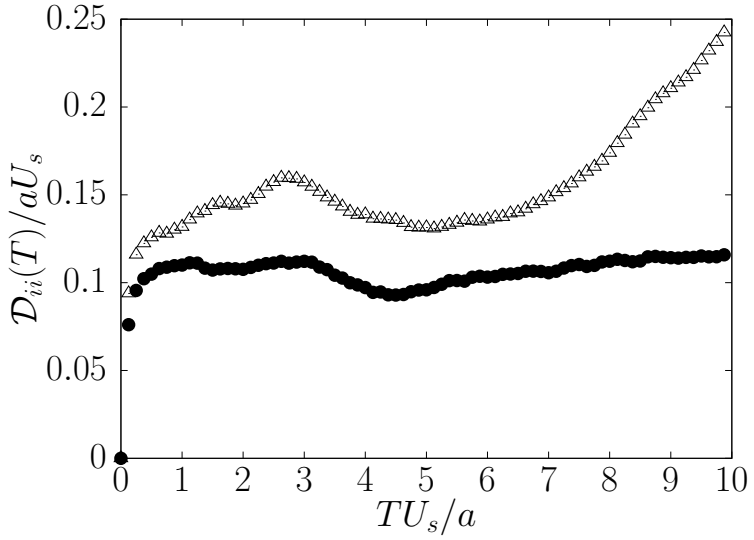

(b) $\alpha = 100$.

Figure 52 – Non-dimensional integral of velocity fluctuations autocorrelation perpendicular (•) and parallel (△) to gravity as a function of the time of integration. Simulation carried out for $St = 0.1$, $Pe = 10$, $\lambda = 100$ and $\phi = 0.01$. The inset amplifies the autocorrelation integral perpendicular to gravity.

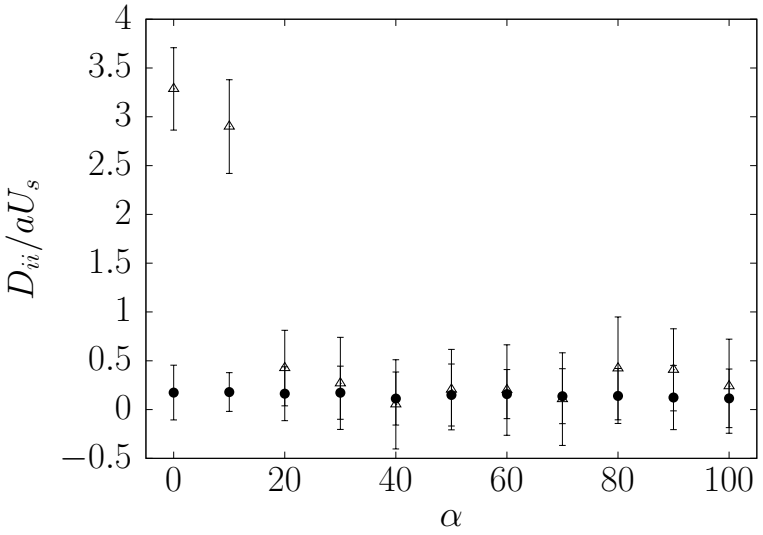

Figure 53 – Non-dimensional diffusion perpendicular (•) and parallel (△) to gravity in a monodisperse magnetic low Reynolds number suspension with $St = 0.1$, $Pe = 10$, $\phi = 0.01$ and $\lambda = 100$. Statistics performed over 50 realizations.

6 Applications of Magnetic Suspensions

6.1 Suspension Stability

In this chapter, we address a few characteristics of magnetic suspensions with a view to selected potential applications. The first one we consider is the stability of a magnetic suspension, more specifically how the thickness of the surfactant layer impacts the stability of the suspension. This layer is added to prevent aggregation and flocculation of magnetic particles, which depletes the suspension and reverts its properties back to those of the carrier fluid. In Fig. (55), we examine how the layer thickness affects the average velocity of the suspension. We stress that this is a qualitative study, since it does not renormalize the hydrodynamic interactions by Ewald sums of the mobility tensors (BEENAKKER, 1986). We choose to avoid this renormalization because our interest lies in the scaling of the average velocity dependence on δ_s, rather than its actual values. Furthermore, our study is restrained to dilute suspensions, where these interactions occur at high distances, on average. The decay of these hydrodynamic interaction forces and torques makes the renormalization correction less important. The addition of Ewald sums would elevate the computational cost of the simulations, which is already high, especially the resistance formulation employed. As expected, we find out that the average velocity of the suspension presents a strong dependence with the layer thickness up until approximately $\delta_s = 0.2a$. Beyond this point, the formation of aggregates is strongly reduced and their average fall speed stabilizes as a consequence. Therefore, a layer thickness of $\delta_s = 0.2a$ would be appropriate for the application in question.

We also present the variance of velocity fluctuations as a function of the layer thickness, since it is a counter-intuitive result. As Fig. (55) shows, the variance of velocity fluctuations decays with the thickening of the layer. This would be unexpected since thinner layers permit the formation of longer chains, with increased inertia, which would respond less to applied forces and thus present lower velocity fluctuations. However, we may argue, just as in Sec. (5.2.1), that larger chains produce higher fluctuations over single particles, resulting in greater variances on average. Hence, this result would be in agreement with the conclusions drawn in Sec. (5.2.1). The same behavior reflects itself in

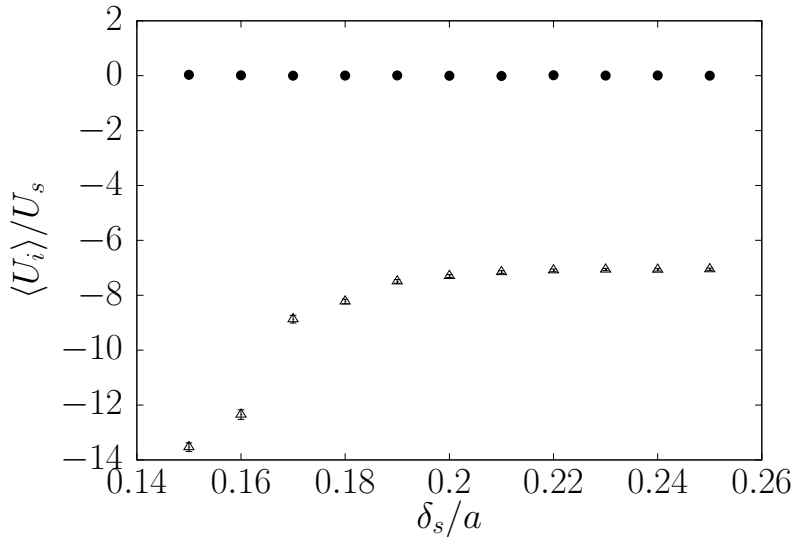

Figure 54 – Non-dimensional velocity average perpendicular (•) and parallel (△) to gravity as a function of the surfactant layer thickness. Simulation performed over 50 realizations with $St = 0.1$, $Pe = 10$, $\phi = 0.01$, $\alpha = 100$ and $\lambda = 100$.

the particle-phase pressure of the suspension, Fig. (56).

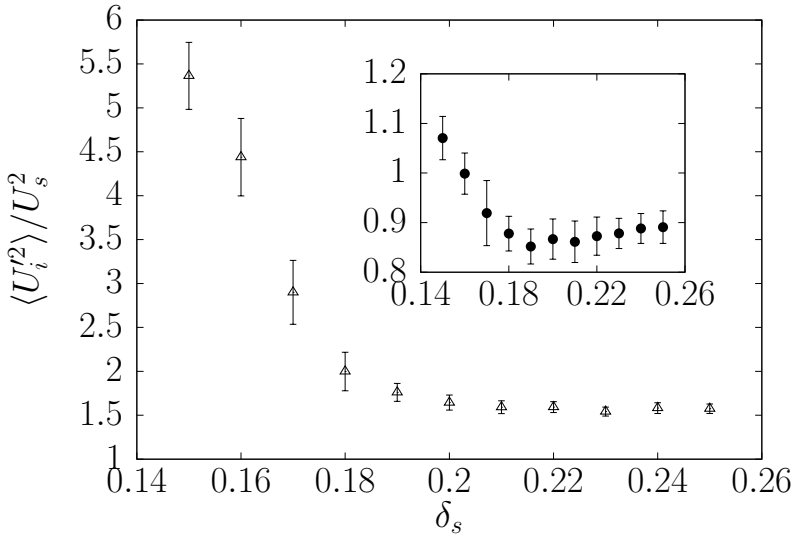

Figure 55 – Non-dimensional variance of velocity fluctuations perpendicular (•) and parallel (△) to gravity as a function of the surfactant layer thickness. Simulation performed over 50 realizations with $St = 0.1$, $Pe = 10$, $\phi = 0.01$, $\alpha = 100$ and $\lambda = 100$. The inset amplifies the variance of perpendicular velocity fluctuations.

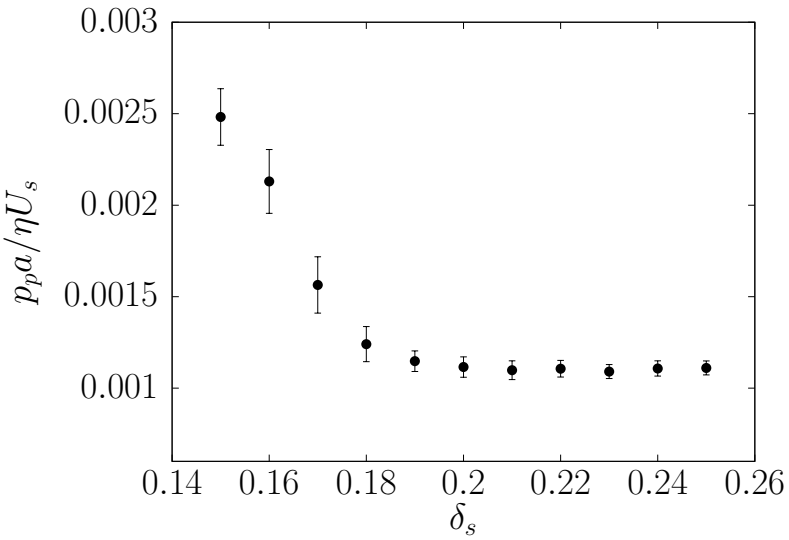

Figure 56 – Non-dimensional particle-phase pressure as a function of the surfactant layer thickness. Simulation performed over 50 realizations with $St = 0.1$, $Pe = 10$, $\phi = 0.01$ and $\lambda = 100$.

6.2 Magnetic Active Matter

Active matter, such as living fluids, has been the focus of extensive research done over the last few years due to the complex collective mechanisms which microorganisms display to generate propulsion in a viscous flow. A related topic that has risen an even more recent interest is that of magnetic active matter (PEYER; ZHANG; NELSON, 2013; KLAPP, 2016), i.e., magnetic particles immersed in a flow, which move under the action of an external magnetic field. Besides being able to emulate the behavior seen in biological suspensions, magnetic active matter presents advantages over the former, such as the simpler models that govern them and their controllability, enabling studies of their optimal propulsion.

We exemplify a possible application of the code developed in this work by simulating a prototype of magnetic active matter. We generate an initial condition where the particles are lined up in chains and submit them to the action of the magnetic field of a rectangular prism, given by Eqs. (2.167) to (2.178), which in addition moves a velocity of constant modulus and periodically changing sign. Fig. (57) illustrates that these so called magnetic snakes are displaced by the field and exhibit relative motion to one another, indicating the break of the symmetry and reversibility of creeping flows induced by interactions between magnetic dipoles or with the external field and also observed in the self-propelled motion of microorganisms.

This is an important example since our code is currently being used by a doctorate student in our group, Yves-Garnard Irilan, to further investigate these propulsion mechanisms in magnetic active matter. Besides the common framework of both studies, with the same equations of particle motion, some quantities are of interest in both works. In fact, a goal of his work is to investigate how these chains of particles interact and recombine over time, the structure factor and the histogram of number of particles per aggregate being fundamental quantities in this structural description.

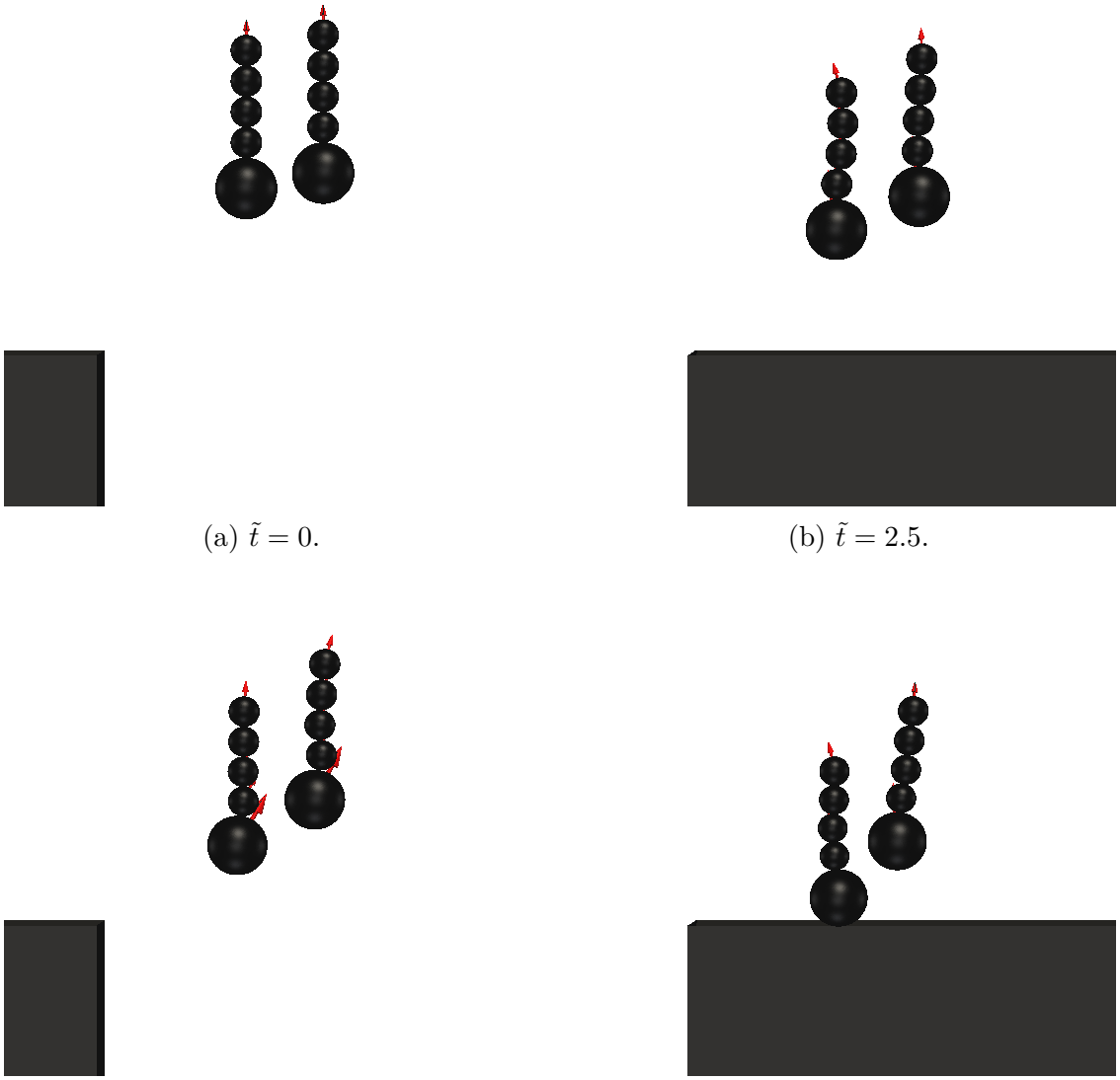

(a) $\tilde{t} = 0$.

(b) $\tilde{t} = 2.5$.

(c) $\tilde{t} = 5$.

(d) $\tilde{t} = 7.5$.

Figure 57 – Top view of the time evolution of the configuration of magnetic snakes subject to an external oscillatory magnetic field. Parameters of the simulation: $St = 0.01$, $Pe = 5$, $\alpha = 1000$ and $\lambda = 40$.

7 Conclusion

We developed a code in Fortran to determine short and long-time properties related to particle velocity fluctuations in magnetic gas-solid suspensions of interacting massive particles in sedimentation. We started our analysis by the case of Brownian motion of a non-magnetic isolated particle under the action of gravity, where we developed a numerical solution which was validated against a particular form of the analytic solution by Uhlenbeck and Ornstein (1930). Next, the numerical approach was extended to perform simulations of viscous magnetic suspensions at low Reynolds numbers in the presence of particle inertia and Brownian motion, with N particles interacting hydrodynamically. From the numerical simulations we have investigated the short and long-time behavior of the anisotropic particle velocity fluctuations (i.e. hydrodynamic fluctuations tensor) produced by hydrodynamic interactions in terms of particle velocity variance, autocorrelation functions and particle diffusivities as a function of time, the Stokes number and particle volume fraction.

The variances and particle diffusivities were found to be highly anisotropic, with velocity fluctuations in the gravity direction being stronger and correlated over longer times than in the horizontal direction. The velocity variance decreased with the increasing of the Stokes number at a high Péclet number. In the dilute regime simulated here, the vertical particle velocity variance was found to increase linearly with $\phi(PeSt)^{-1}$, whereas the particle diffusivity increased like ϕ/Pe. For $St = 0.1$ and a high Pe number (i.e. $Pe = 10$) the largest velocity variance (in the gravity direction) due the effect of hydrodynamic interactions was $110\phi k_{_B}T/m$ and the corresponding result for the particle diffusivity in the same direction was $130D_0\phi$. We also have evaluated from our computer simulation the particle-phase pressure associated with the velocity fluctuations induced by hydrodynamic interactions. The results suggested this particle pressure contribution for the same St and Pe to go like $40D_0\eta\phi^2/a^2$. In a dilute regime the particle pressure seems to be a stabilizing effect on the suspension. This occurs because the particle pressure in a dilute regime always increases with increasing the particle volume fraction ϕ as we have shown here. However, we can argue that in more concentrated suspensions, the particle pressure can decrease with increasing ϕ as a consequence of the increased viscous dissipation and the drastic decreased source of velocity fluctuations as one approaches the close-packed limit.

Afterwards, we turned to the characterization of velocity fluctuations in a magnetic

suspension. Given sufficiently strong external fields and dipolar interactions, we found that the particles orient their dipole moments along the field due to its action, such that the interactions promote formation of chain-like structures. These structures, with larger moments of inertia and rotation restrained by dipolar interactions inhibit the velocity fluctuations, and thus the particle-phase pressure, in the suspension. We found dipolar interaction corrections for the parallel velocity fluctuations as $-0.017\lambda/PeSt$, and for the particle-phase pressure as $-0.2 \times 10^{-5} D_0 \eta \lambda / a^2$. Indeed, the structural changes were found to be reflected in the aggregate histogram, with an enhanced relative frequency of dimers and trimers, and in the structure factor, in a peak of number density correlation at the wavelength corresponding to dimer formation, in the field direction. Nevertheless, we found out that for very strong dipolar interactions (i.e., $\lambda \geq 90$), the variance of velocity fluctuations are notably enhanced by the increasing of dipolar interactions. We claimed that this effect originates in the velocity fluctuations induced by magnetic action of clusters of 3 and 4 particles over the motion of single particles or other clusters. On the other hand, an investigation of the effect of field intensity increase revealed that it is associated with the characteristic time of particle orientation along its direction, which enables the action of the dipolar interactions. Thus, after a field intensity threshold, most of the particles are already oriented along its direction, so the magnetization is saturated and further increase does not significantly affect suspension properties, except when it is sufficiently high to produce an overshooting instability of dipole moment orientations at short-times. We assert that this could be the mechanism behind the verified suppression of the anisotropy of velocity fluctuation autocorrelations and diffusion coefficients after a critical external magnetic field intensity of about $\alpha = 10$.

In fact, the most remarkable distinctions observed between the magnetic and non-magnetic suspensions relate to the diffusion and microstructure. We have seen that the structure factor perpendicular to the field increases in all wavelengths in the presence of high dipolar interactions. This implies the increase of convective currents in the xy plane along time. We In contrast, fluctuations of number density in the direction of gravity were reduced, except near $ak_z/2\pi = 0.5$, associated to dimer formation.

The first appreciable difference of the velocity fluctuations with respect to the non-magnetic suspension is a continuous time decay of the velocity fluctuations perpendicular to the magnetic field (and thus to gravity), especially for high effects of magnetic field and dipolar interactions. This means a break of the statistical stationary character of the process. In a novel result, the autocorrelation of velocity fluctuations was observed to recorrelate at long times, enhancing the diffusivity in the direction of gravity. We also noticed that for high effects of magnetic fields and dipolar interactions, the correlation time in the direction of gravity is sharply decreased. This results in an attenuation of the diffusivity parallel to gravity. We argue that this owes to the dominance of dipolar interactions over hydrodynamic interactions, shifting the regime from diffusive to aggregative.

This work was limited to the study of particle velocity fluctuations in a dilute

gas-solid suspension. This is by no means a restriction of the simulations developed here, liquid-solid suspensions may be studied with the same code, with only a proper choice of physical parameters. In fact, our code is ideally suitable to explore more concentrated suspensions. Our studies have motivated the use of direct numerical simulations of particles to feed parameters of continuum models for multiphase particulate flows.

7.1 Future Work

The flexibility of the modeling used in this code could support diverse complementary works. There are multiple related topics of interest which could be explored with similar methods, such as the investigation of suspensions containing both magnetic and non-magnetic particles. Thence, one is able to quantify the dependence of the magnetic effects on the fraction of magnetic particles. This is important in industrial applications because it enables the determination of an ideal fraction of magnetic particles from the economic benefit-cost point of view, reducing the cost of the suspension while still achieving the desired control of its properties. Another application of this work is, as mentioned in Sec. (6.2), is the study of the control over a collective motion of assemblies of magnetic particles in a fluid, resembling microorganisms.

In addition, there are numerous ways to supplement our characterization of the magnetic suspension studied in this work. A principal direction among them is studying the effect of diameter size polydispersity over the response of the suspension. This is such an important consideration in view of the natural polydispersity which occurs in the production of magnetic particles, and some of its impact over the suspension dynamics arises from the proportionality of the dipole moment to the volume of the particles, which results in the fostering of magnetic forces produced by the largest particles. In fact, this is a simply feasible study under the formulation described in this work, which is already polydisperse. Effects of polydispersity over velocity fluctuations of non-magnetic suspensions have already been studied by Cunha et al. (2002), and a related study of the magnetic case would an extension of this work. Investigations of magnetic suspensions with higher concentrations ($\phi > 5\%$) is another natural direction for expansion of this work. Though the framework is essentially equal, we advise the renormalization of magnetic dipolar and hydrodynamic interactions by Ewald summing in this more concentrated suspensions.

Furthermore, it would be important to investigate the response of the suspension to a horizontal magnetic field (i.e., perpendicular to gravity). Its action could cause a larger suppression of velocity fluctuations, increasing the contrast in the dynamic behavior of magnetic and non-magnetic suspensions. In that case, it could be a more fitting configuration for commercial uses. This has been verified in the stabilization of magnetic fluidized beds, e.g. by Wang et al. (2013).

Our explanations of the physical mechanisms behind anisotropy suppression of the long-time transport coefficients can be put on a more solid ground with further tests. Suggestions for future work regarding this characterization include a closer investigation of the parameter interval over which the anisotropy is hindered, for example varying $\alpha \in (10, 30)$ for $\lambda = 100$, and likewise $\lambda \in (70, 90)$ for $\alpha = 20$. Also, examining the variance of particle orientation over time could shed some light upon the alleged mechanism of overshooting instability, its dependence on the external field and the time scales over which it occurs.

Lastly, this study prompts a more complete characterization of the recorrelation of velocity fluctuations at long times and its relation to dipolar interactions. It would be very interesting to quantify the time at which this recorrelation starts and compare it against scalings based on the characteristic time of structure formation.

The author would like to continue researching correlated topics to this dissertation in a PhD, possibly with Professor D. L. Koch at Cornell University.

Bibliography

ABADE, G. C. *Mecânica da Sedimentação de Partículas Esféricas Interagindo Hidrodinamicamente*. [S.l.]: Universidade de Brasília, 2005. Citado 2 vezes nas páginas xii and 59.

ABADE, G. C.; CUNHA, F. R. Computer simulation of particle aggregates during sedimentation. *Computer Methods in Applied Mechanics and Engineering*, Elsevier, v. 196, n. 45, p. 4597–4612, 2007. Citado 2 vezes nas páginas 16 and 51.

BATCHELOR, G. K. Sedimentation in a dilute dispersion of spheres. *Journal of Fluid Mechanics*, Cambridge Univ Press, v. 52, n. 02, p. 245–268, 1972. Citado na página 5.

BATCHELOR, G. K. Brownian diffusion of particles with hydrodynamic interaction. *Journal of Fluid Mechanics*, Cambridge University Press, v. 74, n. 1, p. 1–29, 1976. Citado 2 vezes nas páginas 5 and 69.

BATCHELOR, G. K. A new theory of the instability of a uniform fluidized bed. *Journal of Fluid Mechanics*, Cambridge Univ Press, v. 193, p. 75–110, 1988. Citado 2 vezes nas páginas 5 and 16.

BATCHELOR, G. K. *An introduction to fluid dynamics*. [S.l.]: Cambridge university press, 2000. Citado 5 vezes nas páginas xi, 8, 9, 10, and 13.

BATCHELOR, G. K.; GREEN, J. T. The determination of the bulk stress in a suspension of spherical particles to order c 2. *Journal of Fluid Mechanics*, Cambridge University Press, v. 56, n. 3, p. 401–427, 1972. Citado na página 1.

BEENAKKER, C. W. J. Ewald sum of the rotne-prager tensor. *The Journal of Chemical Physics*, AIP Publishing, v. 85, n. 3, p. 1581–1582, 1986. Citado na página 91.

BICA, I.; LIU, Y. D.; CHOI, H. J. Physical characteristics of magnetorheological suspensions and their applications. *Journal of Industrial and Engineering Chemistry*, Elsevier, v. 19, n. 2, p. 394–406, 2013. Citado 2 vezes nas páginas 2 and 3.

BOSSIS, G. et al. Kinetics aggregation of magnetic suspensions. *Physica A: Statistical Mechanics and its Applications*, Elsevier, v. 390, n. 14, p. 2655–2663, 2011. Citado na página 5.

BRADY, J. F.; BOSSIS, G. Stokesian dynamics. *Annual Review of Fluid Mechanics*, v. 20, p. 111–157, 1988. Citado na página 5.

CAFLISCH, R. E.; LUKE, J. H. C. Variance in the sedimentation speed of a suspension. *Physics of Fluids*, AIP Publishing, v. 28, n. 3, p. 759–760, 1985. Citado na página 5.

CHAPMAN, S.; COWLING, T. G. *The mathematical theory of non-uniform gases: an account of the kinetic theory of viscosity, thermal conduction and diffusion in gases*. [S.l.]: Cambridge university press, 1970. Citado na página 14.

CHHABRA, R. P.; SOARES, A. A.; FERREIRA, J. M. A numerical study of the accelerating motion of a dense rigid sphere in non-newtonian power law fluids. *The Canadian Journal of Chemical Engineering*, Wiley Online Library, v. 76, n. 6, p. 1051–1055, 1998. Citado na página 4.

CHIKAZUMI, S.; GRAHAM, C. D. *Physics of Ferromagnetism 2e*. [S.l.]: Oxford University Press on Demand, 2009. Citado na página 33.

CUNHA, F. R. On the fluctuations in a random suspension of sedimenting particles. *J. Braz. Soc. Mech. Sci.*, v. 19, n. 4, p. 474–495, 1997. Citado 4 vezes nas páginas 5, 16, 45, and 47.

CUNHA, F. R. *Turbulence, Fundamentals of the Hydrodynamics of Magnetic Fluids*. [S.l.]: EPTT, 2012. v. 8 (Book Chapter, in Portuguese). Citado 2 vezes nas páginas xi and 32.

CUNHA, F. R. et al. Modeling and direct simulation of velocity fluctuations and particle-velocity correlations in sedimentation. *Journal of Fluids Engineering*, American Society of Mechanical Engineers, v. 124, n. 4, p. 957–968, 2002. Citado 4 vezes nas páginas 5, 26, 69, and 98.

CUNHA, F. R.; HINCH, E. J. Shear-induced dispersion in a dilute suspension of rough spheres. *Journal of Fluid Mechanics*, Cambridge Univ Press, v. 309, p. 211–223, 1996. Citado na página 5.

CUNHA, F. R.; SOBRAL, Y. D.; GONTIJO, R. G. Stabilization of concentration waves in fluidized beds of magnetic particles. *Powder technology*, Elsevier, v. 241, p. 219–229, 2013. Citado na página 5.

CUNHA, F. R.; SOUSA, A. J.; HINCH, E. J. Numerical simulation of velocity fluctuations and dispersion of sedimentating particles. *Chemical Engineering Communications*, Taylor & Francis, v. 189, n. 8, p. 1105–1129, 2002. Citado na página 5.

DHONT, J. K. G. *An introduction to dynamics of colloids*. [S.l.]: Elsevier, 1996. v. 2. Citado 2 vezes nas páginas 59 and 73.

DURU, P. et al. Constitutive laws in liquid-fluidized beds. *Journal of Fluid Mechanics*, Cambridge Univ Press, v. 452, p. 371–404, 2002. Citado 2 vezes nas páginas 5 and 68.

EINSTEIN, A. *Investigations on the Theory of the Brownian Movement*. [S.l.]: Courier Corporation, 1956. Citado 3 vezes nas páginas 1, 4, and 44.

ERN, P. et al. Wake-induced oscillatory paths of bodies freely rising or falling in fluids. *Annual Review of Fluid Mechanics*, Annual Reviews, v. 44, p. 97–121, 2012. Citado na página 4.

FAXÉN, H. Der widerstand gegen die bewegung einer starren kugel in einer zahen flussigkeit, die zwischen zwei parallelen ebenen wanden eingeschlossen ist. *Arkiv Mat. Astron. Och. Fys.*, v. 18, n. 29, p. 1–52, 1924. Citado na página 22.

FERREIRA, J. M.; CHHABRA, R. P. Accelerating motion of a vertically falling sphere in incompressible newtonian media: an analytical solution. *Powder technology*, Elsevier, v. 97, n. 1, p. 6–15, 1998. Citado na página 4.

GONTIJO, R.; CUNHA, F. Dynamic numerical simulations of magnetically interacting suspensions in creeping flow. *Powder Technology*, Elsevier, v. 279, p. 146–165, 2015. Citado na página 5.

Gregory F. Maxwell. *Ferrofluid on glass, with a magnet underneath.* 2006. [Online; accessed September 17, 2019]. Disponível em: <https://en.wikipedia.org/wiki/Ferrofluid>. Citado 2 vezes nas páginas xi and 2.

GRIFFITHS, D. J. *Introduction to electrodynamics*. [S.l.]: AAPT, 2005. Citado 2 vezes nas páginas xi and 33.

GROOT, S. R. d.; SUTTORP, L. G. Foundations of electrodynamics. Noord-Hollandsche UM, 1972. Citado 2 vezes nas páginas 29 and 30.

GUAZZELLI, É.; HINCH, E. J. Fluctuations and instability in sedimentation. *Annual Review of Fluid Mechanics*, Annual Reviews, v. 43, p. 97–116, 2011. Citado na página 69.

HARRIS, S. E.; CRIGHTON, D. G. Solitons, solitary waves, and voidage disturbances in gas-fluidized beds. *Journal of Fluid Mechanics*, Cambridge Univ Press, v. 266, p. 243–276, 1994. Citado na página 5.

HIERGEIST, R. et al. Application of magnetite ferrofluids for hyperthermia. *Journal of magnetism and Magnetic Materials*, Elsevier, v. 201, n. 1-3, p. 420–422, 1999. Citado na página 2.

HINCH, E. J. *Disorder and Mixing*. Dordrecht: Kluwer Academic, 1988. Citado 3 vezes nas páginas xii, 47, and 59.

HOMSY, G. M.; EL-KAISSY, M. M.; DIDWANIA, A. Instability waves and the origin of bubbles in fluidized beds—ii comparison with theory. *International Journal of Multiphase Flow*, Elsevier, v. 6, n. 4, p. 305–318, 1980. Citado na página 68.

JACKSON, E. A. *Equilibrium statistical mechanics*. [S.l.]: Courier Corporation, 2000. Citado na página 107.

JACKSON, J. D. *Classical electrodynamics*. [S.l.]: John Wiley & Sons, 2012. Citado 5 vezes nas páginas xi, 29, 31, 33, and 34.

JAYARAMAN, A.; BELMONTE, A. Oscillations of a solid sphere falling through a wormlike micellar fluid. *Physical Review E*, APS, v. 67, n. 6, p. 065301, 2003. Citado na página 4.

KIM, S.; KARRILA, S. J. *Microhydrodynamics: Principles and Selected Applications*. [S.l.]: Butterworth-Heinemann, 1991. Citado 7 vezes nas páginas xi, 17, 18, 19, 21, 25, and 27.

KLAPP, S. H. Collective dynamics of dipolar and multipolar colloids: From passive to active systems. *Current opinion in colloid & interface science*, Elsevier, v. 21, p. 76–85, 2016. Citado na página 94.

KOCH, D. L. Kinetic theory for a monodisperse gas–solid suspension. *Physics of Fluids A: Fluid Dynamics*, AIP, v. 2, n. 10, p. 1711–1723, 1990. Citado na página 68.

KOCH, D. L. Hydrodynamic diffusion in a suspension of sedimenting point particles with periodic boundary conditions. *Physics of Fluids*, AIP Publishing, v. 6, n. 9, p. 2894–2900, 1994. Citado 3 vezes nas páginas 5, 44, and 69.

KOCH, D. L.; SANGANI, A. S. Particle pressure and marginal stability limits for a homogeneous mono dispersed gas-fluidised bed: kinetic theory and numerical simulations. *Journal of fluid mechanics*, CAM, v. 400, n. 1, p. 229–263, 1999. Citado na página 5.

LADD, A. J. C. Dynamical simulations of sedimenting spheres. *Physics of Fluids*, AIP Publishing, v. 5, n. 2, p. 299–310, 1993. Citado 2 vezes nas páginas 5 and 44.

LORENTZ, H. A. *Abhandlungen über theoretische Physik*. [S.l.]: BG Teubner, 1907. Citado na página 19.

MASSART, R. et al. Preparation and properties of monodisperse magnetic fluids. *Journal of Magnetism and Magnetic Materials*, Elsevier, v. 149, n. 1-2, p. 1–5, 1995. Citado na página 56.

MATTIS, D. C. *Statistical mechanics made simple: a guide for students and researchers*. [S.l.]: AAPT, 2004. Citado 2 vezes nas páginas 59 and 73.

MATTIS, D. C. *The theory of magnetism made simple: an introduction to physical concepts and to some useful mathematical methods*. [S.l.]: World Scientific Publishing Company, 2006. Citado na página 33.

MCQUARRIE, D. A. *Statistical Mechanics*. [S.l.]: University Science Books, 2000. Citado na página 58.

MELLE, S. et al. Rotational dynamics in dipolar colloidal suspensions: video microscopy experiments and simulations results. *Journal of Non-Newtonian Fluid Mechanics*, Elsevier, v. 102, n. 2, p. 135–148, 2002. Citado na página 5.

MOHAZZABI, P. Falling and rising in a fluid with both linear and quadratic drag. *Canadian Journal of Physics*, NRC Research Press, v. 88, n. 9, p. 623–626, 2010. Citado na página 4.

MOHEBI, M.; JAMASBI, N.; LIU, J. Simulation of the formation of nonequilibrium structures in magnetorheological fluids subject to an external magnetic field. *Physical review E*, APS, v. 54, n. 5, p. 5407, 1996. Citado na página 5.

MORRISON, F. A. et al. *Understanding rheology*. [S.l.]: Topics in Chemical Engineering, 2001. Citado na página 1.

NÄGELE, G. Brownian dynamics simulations. *Computational Condensed Matter Physics*, v. 37, n. 1, p. B4, 2006. Citado na página 45.

NEWTON, I. *Philosophiae Naturalis Principia Mathematica*. London: Royal Society, 1687. Disponível em: <http://royalsociety.org>. Citado na página 4.

NICOLAI, H.; GUAZZELLI, E. Effect of the vessel size on the hydrodynamic diffusion of sedimenting spheres. *Physics of Fluids*, AIP Publishing, v. 7, n. 1, p. 3–5, 1995. Citado na página 5.

NIKIFOROV, A. F.; UVAROV, V. B. *Special functions of mathematical physics*. [S.l.]: Springer, 1988. v. 205. Citado na página 34.

NITSCHE, J.; BATCHELOR, G. Break-up of a falling drop containing dispersed particles. *Journal of Fluid Mechanics*, Cambridge Univ Press, v. 340, p. 161–175, 1997. Citado na página 51.

ODEN, J. T. *An introduction to mathematical modeling: a course in mechanics*. [S.l.]: John Wiley & Sons, 2011. v. 1. Citado 2 vezes nas páginas 9 and 13.

ODENBACH, S. *Colloidal magnetic fluids: basics, development and application of ferrofluids*. [S.l.]: Springer, 2009. v. 763. Citado na página 50.

PADDING, J. T.; LOUIS, A. A. Hydrodynamic and brownian fluctuations in sedimenting suspensions. *Physical review letters*, APS, v. 93, n. 22, p. 220601, 2004. Citado na página 5.

PATERSON, A. R. *A first course in fluid dynamics*. [S.l.]: Cambridge university press, 1983. Citado na página 12.

PEYER, K. E.; ZHANG, L.; NELSON, B. J. Bio-inspired magnetic swimming microrobots for biomedical applications. *Nanoscale*, Royal Society of Chemistry, v. 5, n. 4, p. 1259–1272, 2013. Citado na página 94.

PRESS, W. H. et al. *Numerical Recipes in FORTRAN*. [S.l.]: Cambridge Univ. Press, 1992. Citado na página 56.

Purdue University. 2010. [Online; accessed September 26, 2019]. Disponível em: <https://engineering.purdue.edu/NEESR/research.html>. Citado 2 vezes nas páginas xi and 3.

RAJ, K.; MOSKOWITZ, R. Commercial applications of ferrofluids. *Journal of Magnetism and Magnetic Materials*, Elsevier, v. 85, n. 1-3, p. 233–245, 1990. Citado na página 2.

RALLISON, J. M.; HINCH, E. J. The effect of particle interactions on dynamic light scattering from a dilute suspension. *Journal of Fluid Mechanics*, Cambridge University Press, v. 167, p. 131–168, 1986. Citado na página 4.

REYNOLDS, O.; BRIGHTMORE, A. W.; MOORBY, W. H. *The sub-mechanics of the universe*. [S.l.]: Cambridge University Press, 1903. v. 3. Citado na página 11.

ROSENSWEIG, R. E. *Ferrohydrodynamics*. [S.l.]: Courier Corporation, 1969. Citado na página 1.

ROSENSWEIG, R. E. Fluidization: Hydrodynamic stabilization with a magnetic field. *Science*, American Association for the Advancement of Science, v. 204, n. 4388, p. 57–60, 1979. Citado na página 3.

ROSENSWEIG, R. E. *Ferrohydrodynamics*. [S.l.]: Courier Corporation, 2013. Citado na página 51.

ROSENSWEIG, R. E.; KAISER, R.; MISKOLCZY, G. Viscosity of magnetic fluid in a magnetic field. *Journal of Colloid and Interface Science*, Elsevier, v. 29, n. 4, p. 680–686, 1969. Citado na página 1.

ROSENSWEIG, R. E.; NESTOR, J. W.; TIMMINS, R. S. Ferrohydrodynamic fluids for direct conversion of heat energy. In: *Materials associated with direct energy conversion*. [S.l.: s.n.], 1965. Citado na página 51.

ROURE, G. A. *Macroscopic quantities of dilute non-brownian: magnetic suspensions in a shear flow*. [S.l.]: Universidade de Brasília, 2018. Citado na página 17.

ROURE, G. A.; CUNHA, F. R. Hydrodynamic dispersion and aggregation induced by shear in non-brownian magnetic suspensions. *Physics of Fluids*, AIP Publishing, v. 30, n. 12, p. 122002, 2018. Citado na página 5.

SCHWARTZ, M. *Principles of electrodynamics*. [S.l.]: Courier Corporation, 2012. Citado na página 29.

SOBRAL, Y. D.; HINCH, E. J. Finite amplitude steady-state one-dimensional waves in fluidized beds. *SIAM Journal on Applied Mathematics*, SIAM, v. 77, p. 247–266, 2017. Citado na página 5.

SOBRAL, Y. D.; OLIVEIRA, T. F.; CUNHA, F. R. On the unsteady forces during the motion of a sedimenting particle. *Powder Technology*, Elsevier, v. 178, n. 2, p. 129–141, 2007. Citado na página 4.

Sony. *Replacing dampers with fluid suspension lightens the vibration system and enhances drive, reducing energy consumption by 35%*. 2014. [Online; accessed September 26, 2019]. Disponível em: <https://www.sony.net/SonyInfo/csr/SonyEnvironment/products/BDV-N9200WL.html>. Citado 2 vezes nas páginas xi and 2.

STOKES, G. G. On the effect of internal friction of fluid on the motion of pendulums. *Trans. Camb. Phil. Soc.*, v. 9, p. 8–106, 1851. Citado na página 4.

SUNDARESAN, S. Instabilities in fluidized beds. *Annual review of fluid mechanics*, CAM, v. 35, n. 1, p. 63–68, 2003. Citado 2 vezes nas páginas 5 and 68.

TIMOSHENKO, S. P.; GOODIER, J. N. *Theory of Elasticity*. New York, NY: McGraw-Hill, 1970. Citado na página 51.

UHLENBECK, G. E.; ORNSTEIN, L. S. On the theory of the brownian motion. *Physical review*, APS, v. 36, n. 5, p. 823, 1930. Citado 4 vezes nas páginas 4, 40, 44, and 96.

WANG, S. et al. Study of hydrodynamic characteristics of particles in liquid–solid fluidized bed with uniform transverse magnetic field. *Powder technology*, Elsevier, v. 245, p. 314–323, 2013. Citado 3 vezes nas páginas 5, 70, and 98.

ZWANZIG, R. *Nonequilibrium Statistical Mechanics*. [S.l.]: Oxford University Press, 2001. Citado na página 41.

Appendix

A Langevin Magnetization

The case of non-interacting ferromagnetic suspended particles in thermal equilibrium is of particular interest to us because it provides an example where the dependence of the magnetization on the magnetic field may be directly determined[1]. Thus, it enables the validation of the formulae of magnetic force and torque which we used in our numerical simulations.

In order to determine this magnetization, we first find the potential energy of the magnetic permanent dipoles. To this, we would like to write Kelvin's force over a particle with dipole moment $\boldsymbol{m}_i$,

$$\boldsymbol{F} = \mu_0 \boldsymbol{m}_i \cdot \nabla \boldsymbol{H} \tag{A.1}$$

as the gradient of a scalar field. Since $\boldsymbol{H}$ is irrotational by Ampère's law in the magnetostatic regime, we have $(\nabla \boldsymbol{H})^T = \nabla \boldsymbol{H}$, thus it follows from Eq. (A.1) that

$$\boldsymbol{F} = \nabla \left(\mu_0 \boldsymbol{m}_i \cdot \boldsymbol{H} \right), \tag{A.2}$$

such that the potential energy of a magnetic dipole in a field $\boldsymbol{H}$ is

$$\varphi = -\mu_0 \boldsymbol{m}_i \cdot \boldsymbol{H}. \tag{A.3}$$

The total energy in a system of N non-interacting particles with permanent dipoles $\boldsymbol{m}_i$ is therefore

$$E = E_0 - \sum_{i=1}^{N} \mu_0 \boldsymbol{m}_i \cdot \boldsymbol{H}, \tag{A.4}$$

where E_0 is the ground-state energy, i.e., its energy when the magnetic field is null. Its partition function in equilibrium is given by the integral

$$Z = \int \exp(-\beta E)\, d\Omega, \tag{A.5}$$

where $\beta = 1/k_{_B}T$, over the whole state space Ω, comprised of the angles which determine the orientations of the particles. This integral is in fact a product of N equivalent iterated integrals. Integrating each one in spherical coordinates over a sphere of unitary radius,

[1] The reader should be advised that this attempt of demonstration is an oversimplification, it is inherently at fault as the Bohr-van-Leuween theorem precludes the possibility of explaining magnetization by classical mechanics. Essentially, the demonstration fails because magnetic moments are quantized, only being able to assume any value (JACKSON, 2000). However, it does need to concern us, since our systems are far from ground-states, thus quantum-mechanical effects are negligible.

the integral over the azimuth angle ϕ yields 2π, while the one over the latitude attains the following form:

$$Z(T,V,H) = Z_0(T,V)\left[2\pi\int_0^{\pi}\exp(\mu_0 m\beta H\cos\theta)\sin\theta\,d\theta\right]^N, \tag{A.6}$$

$Z_0(T,V)$ being the partition function in the absence of an applied magnetic field. Integrating over θ, we get

$$Z = Z_0\left[4\pi\frac{\sinh(\mu_0 m\beta H)}{\mu_0\beta mH}\right]^N. \tag{A.7}$$

Now note that the total magnetic dipole moment can be alternatively represented by minus the gradient of the energy with respect to the magnetic field, i.e., it follows from Eq. (A.4) that

$$\boldsymbol{m} = \sum_{i=1}^{N}\boldsymbol{m}_i = -\frac{1}{\mu_0}\frac{\partial E}{\partial \boldsymbol{H}}. \tag{A.8}$$

Therefore, the equilibrium ensemble average of the magnetic dipoles,

$$\langle\boldsymbol{m}\rangle = Z^{-1}\int \boldsymbol{m}\exp(-\beta E)\,d\Omega, \tag{A.9}$$

can also be written as

$$\langle\boldsymbol{m}\rangle = \frac{1}{\mu_0\beta}\frac{\partial\ln Z}{\partial H}\hat{\boldsymbol{H}}. \tag{A.10}$$

Taking the natural logarithm of Eq. (A.7) and deriving over H, we get

$$\langle\boldsymbol{m}\rangle = mN\left[\coth(\mu_0 m\beta H) - \frac{1}{\mu_0 m\beta H}\right]. \tag{A.11}$$

The magnetization is the volume average of the magnetic dipole moments, which in this case is simply equivalent to the division by the volume of the system, V, thus

$$\langle\boldsymbol{M}\rangle = mn\left(\coth\alpha - \frac{1}{\alpha}\right), \tag{A.12}$$

where the number density is $n = N/V$ and the magnetic field intensity parameter is defined by $\alpha = \mu_0 mH/k_{_B}T$. In terms of the volume fraction of particles, we have

$$\langle\boldsymbol{M}\rangle = \frac{3m\phi}{4\pi a^3}\left(\coth\alpha - \frac{1}{\alpha}\right). \tag{A.13}$$

With the Langevin function defined by

$$\mathcal{L}(\alpha) = \coth(\alpha) - \frac{1}{\alpha}, \tag{A.14}$$

we have

$$\langle\boldsymbol{M}\rangle = \frac{3m\phi}{4\pi a^3}\mathcal{L}(\alpha). \tag{A.15}$$

In the limit of low applied fields, the magnetization may be shown to grow linearly with the field intensity parameter. Taking into account that the cotangent is singular at $\alpha = 0$, this expansion may be somewhat involved. Our approach consists in taking advantage of the readily obtainable series of another function, $\alpha/(e^{\alpha}-1)$. Firstly, note

that the aforementioned quotient tends to a finite limit as $\alpha \to 0$, albeit the denominator goes to zero. Therefore, we have the Taylor expansion

$$\frac{\alpha}{e^{\alpha}-1} = \sum_{k=0}^{\infty} \frac{B_k}{k!}\alpha^k \tag{A.16}$$

where B_k are called the Bernoulli numbers. In order to determine these numbers, passing the denominator of the left-hand side to the right-hand side and writing it as a Taylor series,

$$\alpha = \sum_{m=1}^{\infty}\sum_{k=0}^{\infty} \frac{B_k}{k!m!}\alpha^{k+m}. \tag{A.17}$$

Now we effect the variable change $n = k + m$ in the double series, getting

$$\alpha = \sum_{n=1}^{\infty} \frac{\alpha^n}{n!}\sum_{k=0}^{n-1} \frac{n!}{k!(n-k)!}B_k. \tag{A.18}$$

By the linear independence of powers of α, we have

$$B_0 = 1 \tag{A.19}$$

and

$$\sum_{k=0}^{n-1}\binom{n}{k}B_k = 0, \quad n > 1, \tag{A.20}$$

whence it follows that $B_1 = -1/2$ and $B_2 = 1/6$.

Note that the Langevin function may be written in terms of Bernoulli numbers. Indeed, since

$$\coth(\alpha) = \frac{e^{\alpha}+e^{-\alpha}}{e^{\alpha}-e^{-\alpha}} = 1 - \frac{2\alpha}{\alpha(e^{2\alpha}-1)}, \tag{A.21}$$

there results

$$\coth(\alpha) = 1 - \frac{1}{\alpha}\sum_{k=0}^{\infty}\frac{B_k}{k!}(2\alpha)^k. \tag{A.22}$$

Replacing the first three Bernoulli numbers, we find from Eq. (A.22) that

$$\mathcal{L}(\alpha) \sim \frac{\alpha}{3}, \quad \alpha \ll 1 \tag{A.23}$$

so

$$\langle \boldsymbol{M} \rangle \sim \frac{mn}{3}\alpha, \quad \alpha \ll 1. \tag{A.24}$$

On the other hand, in the limit of large fields, Eq. (A.14) the Langevin function goes to 1,

$$\lim_{\alpha\to\infty}\mathcal{L}(\alpha) = 1. \tag{A.25}$$

Both behaviors are represented in Fig. (58). A logical physical conclusion that may be drawn from this calculation is that the maximum magnetization obtainable occurs when all dipole moments are aligned with the magnetic field, resulting in a saturation value equal to the dipole moment of a particle times their number density.

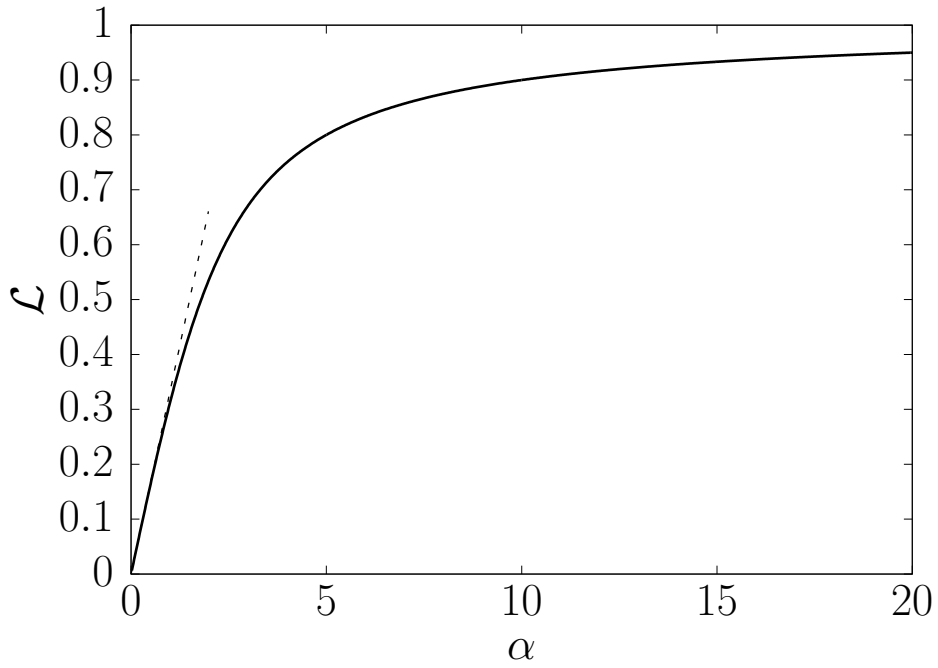

Figure 58 – Langevin function (continuous line) of the applied field intensity parameter and its linear asymptote for small values of α (dashed line).